



Experimental and Computational characterization of biofilm formation and deformation

A thesis submitted to the Faculty of Science, Agriculture, and
Engineering for the Degree of

Doctor of Philosophy

By

Subash Bommu Chinnaraj

School of Engineering

Newcastle upon Tyne

Nov. 2018

Abstract

Bacterial adhesion to surfaces is one of the crucial phases in biofilm formation. Bacterial attachment is a complex process which can be affected by flow conditions and properties of the substratum material. Experiments on initial attachment were carried out using the oral bacterial species *Streptococcus gordonii* which is one of the early colonizers of tooth surfaces. There has been a limited study about how early colonizing bacteria like *S. gordonii* adhere to stainless steel with different surface characteristics. In this study, we will concentrate on understanding the interactions at the interface between bacteria and materials.

In natural environments, a conditioning layer (e.g., saliva) would appear on the implant surface before the arrival of bacteria. Therefore, bacterial adhesion on stainless steel coated with saliva was also studied. To understand the physics of bacterial adhesion, an in-house computational model has been developed by implementing a population balance model coupled with Extended Derjaguin Landau Verwey and Overbeek (XDLVO) theory. The effect of microtopography, roughness, and flow on bacterial attachment were examined quantitatively with the computational model.

The results from the experimental and computational methods have been qualitatively comparable, and the attachment of bacteria has been altered due to combination of different surface characteristics.

Biofilm detachment and deformation is the final stage of a biofilm cycle and it is important to study how biofilms react to physical forces. Biofilm deformation was studied *in situ*, and in particular, the viscoelastic behavior of the biofilms was assessed using Particle Image Velocimetry techniques. The viscoelastic behavior was studied using the loading and unloading cycle of stress resulting from different flow velocities applied to the surface of the biofilm. The *in situ* experimental models can be used to study the material properties of biofilms without disrupting the internal structure.

Acknowledgments

Firstly, I would like to thank my supervisors Dr. Jinju Chen and Dr. Nicholas Jakubovics for sharing their invaluable knowledge, expertise, and guidance. Their support, encouragement, and advice were extremely valuable throughout the course of this work.

I would like to thank Dr. Jayathilake Pahala Gedara for his patience, help, and advice. I would also like to thank Dr. Saikat Jana for his advice, guidance, availability and the stimulating discussions.

Heartfelt thanks to all my friends Pavlos, Nehir, Fatma who made my time in Newcastle much more enjoyable. I would like to thank my friends Arun and Charan who have been there always for me.

I would like to especially thank my fiancé, who has been next to me even when she was miles away. Her love and sacrifice during the final stages of this Ph.D., is much appreciated.

Last but not least, I would like to thank my brother and dad for their support every single day on every decision I made and for providing everything to fulfil my dreams.

Contents

1	Introduction	1
1.1	Thesis Structure	5
2	Literature Review	7
2.1	Introduction.....	9
2.2	Bacterial attachment.....	11
2.3	Hydrodynamic conditions and motility:	11
2.4	Forces at the solid-liquid interface	14
2.4.1	Surface roughness.....	14
2.4.2	Effect of surface topographical patterns in bacterial attachment	19
2.4.3	Surface chemistry	22
2.4.4	Surface coatings	26
2.4.5	Effect of bacteria-surface appendages	27
2.5	Human oral cavity.....	30
2.6	Mechanical properties of biofilms	32
2.6.1	Viscoelasticity	33
2.6.2	Viscoelastic models	34
3	Experimental characterization of bacterial attachment on stainless steel surfaces	39
3.1	Introduction.....	41
3.2	Materials and Methods	42
3.2.1	Stainless steel samples:	42
3.2.2	Profilometry.....	43
3.2.3	Scanning electron microscopy and Energy dispersive X-ray spectroscopy.....	43
3.2.4	Atomic force microscopy.....	43
3.2.5	Contact angle measurement.....	44
3.2.6	Zeta potential measurements	45
3.2.7	Bacterial culture	46
3.2.8	Dynamic culture condition.....	47
3.3	Results and discussion.....	50
3.3.1	Sample characterization	50
3.3.2	Bacterial viability on steel surfaces	54
3.3.3	Optical density measurement	56
3.3.4	Fluorescence imaging.....	57
3.3.5	Bacterial attachment to static conditions.....	58

3.3.6	Bacterial attachment underflow	64
3.4	Conclusions	69
4	Computational modelling of bacterial attachment on steel surfaces..	71
4.1	Introduction	73
4.2	Numerical methods.....	74
4.2.1	Surface element integration	74
4.2.2	XDLVO theory	76
4.2.3	Navier-Stokes equation	79
4.2.4	Diffusion – convection	81
4.2.5	Finite difference method.....	82
4.2.6	Bacterial adhesion.....	84
4.3	Results and discussion	87
4.3.1	Simulation of bacterial deposition in static conditions	87
4.3.2	Bacterial deposition on sample surfaces	90
4.3.3	Modelling bacterial attachment on nanostructured titanium surfaces.....	97
4.4	Conclusions	100
5	Biofilm Deformation underflow	101
5.1	Introduction	103
5.2	Experimental methods	103
5.2.1	Lithography	103
5.2.2	Particle velocimetry	104
5.2.3	Velocity profile in microchannels:	113
5.2.1	Pressure Calculation:	116
5.3	Experimental setup	117
5.3.1	Image Acquisition	117
5.3.2	Recording techniques:	117
5.3.3	Syringe pump operation	118
5.3.4	Bacteria culture	119
5.3.5	Microfluidics setup.....	119
5.3.6	Image Pre-processing	119
5.3.7	Processing	121
5.4	Results and discussion	122
5.5	Conclusions	134
6	Conclusions and future work	135
6.1	Conclusions	137

6.2 Future work	138
Appendix	140
References	141

List of Figures

Figure 2:1 The life cycle of biofilm.	9
Figure 2:2 Height of the hydrodynamic boundary layer for low and high flows.....	12
Figure 2:3 Representation of a roughness profile.	15
Figure 2:4 Representation of two different roughness profile.....	16
Figure 2:5 2D profile of a rough surface showing the skewness in the profile.	17
Figure 2:6 Roughness profile showing kurtosis.	18
Figure 2:7 Increasing the contact area of the surface changes the bacterial attachment (Hochbaum and Aizenberg, 2010).	21
Figure 2:8 Characteristic DLVO and XDLVO potentials, with different interactions.	26
Figure 2:9 Schematic representation of a bacteria approaching a substrate (Flemming, 2011).....	27
Figure 2:10 Net interaction potential between the 500 nm radius bacterial cell and the surface for the different appendage radii at an ionic strength of 10 mM (Ammar <i>et al.</i> , 2015).	29
Figure 2:11 Schematic of a Maxwell model.	34
Figure 2:12 Schematic of a Kelvin-Voigt model with a spring and a dashpot in parallel.....	34
Figure 2:13 Various three element models.	35
Figure 2:14 Cross section of a biofilm grown from wastewater from treatment plant after applying stress.....	37
Figure 3:1: Topography of the channels and an SEM image of 40 μm depth channelled sample.....	43
Figure 3:2 CAD design of the flow chamber.	48
Figure 3:3 ANSYS simulation of one flow chamber.	49
Figure 3:4 Flow chamber setup for bacterial attachment under flow conditions.....	50
Figure 3:5 Cross-sectional profile for different steel samples a) 10 μm channels and b) 40 μm channels.	51

Figure 3:6 SEM images a) 10 μm deep channel b) chemically etched surface inside a 10 μm channel c) 40 μm deep channel d) chemically etched surface inside a 40 μm channel.	52
Figure 3:7 AFM images of a) plain samples b) inside 10 μm channel c) inside 40 μm channel.....	53
Figure 3:8 Biofilm growth on steel samples.	55
Figure 3:9 Rinsing cycles after bacterial attachment.	56
Figure 3:10 Optical density measurements corresponding to the number of colony forming units per ml.....	57
Figure 3:11 Fluorescence images of a) Plain steel samples b) 10 μm channelled sample.....	57
Figure 3:12 Plot showing obtained for the experiments for saliva coated and uncoated surfaces.	59
Figure 3:13 SEM images of a) 10 μm depth channel with attached bacteria the upper surface is the on the top and the channel is on the bottom. b) 40 μm depth channel with attached bacteria.	61
Figure 3:14 Plot showing number of attached bacterial cells on different samples.	62
Figure 3:15 SEM image of attached bacteria on to the peaks of the rough surface.....	63
Figure 3:16 SEM image of a plain steel surface.	63
Figure 3:17 Bacterial attachment to steel samples underflow velocity of 0.125 cm/s.....	65
Figure 3:18 Bacterial attachment to steel samples underflow velocity of 0.253 cm/s.....	66
Figure 3:19 Bacterial attachment to steel samples underflow velocity of 0.8 cm/s.....	67
Figure 3:20 Bacterial attachment on steel samples under three different flow conditions (with p values * < 0.01 and * = no significance).....	68
Figure 4:1 (a) Schematic diagram of a bacterial cell and computationally recreated material surface. (b) Schematic diagram showing the calculation of separation distance between an approaching particle and asperity on the surface.....	76
Figure 4:2 An uniform Cartesian grid used to discretize the computational domain.....	82

Figure 4:3 A simple function y plotted against x describing the finite difference method.	83
Figure 4:4 Representation of interaction force boundary layer (IFBL) and diffusion and convection (Ammar <i>et al.</i> , 2015).	85
Figure 4:5 Histogram showing the distribution of asperities for surface recreation a) SAD= 3.15% and Ra=10.5 nm b) SAD=3.15% and Ra = 45.24 nm.	87
Figure 4:6 Interaction energy curves for different average roughness at an ionic strength of 20 mM and zeta potential of 10 mV	88
Figure 4:7 Interaction energy curves for different zeta potentials of the bacteria using ionic strength of 20 mM and average roughness as 55.8 nm.	89
Figure 4:8 Interaction energy curves for different ionic strengths using zeta potential of bacteria as -10 mV and average roughness as 55.8 nm.	90
Figure 4:9 Schematic representation of the lid-driven cavity flow.	91
Figure 4:10 Velocity of the fluid in the direction of the moving wall along the vertical line passing through the centre of the cavity was derived and compared with the results of (Aydin and Fenner, 2001).	91
Figure 4:11 Surface coverage on different samples from the diffusion equation.	92
Figure 4:12 Flow profile across a 10 μm depth channel used for the computational model.	93
Figure 4:13 Flow velocity over a 40 μm depth channel showing the channel profile used in the computation.	94
Figure 4:14: Surface coverage calculation of deposited bacterial cells using diffusion-convection equation, with an inlet velocity of 0.125 cm/s.	95
Figure 4:15 Surface coverage calculation of deposited bacterial cells using diffusion-convection equation, with an inlet velocity of 0.253 cm/s.	95
Figure 4:16 Surface coverage calculation of deposited bacterial cells using diffusion-convection equation, with an inlet velocity of 0.8 cm/s.	96
Figure 4:17 SEM images of three titanium surfaces a) Polished titanium surface b) Spear-type surface s. C) The pocket-type surface (Cao <i>et al.</i> , 2018).	97
Figure 4:18 Interaction energy for titanium surfaces.	99
Figure 5:1 A schematic of the laser illuminated PIV system.	105

Figure 5:2 Schematic representation of a micro PIV system.	106
Figure 5:3 Cross-correlation and particle displacement from image pairs with particles of diameter 1 μm	109
Figure 5:4 a) Dark phase contrast image of 0.5 μm particles underflow b) Bright phase contrast image of 0.5 μm particles underflow.	110
Figure 5:5 2D representation of the cross-correlation output.....	112
Figure 5:6 2D representation of the cross-correlation output of a pair of images separated by time dt and with background noise.	112
Figure 5:7 Contours corresponding to the velocity field u_x for Poiseuille flow inside a rectangular microfluidic chamber of height 30 μm , width 800 μm	113
Figure 5:8 Analytical velocity profile for a flow rate of 100 $\mu\text{l/h}$ for the channel of height 30 μm , width 800 μm	115
Figure 5:9 Theoretical and experimental velocity magnitude across the width of the channel.	115
Figure 5:10 a) Illustration of single frame multiple exposure methods. The images of particles are recorded in the same frame by this method. b) Illustration of multiple frame single exposure methods.	118
Figure 5:11 A Sample flow rate ramp used in the experiments.	119
Figure 5:12 Image Pre-processing.	120
Figure 5:13 Background removal from images.	121
Figure 5:14 PIV processing.	121
Figure 5:15 Plots showing the velocity profile for different flow rates.	122
Figure 5:16 Contour plots showing the velocity magnitude (a) and the pressure (b) for a flow rate of 1000 $\mu\text{l/h}$	123
Figure 5:17 Contour plots showing the velocity magnitude (a) and the pressure (b) for the flow rate of 5000 $\mu\text{l/h}$	124
Figure 5:18 Images showing the velocity magnitude (a) and the pressure (b) at three different time points for the maximum flow rate of 25000 $\mu\text{l/h}$	124
Figure 5:19 Stress vs time for the flow rate of 1000 $\mu\text{l/h}$	125
Figure 5:20 The interface of biofilm showing the deformation over time for maximum total stress of 0.08 Pa.	126
Figure 5:21 Stress vs time for the flow rate of 5000 $\mu\text{l/h}$	126

Figure 5:22 The interface of biofilm showing the deformation over time for maximum total stress of 0.8 Pa.	127
Figure 5:23 Stress versus time for a flow rate of 25000 $\mu\text{l/h}$	127
Figure 5:24 Biofilm deformation under maximum stress.	128
Figure 5:25 Stress in the liquid versus strain experienced by biofilm for a flow rate of 1000 $\mu\text{l/h}$	129
Figure 5:26 Stress in the liquid versus strain experienced by biofilm for a flow rate of 5000 $\mu\text{l/h}$	130
Figure 5:27 Stress-strain curve for the maximum flow rate of 25000 $\mu\text{l/h}$	131
Figure 5:28 Deformation of biofilm under a flow velocity of 0.14 m/s (25000 $\mu\text{l/h}$) near the biofilm surface.	133

List of Notations

E	Youngs modulus
η	Coefficient of viscosity
ε	Strain
σ	Stress
γ_1^{LW}	Lifshitz-Van der Waals component of surface energy
γ_1^+	Acid component
γ_1^-	Base component
Φ	Interaction energy
G_{AB}	Acid-Base free energy
ψ	Zeta potential
A_h	Hamaker constant
ε_0	Permittivity of vacuum
ε	Relative permittivity
k	Inverse Debye length
ω	Vorticity
Ψ	Stream function
ρ	Density
μ	Viscosity
k	Boltzmann constant
D	Diffusion coefficient
\emptyset	Interaction energy for adhesion
α	Stokes correction factor
R_a	Average roughness
C_{rms}	Root mean square correlation
Q	Flow rate
p	Pressure

List of Abbreviations

EPS	Extra cellular matrix
RMS, R_q	Root mean square
SAD	Surface area difference
LW	Lifshitz –van Der Waals
AB	Acid-Base
DLVO theory	Derjaguin and Landau, Verwey and Overbeek theory
eDNA	Extracellular DNA
CFU	Colony forming units
SD	Standard deviation
OD	Optical density
PBS	Phosphate buffer solution
SEM	Scanning electron microscope
AFM	Atomic force microscope
SEI	Surface element integration
SNR	Signal to noise ratio
FFT	Fast Fourier transform
PIV	Particle Image Velocimetry

List of Publications

Cao, Y., Su, B., Chinnaraj, S., Jana, S., Bowen, L., Charlton, S., Duan, P., Jakubovics, N.S. and Chen, J. (2018) 'Nanostructured titanium surfaces exhibit recalcitrance towards *Staphylococcus epidermidis* biofilm formation', *Scientific Reports*, 8(1), p. 1071.

1 Introduction

Bacteria are the most ancient form of life on earth and can be dated back beyond 3.7 billion years (Dodd *et al.*, 2017). Since they have existed and evolved for so long, bacteria are now an extremely diverse group and can be found in almost everywhere from deep oceans to the outer most layers of the atmosphere. Although the bacteria are very diverse, common factors among the different types of bacteria are, they tend to form colonies and they are typically in microscopic scales. Bacterial cells have maintained the ability to survive as single cells in the planktonic phase. Nevertheless, like multicellular eukaryotes, bacterial cells are commonly found in communities where metabolic pathways from differentiated cell types combine and contribute to the functioning of the system as a whole. These microbial communities are known as biofilms.

Biofilms naturally occur in the environment and in different industrial and natural processes. For example, biofilms have been employed in wastewater treatment plants for decades to degrade the pollutants in wastewater (Wanner and Reichert, 1996). Biofilms, on the other hand, pose a serious hazard in the medical field where the development of biofilms in implants and in fluid lines are a major cause of healthcare-associated infections (VanEpps and Younger, 2016). In addition, biofilms cause problems of fouling and corrosion in natural and industrial settings from the hulls of ships to the degradation of oil pipelines (Videla and Herrera, 2005; Bryers, 2008). Owing to the diverse effects of biofilm growth, research interest in different communities of bacteria has intensified over the last thirty years. Bacterial attachment is the initial and crucial step in the process of biofilm formation. The ability to control the attachment of bacteria either increasing or decreasing adhesion by altering the material properties of the target surface can have a considerable effect on the development of biofilm.

It has been found that surface roughness may affect bacteria attachment, although the links between roughness and microbial colonization are not yet fully understood (Aykent *et al.*, 2010; Dantas *et al.*, 2016). In addition, surface topographies have also been shown to alter bacterial attachment to surfaces (Epstein *et al.*, 2011; Kargar *et al.*, 2012). However, there is a lack of robust modelling techniques to study how the mechanical

properties of surfaces affect bacteria attachment. The extended DLVO theory (Van Oss, 1989; Hoek and Agarwal, 2006) has been used to describe the mechanism of bacterial adhesion. However, this model only gives a qualitative evaluation of bacterial adhesion. Therefore, further work is required to improve models of bacterial adhesion.

Once the biofilm is mature, shear forces may cause deformation or detachment (Stoodley *et al.*, 2001; Stoodley *et al.*, 2002; Towler *et al.*, 2003). It is important to understand these processes since detachment of cells from the biofilm can lead to dispersal and translocation of bacteria to new surfaces, where they can initiate the formation of a new biofilm. Even so, mechanical forces are traditionally used to disrupt the biofilm structure such as brushing the teeth or the use of high-pressure water to remove biofilms.

The study of biological processes has been greatly enhanced in recent years by the ongoing development of new and improved technologies that enable miniaturization of laboratory models, which often increases the throughput for experimental work. For example, microfluidics has now become widely available for research laboratories (Kim *et al.*, 2012; Rusconi *et al.*, 2014). Microfluidic technology is highly beneficial for the study of biofilms due to small liquid volume control, the ability to confine cells and molecules in spatial geometry, the precise generation of gradients (e.g. to study chemotaxis in bacteria), relatively low cost and precise analysis. Microfluidic devices provide a closed system where biofilms can interact under controlled hydrodynamic conditions. These systems allow validation and iterative development of computational models of the influences and effects of the hydrodynamic conditions such as shear stresses on biofilms (Kim *et al.*, 2012). In addition, microfluidics greatly enhances the ability to study the effect of fluid flow on microbes by allowing one to create controlled flows over a wide range of flow speeds and shear rates (Rusconi *et al.*, 2014). Therefore, here microfluidic channels will be the major experimental system for the study of biofilm deformation.

This project aims to experimentally and computationally characterize bacterial attachment on steel surfaces with different structural arrangements and to investigate biofilm deformation due to physical stresses.

The objectives are

- To characterize the influence of surface roughness, topographies and fluid flow in the attachment of bacteria on steel surfaces.
- To develop a 2D computational model using XDLVO theory and Surface element integration incorporating fluid flow to determine the combined effects in the surface coverage of the bacterial attachment.
- To identify and develop an experimental method for deformation of biofilm for different flow stresses using Micro- Particle Image Velocimetry (PIV) techniques.

1.1 Thesis Structure

In order to achieve the project objectives, the thesis is divided into six chapters.

Chapter 1 provides an introduction to the work, including the main objectives to reach the aim and providing details about the organization of the manuscript.

Chapter 2 contains a detailed literature review about biofilms, bacterial attachment with different factors influencing the attachment such as fluid flow, motility, surface roughness, methods for quantifying surface roughness, conditioning layer, bacterial biofilms in the human oral cavity.

Experimental characterization of bacterial attachment is given in **chapter 3**. Experimental methods, quantification techniques are stated, and the results are summarised. The effect of surface roughness, microscopic topographies and fluid flow on the attachment of oral bacteria *S. gordonii* on the steel surfaces explained.

Chapter 4 presents the computational results for the deposition of bacterial cells on steel surfaces. The numerical methods used in the computation is described in detail. The results from chapter 3 are qualitatively compared with the simulation results to validate the model. XDLVO interaction energies are calculated for *Staphylococcus epidermidis* on titanium Nano topographical surfaces.

In **Chapter 5** an experimental model has been developed to test the viscoelastic properties of biofilm *in situ* using microfluidics and high-speed imaging. The biofilm deformation and the stresses acting on the biofilm are summarised.

Chapter 6 presents a summary of the findings from all the experimental and computational work. The overall conclusions of this study are given with respect to the aims and objectives and future possible directions of this work are presented.

2 Literature Review

2.1 Introduction

Microbial organisms that are encapsulated within a self-developed matrix of polymers and attached to different surfaces are known as biofilms (Characklis and Marshall, 1990; Costerton *et al.*, 1995; Flemming and Wingender, 2010). This microbial community is commonly found in natural environments, where the planktonic cells form colonies on a fluid-solid surface (Biofilms) or in a fluid medium (flocs). Biofilms are one of the most distributed forms of life on earth. Biofilms can be of many uses such as solid waste degradation from wastewater (Capdeville and Rols, 1992), production of chemicals, drugs, and biofuels (Halan *et al.*, 2012).

The bacterial biofilm is comprised of one or more species of bacterial cells co-occurring in a slime of the extracellular matrix. The process of biofilm formation is complex ranging from attachment, quorum sensing, extracellular matrix production, maturation and dispersal to planktonic phase.

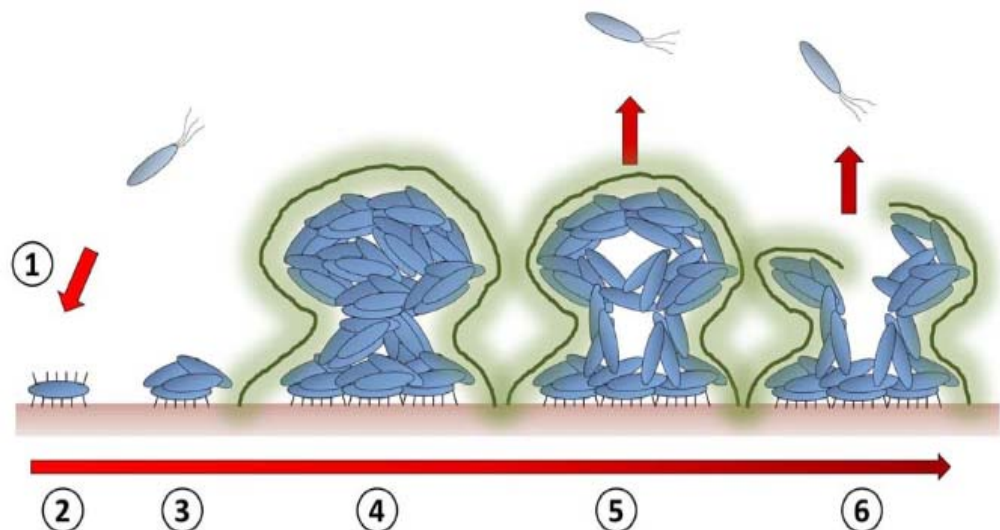


Figure 2:1 The life cycle of biofilm. The different stages of the biofilm are (1) free swimming bacterial cells, (2) Attachment, (3) Division, (4) Extracellular matrix production, (5) Dispersal upon maturity, (6) Cell lysis and matrix dissemination (Garnett A and Matthews, 2012).

Biofilms are found in most natural environments and generally, all biofilms undergo the cycle as shown in Figure 2:1. Biofilms are colonized on

interfaces. The first phase in the biofilm development is the transport of planktonic bacteria to the substrate surface (Donlan, 2002). The substrate is generally covered with a conditioning film comprising of organic and inorganic materials (Flemming and Wingender, 2010). The transport of the bacterial cells in the bulk medium is aided by diffusion, fluid flow or motility. When the bacterial cells are few hundreds of nanometres near the surface electrostatic and Van der Waals forces act on the bacterium, causing a reversible attachment to the surface or to other bacteria already attached on the surface (Watnick and Kolter, 2000; Missirlis and Katsikogianni, 2007). Following the reversible attachment, the bacteria is irreversibly attached to the substrate by the formation of polymer bridges with the surface (Garrett *et al.*, 2008). Following the irreversible attachment, the bacteria attached to the surface initiate the biofilm formation by the production of the polymeric substance. The initiation for biofilm development can be due to certain responses such as nutrient availability (George *et al.*, 2000), quorum sensing (Cvitkovitch *et al.*, 2003; O'Loughlin *et al.*, 2013). Generally, the biofilms are made up of 10-25% of bacteria and 75-90% extracellular polymeric substance (EPS). The EPS forms a natural barrier to the biofilm by providing protection from physical (Stoodley *et al.*, 2002) and chemical factors (Donlan and Costerton, 2002; Stewart, 2002). The EPS is made of polysaccharides, glycoproteins and extracellular DNA (Flemming *et al.*, 2007). In addition biofilm communities have either one species of bacteria or in most environments consists of multiple species of bacteria co-occurring as seen in wastewater treatments (Jayatilake *et al.*, 2017), oral cavity (Kolenbrander *et al.*, 2002).

Bacterial biofilms can mature, and bacterial cells disperse to the planktonic phase again for propagation. Motile bacteria can disperse from the biofilm in response to chemotaxis (Lele *et al.*, 2013). Other ways of dispersal are by the degradation of the EPS matrix or by physical forces and entering the planktonic phase for recolonization.

The initial step of adhesion allows the bacterial cells to colonize on a host surface and the detachment from the surface results in propagation and survival of the bacteria.

2.2 Bacterial attachment

The first phase in biofilm formation is the attachment of free planktonic bacterial cells to the substratum (Missirlis and Katsikogianni, 2007).

Properties of grown biofilm such as size depend on the initial bacterial attachment (Graham and Cady, 2014) which take place in two stages. In the first stage, the bacteria are attracted towards the surface through physical forces such as motility, Brownian motion and fluid flow (Liu and Tay, 2002). The second stage is in effect when the bacteria is close to the surface (in the order of nm) and specific long range and short range interactions become effective (Liu and Tay, 2002). Bacterial attachment to surfaces is a complicated process involving several parameters like surface chemistry (electrostatic charge, surface coatings), surface energy (hydrophobicity), topography, mechanical properties (shear forces due to fluid flow, elastic modulus of cell) and cell surface structures (pili, fimbriae and flagella) (Aykent *et al.*, 2010). In addition to the above-mentioned forces, other main factors influencing attachment single cell level are the liquid medium, solid surface and the bacterial cell morphology.

2.3 Hydrodynamic conditions and motility:

The first step in any bacterial attachment is the transfer of free planktonic cells from the liquid medium to reach the surface. The approach to the surface can be either passive, by convection, diffusion, Brownian motion, and gravitational forces or active by bacterial motility (Donlan, 2002; Boks *et al.*, 2008). The bacteria in the bulk medium are free to move and the major force affecting cell motion is convection (liquid flow). There can be different types of environments based on the flow conditions, such as oral cavity (Ding *et al.*, 2010) where the flow velocity is low compared to other high flow rate environments like fluid pipelines (Mahapatra *et al.*, 2015), ship hulls (Kavitha and Raghavan, 2018) or the urinary pathway (Vincent *et al.*, 2010). The flow velocity in the bulk medium also affects the boundary layer at the liquid-solid interface. A boundary layer starts from the wall surface and extends to the fluid medium. This layer of fluid is dominated by viscous forces rather than convection. The thickness of the hydrodynamic boundary layer is inversely proportional to the flow velocity. The thickness of the boundary layer decreases with the increase in

velocity and shear rates as shown in Figure 2:2. There can be two possible outcomes due to higher shear and flow rates. The bacterial cells are carried away with the flow thus reducing the chance of attachment to the surface. Secondly, due to high shear at the surfaces, the attached cells in the reversible phase of attachment can be removed from the surface. In a study by (Kaya and Koser, 2012) motility of *Escherichia coli* has been studied under different flow rates. It has been observed the bacterium exhibits random trajectories at low shear, in moderate shear the bacterium tends to swim against the flow and at high shear bacterium is carried away with the fluid flow.

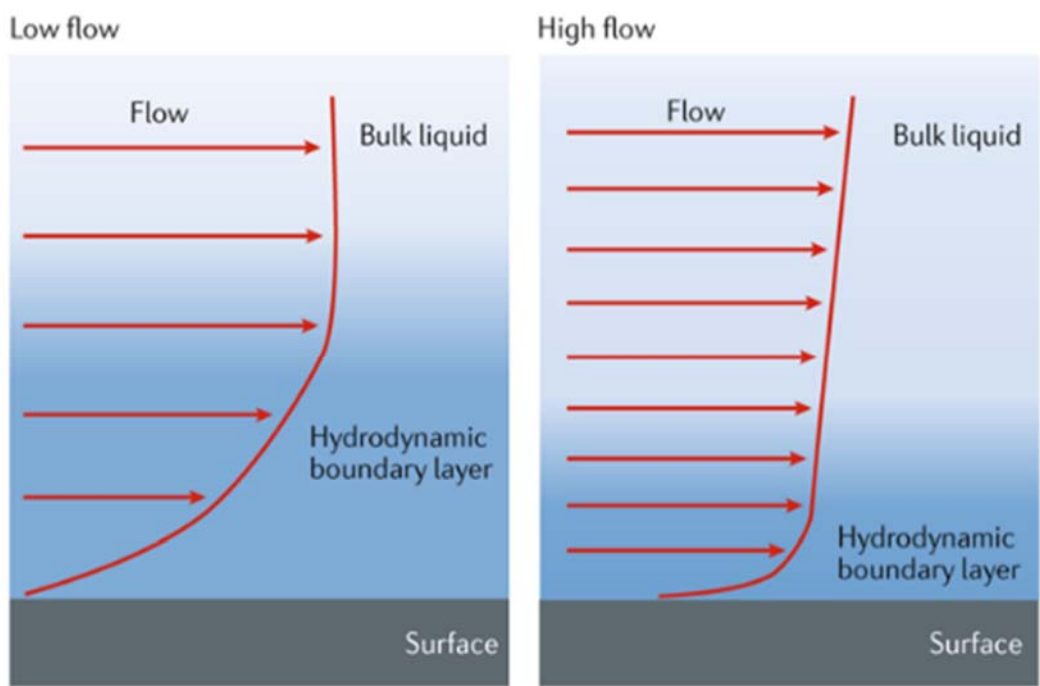


Figure 2:2 Height of the hydrodynamic boundary layer for low and high flows. The gradient shows the decay of the hydrodynamic boundary layer. (Berne *et al.*, 2018).

The second important parameter in the planktonic phase responsible for bacteria transport is the motility. Several bacterial species found in nature are motile (Ottemann and Miller, 1997; Kearns, 2010). The typical form of motility for bacteria in bulk liquid is swimming. Motility is aided by flagella which is comprised of slender helical appendages rotated by specialized motors (Bray, 2001). This flagellar movement in fluid medium makes it possible for the bacterium to adapt itself to chemotactic responses – attractive and repulsive (Lauga, 2016). Bacterial locomotion depends on

different types of interactions like hydrodynamics, electrostatics, chemical diffusion and elasticity of the body (Lauga, 2016). The flagellum of bacteria is made up of organelles (Silverman and Simon, 1974) of about 40 nm in diameter and from a few microns to 10 microns in length. Some motile bacteria have multiple flagella called peritrichous at random positions of the cell body. On the other hand, bacteria such as *E.coli* consist of flagella only at the poles of the cell body (Lauga, 2016). The most observed mechanisms in swimming are run and stop, run and reverse and run and tumble (Lauga, 2016). Owing to the size of the bacteria, the swimming timescales are smaller when compared to convective time scales (in the bulk liquid) and swimming becomes an essential factor only near a boundary or for chemotactic responses (Li *et al.*, 2008). One of the important aspects of motility near the boundary is the tendency of the bacteria to get attracted towards the surface due to the reorientation of the bacterial cells parallel to the surface (Berke *et al.*, 2008). In the bulk fluid, the bacteria are mostly found to have straight trajectories but, near the surface, trajectories are observed to be circular. The transformation from forward to circular swimming is due to the new forces and moments induced near surfaces due to the motility of the bacteria (Lauga *et al.*, 2006). It has been also shown that the Brownian motion of *Caulobacter crescentus* near surfaces is amplified due to the circular trajectories (Li *et al.*, 2008). The hydrodynamic interactions between the surface and bacteria were coupled with the fluctuations due to Brownian motion which leads to variations in speed and trajectory curvature of the bacterium. The flagella can also act as a mechano-sensor to sense the presence of surfaces (Persat *et al.*, 2015). Many bacteria are able to disable the flagellar activity in response to the mechanical forces. The drag force acting on the flagella is relatively higher for a surface attached bacterium compared to that of a planktonic bacterium (Lele *et al.*, 2013). Similarly, mechanical signaling of flagella in *Bacillus subtilis* has been shown to initiate biofilm formation (Cairns *et al.*, 2013). Thus the motility and flagella of motile bacteria play a crucial role in attachment and successive biofilm formation. Although there are several motile bacteria, non-motile cells are in equal abundance which can reach a host surface and colonize. In a study by (McClaine and Ford, 2002) involving both motile and non-motile

E.coli cells, the non-motile strain of *E.coli* was able to attach to the surface under low flow velocities with the same rate as compared to the motile species. It was only at higher flow rates the motile species, showed enhanced attachment rates. Most bacterial strains in the planktonic phase are subjected to physical forces, where the effect of motility diminishes. *Serratia marcescens* a gram-negative motile rod-shaped bacteria, has been observed to shrink and become spherical at higher cell densities and at stationary phase (Young, 2006). On the other hand, the flow characteristics of the liquid which affects bacterial attachment can be altered by the presence of solid surface structures such as topographies.

2.4 Forces at the solid-liquid interface

The second stage in the attachment of a bacterium to the surface after reaching the diffusion boundary layer, where the effect of flow is minimal are chemical composition, coatings, the roughness of the solid surface and bacterial surface appendages. The physical roughness and structure of the surface experiencing bacterial attachment is an important factor as the surfaces can influence or resist bacteria by the presence of micro and nanoscale features on the surface. The surface features are generally termed as surface topography or surface roughness. Topography can be described using roughness which is the random deviation of a surface from its mean surface. This is considered as roughness in this study. Surface topography is another term used to describe the surface property. Surface topography in relation to bacterial attachment, can be defined as structures of known dimensions and often fabricated as patterns on the surface.

2.4.1 Surface roughness

Surface roughness is the representation of the surface texture of a material in its uppermost layer. It is the quantification of the deviation of the surface from its ideal form. Bacterial attachment is also affected by the presence of rough features on the surface. Surface roughness can be altered by either manufacturing or finishing methods. The roughness of a surface can be described by the use of average roughness, Root mean square roughness (RMS), surface area difference, Skewness, Kurtosis.

2.4.1.1 Average Roughness

Average roughness is the arithmetic mean of the roughness profile heights over the evaluation distance. The average roughness is useful to define how much a surface deviates from the mean surface. Average roughness can be calculated from the measured profile by the formula,

$$R_a = \frac{1}{n} \sum_{i=1}^n |y_i| \quad (2.1)$$

where, y_i is the discrete profile heights as shown in Figure 2:3.

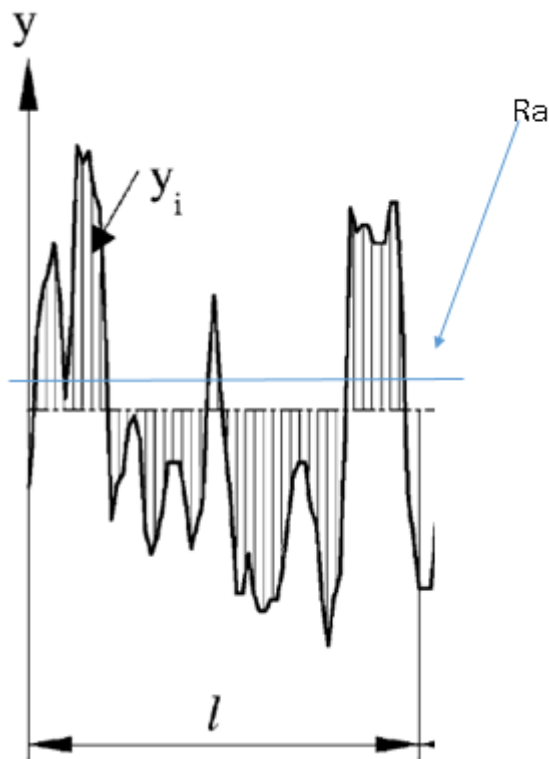


Figure 2:3 Representation of a roughness profile, with discrete height at different points over a length l and an average roughness R_a (Horvath *et al.*, 2015).

The average roughness gives an overall perspective of the roughness of the surface and historically roughness data is presented in terms of average roughness. On the other hand, the average roughness is very general in describing the surface. Average roughness cannot provide information about spatial structure or difference between peaks and

valleys. Hence other factors are also used to describe the roughness of a surface like root mean square roughness.

2.4.1.2 **Root mean square roughness (R_q)**

The root mean square roughness (RMS) is the standard deviation of the rough features from the mean plane, hence it is statistically important to represent a surface's RMS. The RMS value of a surface can be calculated as

$$R_q = \sqrt{\frac{1}{n} \sum_{i=1}^n (y_i - \mu)^2} \quad (2.2)$$

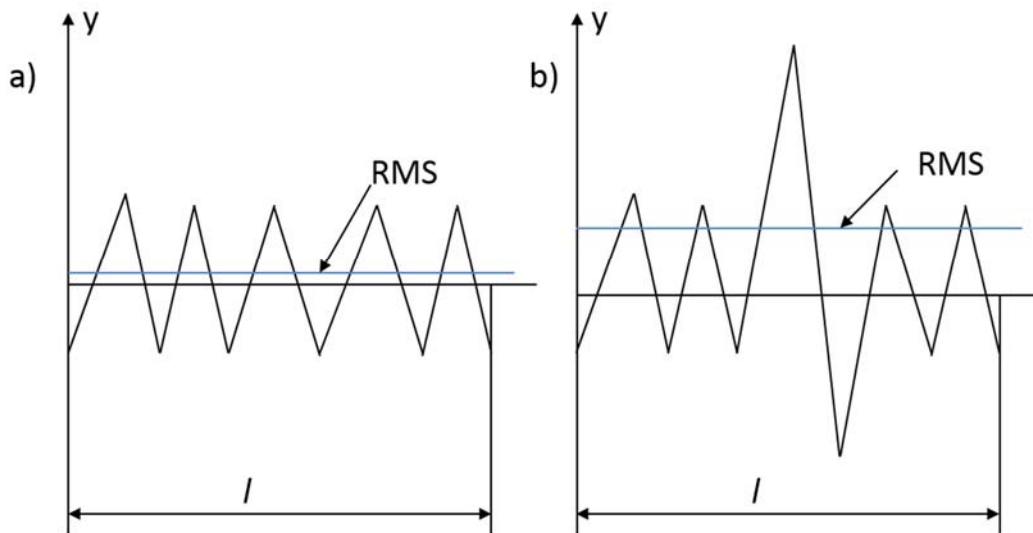


Figure 2:4 Representation of two different roughness profile. a) The rough profile has uniform peaks and valleys b) The presence of few higher peak or lower valleys compared to the rest of the profiles causes the RMS value to raise more than the Ra.

As shown in Figure 2:4 few higher peaks or lower valleys in the rough surface can cause the RMS roughness value to increase drastically making it more sensitive than the average roughness to sudden changes in roughness.

2.4.1.3 **Surface area difference (SAD)**

The surface area difference can be defined as the ratio of surface area of a rough surface to the surface area of a perfectly smooth surface of similar dimension. The SAD provides an idea about the increase in the surface area of a material due to the surface roughness. The above-mentioned

parameters are useful to assess the surface roughness properties and are commonly used in the study of roughness effect on bacteria material interactions. SAD can be calculated by the following formula

$$SAD = \frac{\text{surface area of a rough surface}}{\text{surface area of a equivalent plain surface}} \quad (2.3)$$

2.4.1.4 Skewness

Skewness is the measure of the asymmetry above and below the mean plane of the rough surface. A positive skewness means the surface has higher peaks above the mean plane and shallow valleys below the mean plane and negative skewness corresponds to a surface with deeper valleys below the mean plane and shorter peaks above the mean plane. An equal distribution of pits and peaks in the surface results in a skewness value of zero. Skewness can be represented using the following formula

$$S = \frac{1}{nR_q^3} \sum_1^n (y_i - \mu)^3 \quad (2.4)$$

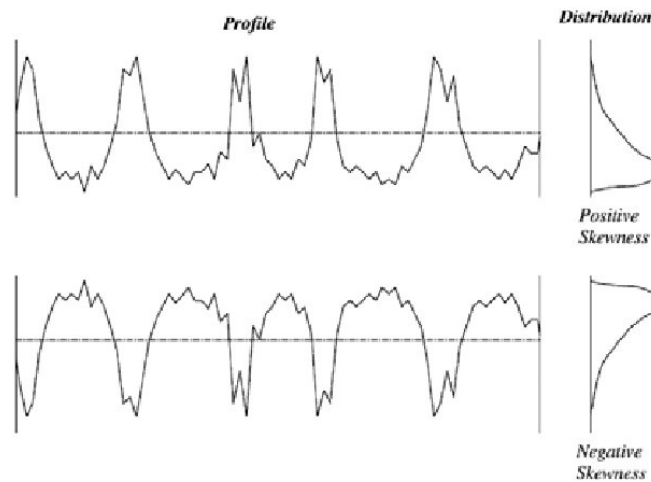


Figure 2:5 2D profile of a rough surface showing the skewness in the profile. Positive skewness corresponds to the mean of the profile distribution above zero (higher peaks than valleys) and a negative skewness corresponds to the mean of the profile distribution below zero (deeper valleys than peaks) (Horvath *et al.*, 2015).

Skewness is an important feature when analyzing engineered surfaces to analyze the effect of finishing. A skewness of negative value represents a good surface polishing as the heights are removed and only the pits remain in the surface Figure 2:5.

2.4.1.5 Kurtosis

Kurtosis represents the sharpness of the peaks in the rough surfaces. For a normal distribution of both peaks and valleys, the kurtosis value is three. If the value is less than three the rough profile has broader peaks and for a value greater than three the height distribution is spiked. Kurtosis is expressed using the formula as seen in Figure 2:6.

$$K = \frac{1}{nR_q^4} \sum_1^n (y_i - \mu)^4 \quad (2.5)$$

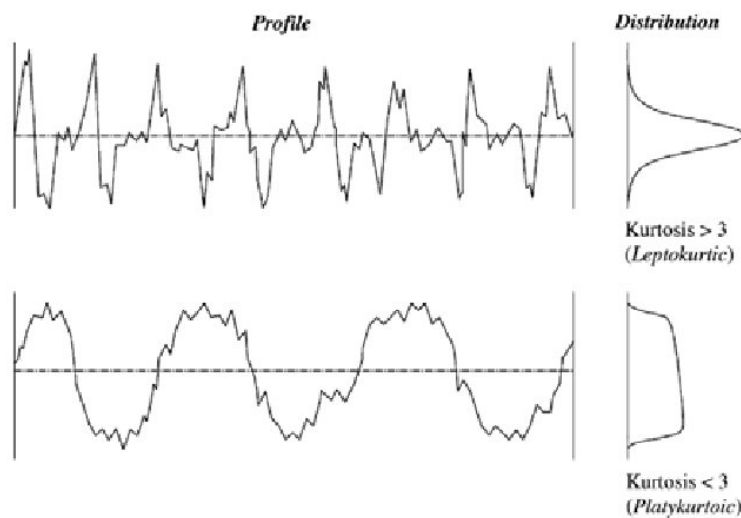


Figure 2:6 Roughness profile showing kurtosis. It can be observed for a spiked profile the kurtosis value is more than 3 and for a kurtosis value of less than 3 the profile has broader peaks (Horvath *et al.*, 2015).

The above parameters can be used to describe a rough surface. In most cases, average roughness along with few of the remaining parameters are used to give a clear description of the rough surface under consideration.

Increased average roughness on microscale has shown increased bacterial attachment (Taylor *et al.*, 1998; Poncin-Epaillard *et al.*, 2013). The microscopic grooves or valleys in a rough surface provides more surface area for a bacterial cell to attach (Hoek *et al.*, 2003). In a study by (Yu *et al.*, 2016) on the effect of bacterial adhesion by *Streptococcus mutans* on zirconia surfaces with different finishing/polishing methods quantified by average roughness showed the initial attachment of bacteria increases with surface roughness. It is further shown the effect of roughness is observed in only initial adhesion phase and not in biofilm development. Another study using *Listeria monocytogenes* adhesion and

removal on polyester urethane (used in conveyor belt systems in the food industry) showed not only roughness increases bacterial adhesion, but it also decreases the effectiveness of the biofilm removal from the belt surface (Chaturongkasumrit *et al.*, 2011).

The valleys created by the rough features also produce wells of low interaction energy in which bacteria might preferentially attach. A similar study for colloidal attachment was carried out by (Hoek *et al.*, 2003), where a computational model has been described for colloidal particles interacting with rough surfaces in terms of DLVO theory. It has been shown that rough surfaces have lower interaction energy barrier compared to that of smooth surfaces. This reduction in interaction barrier depends on the magnitude of the roughness (Hoek *et al.*, 2003).

On the other hand, the impact of Nanoscale roughness on bacterial attachment has shown varied results. Bacteria strains like *Staphylococcus aureus* and *E.coli* (Etxeberria *et al.*, 2013) showed increased attachment, whereas the reduction in attachment was observed by *Pseudoalteromonas issachenkonii* (Mitik-Dineva *et al.*, 2008). The studies vary depending on the strains and on the surfaces hence, surface roughness should be studied as a combined effect with surface properties of both the bacteria and surface. Another aspect of the surface property influencing bacterial attachment with respect to the surface property is the topography of the surface. Many studies have been carried out in recent times to develop novel surface topographies to control the bacterial adhesion.

2.4.2 Effect of surface topographical patterns in bacterial attachment

The topography of surfaces is mostly controlled at macro-scale, rather than Micro and Nano-topographical (surface patterns) levels (Graham and Cady, 2014). The effects of topographies in bacterial attachment have been carried out with surfaces generated using roughening or polishing (Aykent *et al.*, 2010). The increase in attachment was caused by the wedging of bacterial cells on randomly sized grooves. Recent studies have focussed on defined engineered topographies to study the effects of

topography in bacterial cell attachment (Hou *et al.*, 2011; Graham and Cady, 2014). The topographical scales decide the parameters involved in the attachment of the bacteria. Surfaces with rough features much larger than the size of the bacteria are considered to be smooth. (For e.g., For a spherical bacterial cell with a diameter of 1 μm , surface with rough features of 10 μm can be considered to be a flat surface) (Crawford *et al.*, 2012). However, the flow conditions highly influence bacterial attachment at these scales (Busscher and van der Mei, 2006). Attachment to topographies in the order of bacterial cell is highly influenced by the cell size and the shape of the topography (Crawford *et al.*, 2012; Graham and Cady, 2014). On the other hand, attachment to nanoscale topographies is highly dependent on the bacterial appendages like the pili and fimbriae which are in the order of nanometres (Epstein *et al.*, 2011) and studies show contradicting results (Hizal *et al.*, 2017; James *et al.*, 2017). Surface patterns also increase the surface area for contact of the bacterial cell (Palmer *et al.*, 2007). In a study by (Hochbaum and Aizenberg, 2010) it has been shown how bacteria form patterns on Nano topographical surfaces depending on the spacing between the Nanopillars as seen in Figure 2:7. Hence the presence of topographies and the size of the topographies highly influence or alter the adhesion of bacteria to the surfaces. By taking into account the different factors influencing adhesion, it is possible to design specific engineered topographies which can affect attachment for specific bacteria based on the morphology (Graham and Cady, 2014).

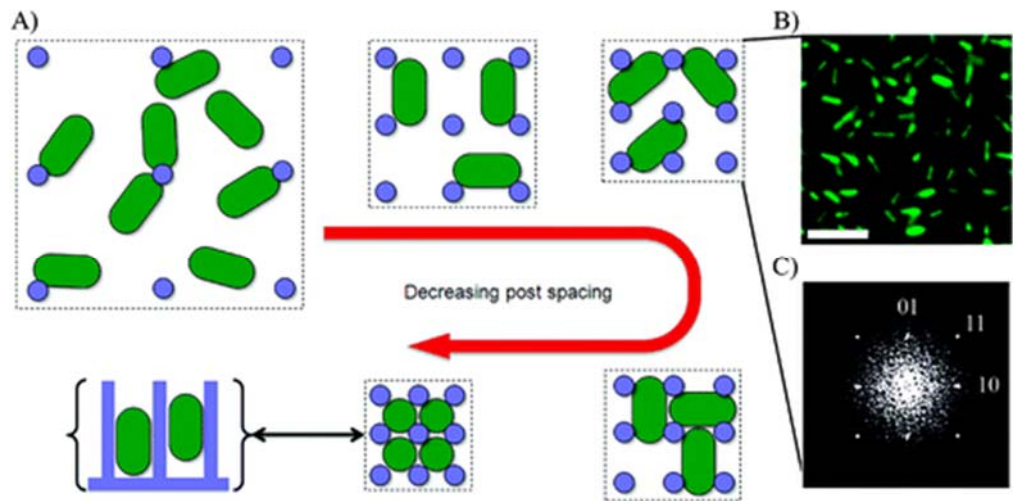


Figure 2:7 Increasing the contact area of the surface changes the bacterial attachment (Hochbaum and Aizenberg, 2010).

Other approaches inspired from natural anti-bacterial surfaces like cicada wings (Hasan *et al.*, 2013), dragonfly wings (Mainwaring *et al.*, 2016), or leaf surfaces of Taro (*Colocasia esulenta*) (Ma *et al.*, 2011) and lotus (Ensikat *et al.*, 2011). In a study by (Ma *et al.*, 2011) on taro leaves showed the presence of highly dense patterns of microscale bumps and Nanoscale epicuticular crystals. The hydrophobicity of the surface is very high, causing the droplets to roll off the surface and thereby cleaning the surface in the process. It was observed that this hydrophobicity was caused due to the presence of microscale bumps and air trapped by the nanostructures on the surface. Similar studies by (Cheng *et al.*, 2006; Ensikat *et al.*, 2011) showed self-cleaning properties of lotus leaves, which too have micro and Nanoscale structures. In the study by (Cheng *et al.*, 2006), the Nanostructured leaves were annealed at a temperature of 150°C to remove the Nanoscale structures. The results show the unprocessed leaves have higher hydrophobicity aided by the presence of Nanostructures. Similar structures inspired by patterns on shark skin have also been developed. Silicone patterned surfaces on ships designed to mimic shark skin have shown to have decreased the drag by up to 15% and attachment of algae by 67% (Kesel and Liedert, 2007). On the other hand studies by (Bhadra *et al.*, 2015; Cao *et al.*, 2018) have shown bactericidal activity on Nanostructured surfaces inspired by nature. In a study by (Cao *et al.*, 2018) *Staphylococcus epidermidis* has been observed on nanostructured titanium surfaces synthesized by

hydrothermal treatment method. 2 h and 3 h hydrothermal treatments produced different surfaces with short, thin Nano-spears (resembling cicada wing surfaces) and open porous nanostructures with intertwined Nano-spears. It has been shown the three hour processed samples delayed bacterial proliferation by rupturing the bacterial cell wall. From the studies on Nano topographies, it has been shown the combined effect of micro and Nanoscale surface features resisted bacterial attachment. It has been also observed, that the surface features alter the contact angle of the surfaces, making them hydrophobic or hydrophilic. Hence it is important to consider the surface chemistry of the surfaces when investigating the effect of bacteria attachment on rough surfaces.

2.4.3 **Surface chemistry**

Surface properties like surface chemistry and surface energy influence bacterial attachment. Materials with different functional groups alter attachment depending on the material electrostatic charge and hydrophobicity. Studies show that when surfaces like silver, DLC and plasma coatings reduced attachment of bacteria as observed in (Francois *et al.*, 1996; Woodyard *et al.*, 1996; Hauert, 2003). On the other hand, studies show that oxygen treated surfaces resulted in higher bacterial attachment (Balazs *et al.*, 2003) and thiocyanation in surfaces hindered bacterial attachment (James and Jayakrishnan, 2003). Most bacteria are negatively charged, hence bacteria are attracted towards cationic surfaces and repelled from anionic surfaces (Costerton *et al.*, 1995). Bacterial attachment to hydrophilic surfaces is preferential when surface energy of bacteria is larger than that of the liquid medium (Tuson and Weibel, 2013). Superhydrophobic surfaces can have very low initial bacterial adhesion due to low wettability of these surfaces in smaller timescales. Similarly, surfaces with peptide coatings reduced bacterial attachment. These effects are due to either hydrophobicity or electrostatic charge of surface and bacterium. The surface charge of the substrate can be altered by treatments as discussed above. On the other hand, the bacteria surface charge is dependent on the ionic strength of the fluid medium, bacterial surface structures, and bacterial age. The bacterial attachment can hence be represented as a sum of attractive and repulsive forces between the

bacterium and the solid surface. The two major forces involved are the Van der Waals forces which are attractive and electrostatic forces which are repulsive are controlled by the ionic strength (through electric double layer) and pH of the liquid medium. The hydrophobic interactions, on the other hand, are either attractive or repulsive depending on the surface and bacteria. To understand the forces associated with bacterial attachment to surfaces, different theories have been applied to describe the process. The theories are described below.

2.4.3.1 *Thermodynamic theory*

According to the thermodynamic approach, the attachment of bacteria is described as the formation of a new interface between the bacteria and surface, by removing two interfaces – bacteria liquid interface and liquid surface interface. The ability to attach is expressed using Gibbs free energy, which can be stated as

$$\Delta G = \gamma_{\text{bacteria-surface}} - \gamma_{\text{bacteria-liquid}} - \gamma_{\text{liquid-surface}} \quad (2.6)$$

where,

ΔG , the free energy for adhesion per unit area and

γ , the interfacial free energy between different factors.

The free energy for adhesion is calculated based on the assumption that the separation distance between the bacteria and surface is zero.

Attachment of bacteria occurs if, $\Delta G < 0$ which results in a decrease of the system's free energy as observed by the second law of thermodynamics.

The interfacial energies are calculated based on either Dispersion-polar approach or Lifshitz-Van Der Waals acid base approach. The free energy for adhesion for the first approach is expressed as a sum of dispersion (d) and polar (p) adhesive energies as

$$\Delta G = \Delta G^d + \Delta G^p \quad (2.7)$$

In the latter approach, the free energy for adhesion is expressed as a sum of Lifshitz Van Der Waals (LW) and acid-base (AB) energies as

$$\Delta G = \Delta G^{LW} + \Delta G^{AB} \quad (2.8)$$

In a study by (Ista and López, 2013) thermodynamic approach was used to study the attachment of bacteria on ethylene-glycol monolayers. The correlation between different surfaces and the calculated adhesion energy cannot be made. It has been noted, the shortcoming of the thermodynamic approach is due to the lack of polar components in the calculations. (Zhang *et al.*, 2015) observed the failure to determine bacterial attachment using thermodynamic theory arises when the adhesion force is close to zero. It is shown on other conditions the sign (+ve or -ve) of adhesion force agrees with the behavior of bacterial adhesion. The degree of attachment is inversely proportional to the energy difference between the cell and the surface (Zhang *et al.*, 2015). It should also be taken into account that all the calculations using thermodynamic approach are carried out using the assumption that the separation distance between bacteria and surface is zero, which is not the case with the actual attachment of bacteria. Hence DLVO theory was proposed for describing bacterial processes.

2.4.3.2 ***Derjaguin and Landau, Verwey and Overbeek (DLVO) theory***

DLVO (Derjaguin and Landau, Verwey and Overbeek) theory (Van Oss, 1989) explains the aggregation of colloidal particles and the interactions between the particles and surfaces, in terms of long range and short range interaction energies. The size scales of bacteria are similar to the colloidal particles hence, DLVO theory was proposed for describing bacterial attachment.

According to DLVO theory, the total interaction energy between bacteria (b) and surface (s) immersed in a fluid medium (l) is defined as a sum of Lifshitz –Van Der Waals interaction energy (LW) and electrostatic interaction energy (EL) as

$$U_{bls} = U_{bls}^{LW} + U_{bls}^{EL} \quad (2.9)$$

where,

U_{bls} , the total interaction energy between the cell and surface immersed in a liquid medium and

U_{bls}^{LW} , U_{bls}^{EL} are the Van Der Waals and electrostatic interaction energies respectively.

The Van Der Waals interactions between the cell and surface are the long range interactions and are expressed as a function of the radius of the cell considered. This interaction energy decays as a function of distance for distances less than 10 nm. After 10 nm, the interaction energy decay is proportional to the square of the distance.

The electrostatic interactions result from the surface charge of the substrate and ionic strength of the suspending liquid. These interactions arise from the overlap of the alternate electrical charges on the surface, which forms electrical double layers. The thickness of this double layer depends on the ionic strength of the solution. The electrical double layer interactions decay exponentially with distance and it is influenced by the thickness of the electrical double layer.

Although DLVO theory imposes distance dependence, the acid-base calculations responsible for hydrophobicity is not taken into account. As most bacterial cells are hydrophobic acid-base interactions are important to model bacterial attachment. Hence, an extended DLVO theory was proposed by Van Oss.

2.4.3.3 *Extended DLVO theory*

The extended DLVO theory represents the total energy of adhesion as the sum of Lifshitz –Van Der Waals (LW), electrostatic (EL) and acid-base (AB) interaction energies as,

$$U_{bls} = U_{bls}^{LW} + U_{bls}^{EL} + U_{bls}^{AB} \quad (2.10)$$

The Van Der Waals, U_{bls}^{LW} and electrostatic forces, U_{bls}^{EL} mentioned above are similar to the DLVO theory. In addition to the DLVO theory, the acid-base interaction energy, U_{bls}^{AB} is expressed in XDLVO theory. The acid base interaction energy decays exponentially with distance and is proportional to the radius of the bacteria. The electrostatic interactions are always repulsive and Van Der Waals interactions are always attractive. The acid base interactions are either attractive or repulsive depending on

the degree of hydrophobicity or hydrophilicity of bacteria and surface (Figure 2:8).

Based on these interactions a careful selection of materials can either favor or deter the initial attachment of bacteria. Previous studies show that aerobic bacteria are hydrophilic and most anaerobes are hydrophobic. Hence, based on these interactions, attachment of specific bacteria can be controlled.

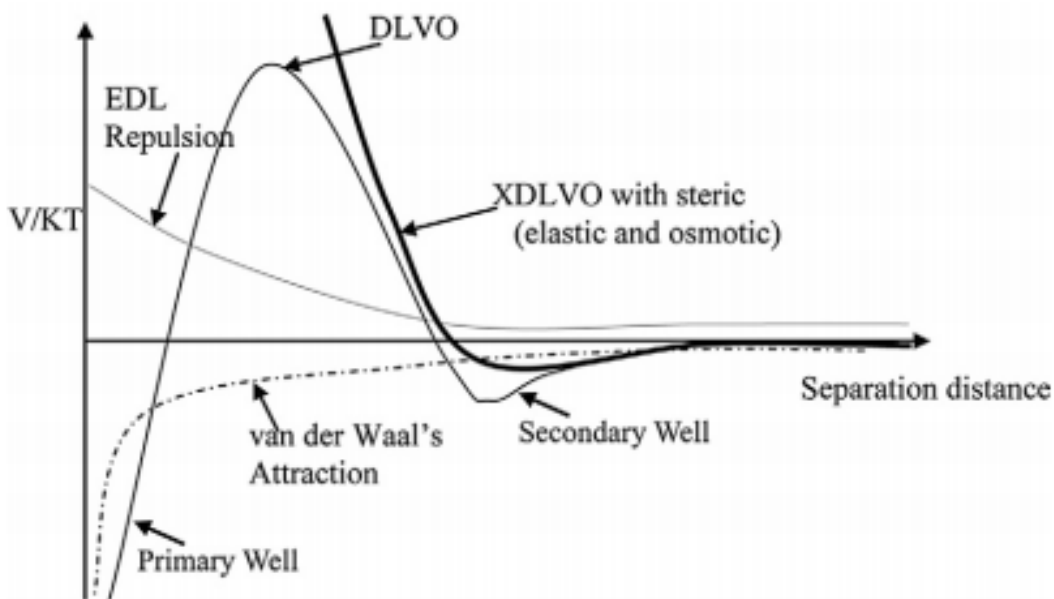


Figure 2:8 Characteristic DLVO and XDLVO potentials, with different interactions. As shown in the figure electrical double layer interactions (EDL) are always repulsive and the Van der Waal's interactions are attractive. (Hotze *et al.*, 2010)

2.4.4 **Surface coatings**

Any surface exposed to a fluid medium like water, blood, for example, becomes coated with a conditioning film. The formation of this conditioning film happens at a faster pace than any biological activity (Baier, 1982). All the particles present in the liquid medium diffuses to the surface along with bacterial cells even at very low concentrations. Bacterial cells diffuse slower than biopolymers, which have a high possibility of bonding than bacteria (Flemming, 2011). It is due to this conditioning layer bacteria also attach to surfaces which initially resist the attachment (Tuson and Weibel, 2013). The formation of the conditioning film observed was after few

minutes of exposure and continues to increase in thickness for several hours in seawater as studied by (Baier, 1975). This conditioning of the surface increases the possibility of masking the original surface properties. It has been shown that hydrophilic surfaces acquire higher wetting character (reduction in contact angle) after few hours of exposure to peptone water broth (Lorite *et al.*, 2011). Most studies focus on the modified surface properties and bacterial adhesion but the effect of conditioning surfaces are not considered in detail. Also, the effects of modifications to surface chemistry can be masked upon prolonged exposure to the environment by the coatings, resulting in altering the bacteria adhesion. The following figure depicts a gram-negative bacterium approaching an immersed surface.

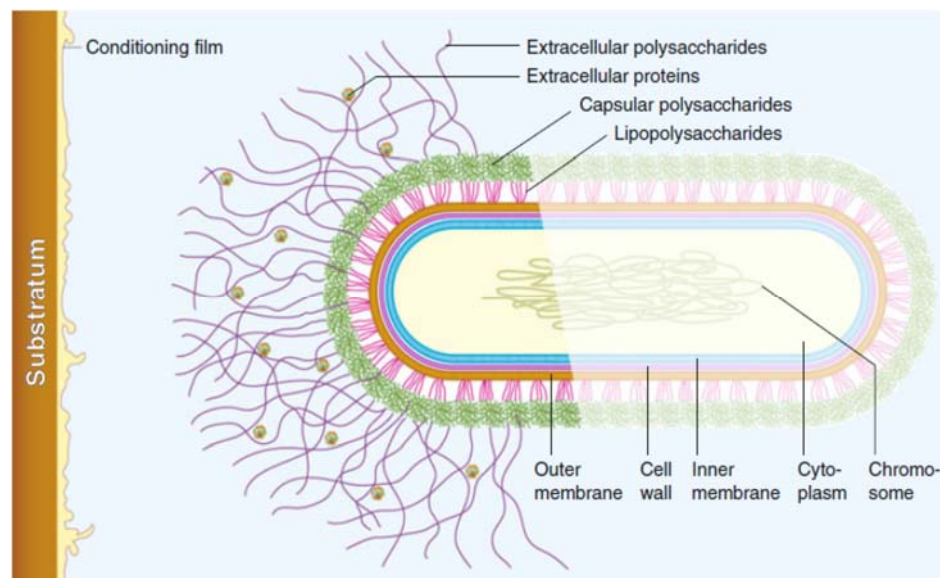


Figure 2:9 Schematic representation of a bacteria approaching a substrate (Flemming, 2011)

2.4.5 **Effect of bacteria-surface appendages**

In addition to the forces between bacteria and surface which attract the bacteria to the surface, when the bacteria approaches the proximity of the surface appendages like extracellular polysaccharides, pili influence the attachment of bacteria Figure 2:9. These appendages are made up of different proteins, lipids which are heterogeneous in nature and the types depend on the environmental conditions such as pH and nutrients available in the growth medium.

The hydrophobicity and charge on a single bacterial cell can differ across its surface due to the presence of these appendages. In a study by (Tsang *et al.*, 2006) on *Caulobacter crescentus* it has been shown that after the initial attachment, the bacterial cell attaches to the surfaces with a polar extension called stalk. The tip of the stalk contains a polysaccharide adhesin that helps in attaining a strong attachment, which is referred to as a holdfast. The adhesion strength measured using micromanipulation shows the role of adhesive hold fast in the adhesion strength, which is strongest measured among biological adhesives of more than 68 N/m^2 . This explains the importance, the appendages plays on bacterial attachment. It has been also observed that flagellum acts as an initial contact with the surface (Renner and Weibel, 2011). It has also been shown by (Friedlander *et al.*, 2013) that the flagella of *E.coli* bacteria act as a sensor to explore crevices where the bacteria will be unable to enter and thus increasing attachment.

Other appendages like pili are known to have involved in nonspecific initial attachment to surfaces (Klemm and Schembri, 2000; Berne *et al.*, 2015). The surface appendages of the bacteria which aid in adhesion are collectively known as adhesins. The adhesins, bind to specific molecules in the surfaces and are found in both gram-positive and gram-negative bacteria. The most important of these adhesins are the pili and fibrils, and they are comprised of complex surface proteins.

The type-IV pili of the soil bacterium *Myxococcus xanthus* is used to move on surfaces by the twitching motility (Jin *et al.*, 2011). It has been observed that a type IV pili can generate forces up to 100pN (Merz and Forest, 2002). The type IV pili as seen on the polar ends of the bacterium helps the bacterial to twitch by alternating pull and push actions (Jin *et al.*, 2011). The twitching motion by *Pseudomonas aeruginosa* was also observed in the same study. In another study by (Tala *et al.*, 2018) short type IV pili less than $4 \mu\text{m}$ in length of *P. aeruginosa* was observed to extend upstream against the flow, adhere and pull the cell body.

In addition, pili increases attachment with specific receptors which can adhere to specific adhesins as shown in (Pratt and Kolter, 1998), most pili

can aid in attachment to different types of surfaces, as the smaller thickness of the pili can reach the surface without experiencing greater repulsive forces as the bacterium experiences due to its bigger size. It should be noted the repulsive forces are mostly due to electrostatic forces which are short ranged as opposed to Van der Waals forces.

A computational model has been developed to study how appendages with different sizes would affect the bacteria adhesion on materials surface (Ammar *et al.*, 2015). In such case, the appendage was modeled as a rod-shape filament which covers the cell wall. The interactions between appendages and the materials surfaces were calculated based on DLVO theory. The simulations have confirmed that the presence of appendage enhances the bacteria attachment which agrees with experimental findings. In addition, it was found that the slimmer and longer appendages lead to an increased tendency of bacteria attachment (Ammar *et al.*, 2015) as seen in Figure 2:10.

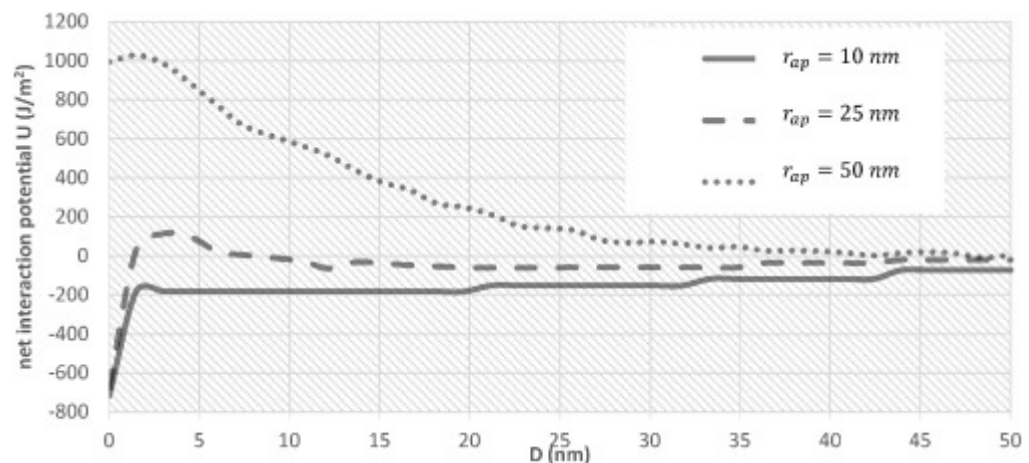


Figure 2:10 Net interaction potential between the 500 nm radius bacterial cell and the surface for the different appendage radii at an ionic strength of 10 mM (Ammar *et al.*, 2015).

Once the bacterial cell is attached initially due to short-range interactions, the process of irreversible attachment starts. Upon arrival to the surface, the appendages like pili after initial attachment, create strong contacts with the surface. In bacteria like *E.coli* and *P. aeruginosa*, the initial attachment is aided by flagella (Friedlander *et al.*, 2013), mostly attaching on the polar edge. After initial attachment the cell is repositioned to attach on the longitudinal direction, to reduce the fluid forces (Petrova and Sauer, 2012).

2.5 Human oral cavity

The human oral cavity is a diverse habitat consisting of different types of bacteria. These organisms come in contact and interact with the human tissue. It has been shown that human saliva consists of up to 10^9 bacterial cells per ml (Wade, 2013). Estimates about the number of bacterial species in the human oral cavity are more than 700 according to the Human Oral Microbiome Database. Although there are about 700 different species of bacteria in the oral cavity, only a few bacteria like *Actinomyces spp*, *Eikenella spp*, *Capnocytophaga spp*, *Haemophilus spp*, *Streptococcus gordonii* are the early colonizers of the cavity (Kolenbrander *et al.*, 2002). Due to the presence of different bacterial strains and the abundant availability of nutrients, bacterial biofilms can be complex with more than 100 bacterial species (dental plaque). At instances, the lower dental health combined with the abundance of carbohydrates (sugars) increases the acid producing bacteria in the biofilm leading to dental caries (Head *et al.*, 2017; Larsen and Fiehn, 2017). Dental caries is the decay of the tooth surface by local demineralization (Head *et al.*, 2017). If left untreated, the erosion can lead to supragingival biofilm which can spread further inside the tooth surface to form a subgingival biofilm which is one of the causes of periodontal diseases (Larsen and Fiehn, 2017). *Streptococcus mutans* is a viridians group which plays an important role in causing dental caries (Saini *et al.*, 2011). Peri-implantitis is the colonization of dental implants which causes the degradation of bone to which the implant is fixed. With the increasing number of dental implant procedures, the chance of infections also increases. Biofilms can also develop in the crevices between the teeth making it harder to remove (Donlan and Costerton, 2002). The development of biofilms (dental plaque) starts with the attachment of bacterial cells or aggregates (clumps of bacteria) to the oral cavity. In order to understand the attachment of the bacterial cells, the different types of conditions such as physical and chemical characteristics prevailing in the oral cavity have to be analyzed.

The chemical properties of the human oral cavity changes constantly depending on multiple factors such as CO_2 , protein concentration. Salivary pH in the oral cavity changes constantly due to the intake of food. (Pachori

et al., 2018) studied the effects of different food materials such as fruit juice, cold drinks, and biscuits on the changes in the pH values. In a computational study by (Head *et al.*, 2017) the role of dietary sugars in the influence of aciduric and acid-producing bacteria have been studied. It has been shown the total amount of sugar and the intake frequency increases the bacterial activity. In another study by (Kinnari *et al.*, 2009) the influence of porosity and pH on bacterial attachment to hydroxyapatite and biphasic calcium phosphate ceramics studied. The adherence of *Staphylococcus aureus* and *Staphylococcus epidermidis* was reduced significantly when the pH was reduced to 6.8. Another important feature of the dental cavity is the different roughness of the tooth surface. The surface roughness of the tooth can be altered by bleaching (Worschech *et al.*, 2003), Finishing techniques used for dental implants (Laufer *et al.*, 1996; Ayad *et al.*, 1997). Erosion of the enamel changes the roughness of the surface. (Mullan *et al.*, 2017) studied the differences in the roughness of unpolished and polished enamel surfaces following erosion was greatly reduced. The fluid flow inside the oral cavity is a very complex mechanism. In a study by (Harrison and Cleary, 2014) a computational model has been developed to study fluid motion due to gravity, inertial forces, and tongue movement. The fluid motion in the anterior oral cavity reaches a maximum velocity of 20 mm/s (Harrison and Cleary, 2014). The saliva is responsible for coating the surfaces of the oral cavity, in addition to the contribution to fluid flow. It has been shown that the saliva coating on hydroxyapatite surfaces, increased the attachment of *S. mutans* strains (Abbott and Hayes, 1984). The study also showed that negatively charged and hydrophilic salivary layers reduced the attachment of bacteria and hydrophobic saliva might aid in colonizing hydrophobic bacteria (Abbott and Hayes, 1984). Hence, the bacterial attachment in the oral cavity is a complex process involving diverse physical properties.

Bacterial attachment in the oral cavity is not only complex but is also the initial phase in biofilm development. It is crucial to study bacteria-material interactions in the human oral cavity, to reduce the infections caused by bacteria. Among the multitude of bacterial species in the oral cavity, *Streptococci* account for 60-90% of colonization in the first four hours of

cleaning (Nyvad and Kilian, 1987). Hence, *Streptococci gordonii* will be one of the main bacteria observed in this work.

The attachment of bacteria is a complicated process, involving different physical, chemical, and biological parameters. Although attachment is studied in depth from a biological perspective, studies involving all the physical factors on bacterial attachment is limited. Hence it is important to observe how bacterial adhesion can be modified by the physical properties of the materials and surroundings.

After the initial attachment, during the growth phase, biofilms are exposed to fluid flow, by which they acquire the nutrients (Stoodley *et al.*, 2000), communicate through the transfer of sensing molecules (Cvitkovitch *et al.*, 2003; Christopher and Bonnie, 2005). In addition to the mass transfer, the fluid surrounding the biofilms, impose mechanical stresses on the biofilms. The biofilms have to overcome these stresses for successful proliferation. Understanding the mechanical properties of the biofilm will help in developing effective mechanical methods for the removal of the biofilms.

2.6 Mechanical properties of biofilms

Biofilms are complex heterogeneous materials comprising of bacterial cells (single or multiple species), consisting of voids and channels to assist nutrient flow through the structure (Stoodley *et al.*, 1994) and EPS consisting of polysaccharides, eDNA, macromolecules in water thus making the biofilm a complex fluid which is not completely elastic or completely fluid (Billings *et al.*, 2015). The mechanical properties of the biofilms are crucial in determining the shape, stability of biofilm and also the nutrient uptake and mass transfer (Stoodley *et al.*, 2000). The EPS is important for the structural integrity of the biofilms by protecting the biofilm from environmental factors both chemical and physical stresses in addition to facilitating cell-cell interactions (Kundukad *et al.*, 2016). Although the biofilm matrix provides protection to the mechanical forces such as fluid flow (continuous or peristaltic), which causes the reorganisation of the biofilm (Lieleg *et al.*, 2011). The biofilm matrix also provides a soft environment inside the biofilm for proliferation and movement of the bacteria (Tolker-Nielsen *et al.*, 2000). This can be attributed to the

viscoelasticity of the biofilms. Biofilms exhibit both elastic and plastic deformation depending on the time of exposure to the biofilm. Under short duration of applied stress, biofilm exhibits elastic deformation, regaining the original shape after the stress is removed. On the other hand, viscoelastic deformation occurs on prolonged exposure to the stress, where the material starts to behave like a viscous liquid if the stress is continuously applied (Piciooreanu *et al.*, 2018). This causes the material to behave like a liquid thus losing its original shape.

2.6.1 **Viscoelasticity**

Hydrodynamic stresses from the environment cause the biofilms to deform or detach from the biofilm surface. Biofilms are viscoelastic in nature, behaving like elastic solids over shorter timescales and like viscous fluids over long periods of time. The stresses acting on a biofilm structure is one of the prominent physical forces on a mature biofilm. Survival of biofilms under high shear environments and the challenge involving the mechanical removal of biofilms can be addressed using the viscoelastic properties of the biofilm. For example, the viscoelasticity of biofilms adjust the biofilm structure over time to high shear flows to form filamentous streamers. In a study by (Drescher *et al.*, 2013) with *P. aeruginosa* biofilms in microfluidic devices showed the flow chambers exhibited sudden clogging compared to surface formed biofilms. It is also been shown, the streamers can capture cells and other biomass in the flow by acting like a sieve. This effect of forming streamers can be observed in many environments such as industrial filters, and medical devices. Another such example is the biofilm streamers formed in catheters where the fluid flow is high and fluid flow is affected as a result of clogging. In a study by (Kim *et al.*, 2014) on *S. aureus* in intravenous catheter has shown the streamer formation which can block the catheter.

Understanding the viscoelastic properties of the biofilms can help in the mechanical removal of biofilms. One of the common environments where biofilms are removed mechanically is the human oral cavity by means of brushing. There are a number of viscoelastic models which are briefly discussed as follows.

2.6.2 Viscoelastic models

Maxwell model is a two-element model with a spring and a dashpot connected in series (Figure 2:11)

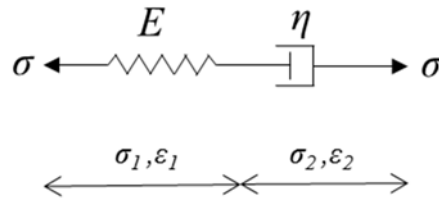


Figure 2:11 Schematic of a Maxwell model. σ_1 and ϵ_1 are the stress and strain for the spring, σ_2 and ϵ_2 are the stress and strain for the dash-pot.

$$\sigma = \sigma_1 = \sigma_2 \quad (2.10)$$

$$\epsilon = \epsilon_1 + \epsilon_2, \quad \epsilon_1 = \frac{1}{E}\sigma \text{ and } \dot{\epsilon}_2 = \frac{1}{\eta}\sigma \quad (2.11)$$

The constitutive equation of the Maxwell model is given by,

$$\sigma + \frac{\eta}{E}\dot{\sigma} = \eta\dot{\epsilon} \quad (2.12)$$

Another commonly used two element model is Kelvin-Voigt model which has a spring and a dashpot connected in parallel (see Figure 2:12).

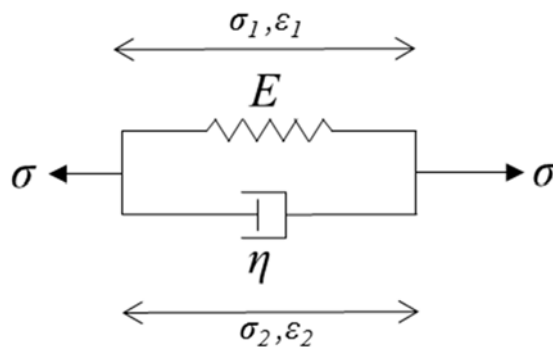


Figure 2:12 Schematic of a Kelvin-Voigt model with a spring and a dashpot in parallel. σ_1 and ϵ_1 are the stress and strain for the spring, σ_2 and ϵ_2 are the stress and strain for the dash-pot.

$$\epsilon = \epsilon_1 = \epsilon_2 \quad (2.13)$$

$$\sigma = \sigma_1 + \sigma_2, \quad \epsilon = \frac{1}{E}\sigma_1 \text{ and } \dot{\epsilon} = \frac{1}{\eta}\sigma_2 \quad (2.14)$$

The corresponding constitutive equation of the Kelvin-Voigt model is given by,

$$\sigma = E\varepsilon + \eta\dot{\varepsilon} \quad (2.15)$$

Both Maxwell model and Kelvin-Voigt model are the simplest models to predict viscoelastic behavior. Due to their limitations, three element models (known as Zener models) have been proposed (Palermo and Marzani, 2015; Piciooreanu *et al.*, 2018).

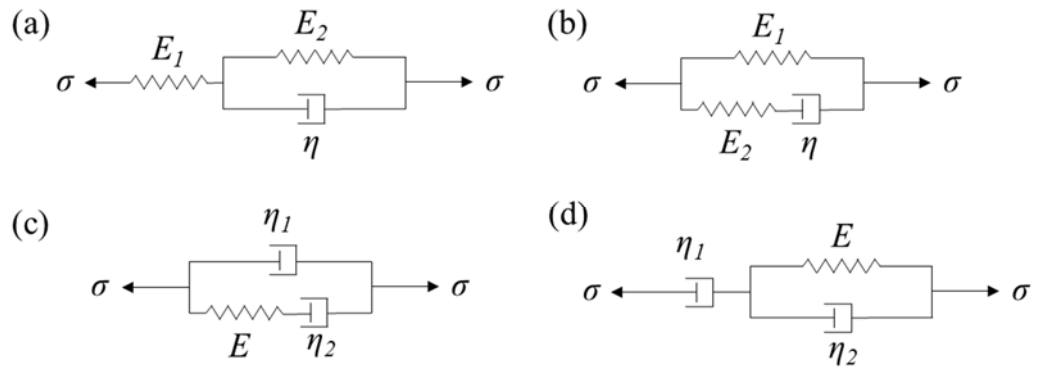


Figure 2:13 Various three element models. (a) A spring connected in series with a Kelvin-Voigt model, (b) a spring connected in parallel with a Maxwell model, (c) a dash-pot connected in parallel with a Maxwell model and (d) a dash-pot connected in series with a Kelvin-Voigt model.

The corresponding constitutive equations for the models shown in Figure 2:13 a-d are given by (Kelly, 2013),

$$\sigma + \frac{\eta}{E_1 + E_2} \dot{\sigma} = \frac{E_1 E_2}{E_1 + E_2} \varepsilon + \frac{\eta E_1}{E_1 + E_2} \dot{\varepsilon} \quad (2.16)$$

$$\sigma + \frac{\eta}{E_2} \dot{\sigma} = E_1 \varepsilon + \frac{\eta(E_1 + E_2)}{E_2} \dot{\varepsilon} \quad (2.17)$$

$$\sigma + \frac{\eta_2}{E} \dot{\sigma} = (\eta_1 + \eta_2) \dot{\varepsilon} + \frac{\eta_1 \eta_2}{E} \ddot{\varepsilon} \quad (2.18)$$

$$\sigma + \frac{\eta_1 + \eta_2}{E} \dot{\sigma} = \eta_1 \dot{\varepsilon} + \frac{\eta_1 \eta_2}{E} \ddot{\varepsilon} \quad (2.19)$$

There are also other more advanced viscoelastic models. These include Burger's model consisting of a Maxwell model and a Kelvin-Voigt model connected in series, generalized Maxwell model and generalized Kelvin-

Voigt model, which are summarized in (Mainardi and Spada, 2011; Zhao *et al.*, 2014).

Different approaches using experimental and computational modelling have been used to study the viscoelastic characteristics of biofilms (Stoodley *et al.*, 2002; Towler *et al.*, 2003; Shaw *et al.*, 2004; Jayathilake *et al.*, 2017). For example, the viscoelastic properties of biofilms can be measured by rotational rheological tests (Towler *et al.*, 2003), compression tests (Paramonova *et al.*, 2007; Kandemir *et al.*, 2018), Nanoindentation tests (Mahmoud *et al.*, 2014). For all these tests, the optical imaging is not required. However, for these tests, it is challenging to measure the biofilm mechanical properties *in situ*. Therefore, it has been suggested to the advantage of high-resolution imaging while applying the flow to measure the viscoelastic properties of biofilms *in situ*. (Stoodley *et al.*, 2002; Blauert *et al.*, 2015). Optical coherence tomography (OCT) is one of the common methods to observe real-time deformation using biofilm cross sections (Blauert *et al.*, 2015).

OCT is a very robust method and biofilm deformations can be captured using time-lapse imaging. OCT can be employed to analyze the biofilm thickness, surface roughness porosity. The typical scan area of 25-100 mm² can be achieved using the OCT technique, which imaging speeds of up to 50,000 axial scans per second (Baumann *et al.*, 2011). Biofilm deformation under fluid stress using OCT has been studied in detail by (Blauert *et al.*, 2015) using axial scan speeds of up to 29,000 per second and an area of 100 mm². By this technique, an entire biofilm structure is observed and the deformation of the biofilm before and after applying the shear is shown in the Figure 2:14. On the other hand, the calculation of the physical forces acting on the biofilm due to fluid flow is calculated using ideal conditions such as maximum flow velocity in the flow chamber where the biofilm is grown and the local disturbances in the fluid flow due to the presence of biofilm structure are not accounted. To further capture the forces exerted by the fluid on the biofilm surface, the local fluid flow should be captured to in addition to observing the biofilm structural changes.

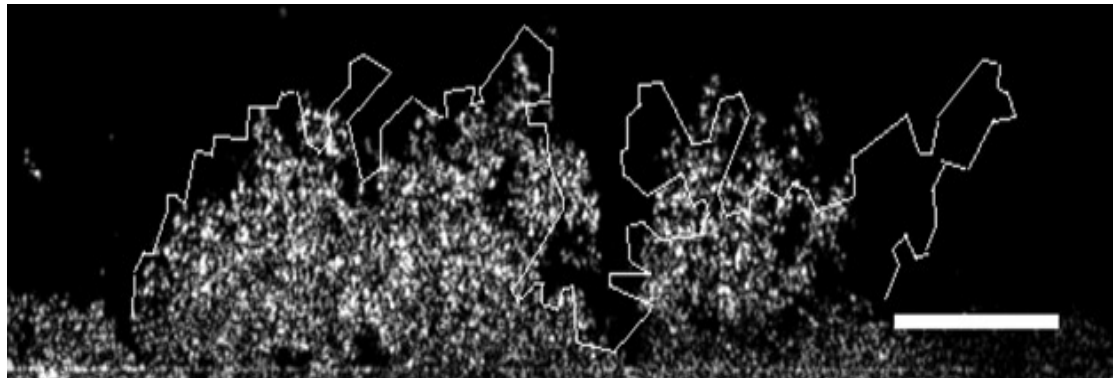


Figure 2:14 Cross section of a biofilm grown from wastewater from treatment plant after applying stress. The line in the figure represents the biofilm structure before applying the stress. The scale bar in the image corresponds to 250 μm and the flow is applied from the left of the image to the right (Blauert *et al.*, 2015).

Understanding the mechanical properties of the biofilm will lead to the development of methods to disrupt the biofilm structures using mechanical procedures. In situ study of complex biofilm systems is advantageous as the structure of biofilm is not disturbed or damaged before the experiments. As most of the conventional methods either directly measure the applied force and not bacterial properties and others measure bacterial properties and not the precisely applied forces, an experimental model to observe both biofilm and the fluid flow should be developed.

From the overall literature survey, two main stages of the biofilm life cycle are to be examined in the study. The initial bacterial attachment is one of the shortest yet crucial steps in the formation of biofilms. The next chapter will examine the attachment of bacterial cells on steel surfaces of different surface properties.

3 Experimental characterization of bacterial attachment on stainless steel surfaces

3.1 Introduction

The aim of this chapter is to investigate the topographical steel surfaces on the attachment of the early colonizing bacteria *S. gordonii*. The steel surfaces employed in the study was designed to have topographical channels which mimic the threads in the implant screws. From the clinical aspect, dental implants (e.g. stainless steel and Titanium) have threads which improve the bone-implant integrations. However, such threaded surface can also potentially attract bacteria to adhere to the implant surfaces (Crawford *et al.*, 2012). It remains elusive how this threaded patterns may affect the bacteria adhesion. Furthermore, due to the fabrication process such as machining or etching, the surface roughness in the threaded portion of the screw material will be altered from the original surface roughness.

Surface topography control bacteria attachment at macro-scale, rather than Micro and Nano-levels (Graham and Cady, 2014). The effects of surface grooves and surface roughness on bacterial attachment have been carried out on surfaces generated using roughening or polishing (Aykent *et al.*, 2010; Abban *et al.*, 2012). Bacteria may attach firmly due to the higher surface area created by the rough surfaces. Recent studies have focussed on well-defined topographies to study the effects of topography on bacterial cell attachment (Hou *et al.*, 2011; Graham and Cady, 2014). If the surface pattern is at least one order of magnitude higher than the cell size, the cell will see it as a smooth surface (Crawford *et al.*, 2012), which means that surface pattern itself may not affect cell-materials interactions. However, the flow conditions can significantly influence bacterial attachment at these scales (Busscher and van der Mei, 2006). When the surface topography is smaller or comparable to a bacterial cell, the surface topography can significantly affect cell-material interactions (Crawford *et al.*, 2012; Graham and Cady, 2014). On the other hand, bacteria attachment to nanoscale topographies is highly dependent on the bacterial appendages like pili and fimbriae which are in the order of nanometres (Epstein *et al.*, 2011; Graham and Cady, 2014). Therefore, how big the topographies are compared to bacteria will affect bacteria adhesion in different ways. By taking into account the different factors

influencing adhesion, it is possible to design specific engineered topographies which can affect attachment for specific bacteria based on the morphology (Graham and Cady, 2014).

3.2 Materials and Methods

3.2.1 *Stainless steel samples:*

The experiments to study initial bacterial attachment to steel surfaces were carried out with steel samples with micro topographical features on the surface. Grade 302 stainless steel of 0.4 mm thickness has been used to fabricate the samples. The samples were obtained from Photofabrication, St. Neots, U.K. The samples were chemically etched to fabricate micro topographical channels on the surface. Chemical etching is carried out on the materials, by first applying a mask to prevent the areas that are not required to be etched. After masking, etching acids such as hydrochloric acid, nitric acid or sulfuric acid are used. The depth of etching is dependant on the time, hence, at the required time the acid is removed and the mask is removed to expose the patterns formed by chemical etching. The channels were designed to have 120 μm width and 80 μm spacing between the channels. The depth of the channels was designed to have depths of 10 μm and 40 μm . These form two different cases for the experiments and the third sample is taken as steel samples without channels and with the natural roughness. The methods used to characterize the steel samples are given below.

The steel samples were first cleaned by ultra-sonication for 10 min. The samples are then air dried and sterilized using autoclave by wrapping in aluminium foils at higher pressure.

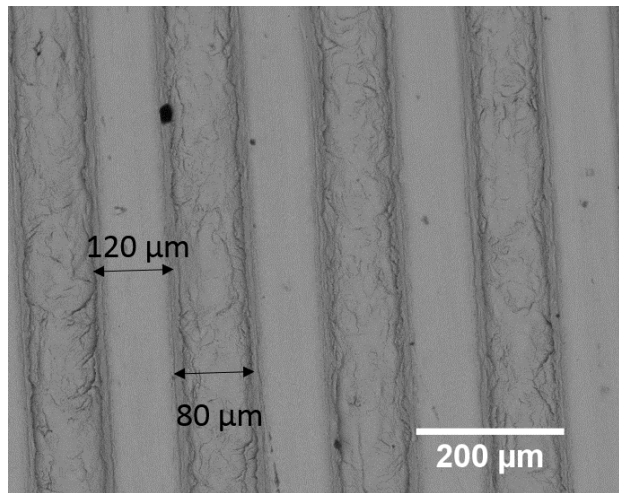


Figure 3:1: Topography of the channels and an SEM image of 40 μm depth channelled sample. The steel samples were 12 mm in diameter and contain channels of 120 μm width and 80 μm separation between the channels.

3.2.2 *Profilometry*

Profilometry was performed on the steel samples using Alicona profilometer to measure the roughness and profile variations of the steel surfaces.

3.2.3 *Scanning electron microscopy and Energy dispersive X-ray spectroscopy*

SEM (Toshiba TM3030) was used to further study the microstructure of channels. EDX was further used to estimate the initial chemical composition of the samples. The samples were ultra-sonicated and autoclaved to get rid of any surface impurities before the analysis. Images were taken at 60 \times magnification for observing the overall surface and images at 600 \times to observe topographies and 2500 \times magnification to visualize surface roughness and EDX measurements.

3.2.4 *Atomic force microscopy*

Atomic force microscopy (AFM) has been employed in the study to obtain precise roughness parameters for the steel samples used in the experiments. Measurements were carried out for 3 \times 3 μm and 10 \times 10 μm to obtain the average roughness and surface area difference (SAD) for the samples and the roughness inside the channels. PNP-TR 20 pyramidal shaped tips were used in a non-contact mode to obtain the surface parameters. Such high-resolution measurement is required as the

accurate roughness values are essential input parameters for the computational modelling developed in the Chapter 4.

3.2.5 Contact angle measurement

Contact angle measurements were taken to obtain the surface properties of the steel samples. Static contact angle measurements were obtained using KSV cam 100. Contact angle measurements were taken using three different liquids namely water, glycerol, diiodomethane. From the contact angle obtained at the solid-liquid interface the Lifshitz-van der Waals free energy, electron acceptor and donor surface tension parameters are calculated using Young's equation with extended Fowke's equation (Xu *et al.*, 1995)

$$\gamma_1^{\text{total}}(1 + \cos\theta) = 2\sqrt{\gamma_1^{\text{LW}}\gamma_s^{\text{LW}}} + 2\sqrt{\gamma_1^{\text{-}}\gamma_s^{\text{+}}} + 2\sqrt{\gamma_1^{\text{+}}\gamma_s^{\text{-}}} \quad (3.1)$$

where,

γ , the surface tension,

θ , the contact angle of the liquid made with the surface,

subscripts l, s represents the liquid and surface and LW, +, - represents the Lifshitz-Van der Waals, Lewis acid and base components of the surface tension. The different components for the three liquids used are shown in the Table 3-1.

Liquid	Lifshitz-Van der Waals component, γ_1^{LW} (mJ/m ²)	Acid component, $\gamma_1^{\text{+}}$ (mJ/m ²)	Base component, $\gamma_1^{\text{-}}$ (mJ/m ²)	Total, γ_1^{total} (mJ/m ²)
Diiodomethane	50.8	0	0	50.8
Glycerol	34	3.92	57.4	64
Water	21.8	25.5	25.5	72.8

Table 3-1 Table showing different surface tension components for the different liquids used to measure the surface tension components for the steel samples and bacteria.

Contact angle measurements were performed using the three different liquids given in Table 3-1. Contact angle measurements were obtained by

placing 10 μl of the liquids on the prepared steel samples and obtaining the images of the drops every 1 s for 10 s. The contact angles were calculated using the above formula, from the angle θ between the droplet and the surface. The contact angle used for the calculation is the average of the ten measurements. As seen from the Table 3-1 on using the different surface components for diiodomethane and the steel surface, the equation 3.1 reduces as given in equation 3.2 since the acid and base components are zero for diiodomethane.

$$\gamma_1^{\text{total}}(1 + \cos\theta) = 2\sqrt{\gamma_1^{\text{LW}}\gamma_s^{\text{LW}}} \quad (3.2)$$

As there is only one unknown component the Lifshitz-van der Waals, component for the steel surface, γ_s^{LW} it can be obtained from the above formula. The remaining components in the equation (3.1) are γ_s^+ and γ_s^- . The two unknowns can be solved by obtaining two separate equations by substituting the values for Glycerol, water and Lifshitz-Van der Waals component of the surface in the equation 3.1. The total surface tension component for the steel surface can be obtained as follows.

$$\gamma_s^{\text{total}} = \gamma_s^{\text{LW}} + \gamma_s^{\text{AB}} \quad (3.3)$$

$$\gamma_s^{\text{AB}} = 2\sqrt{\gamma_s^+\gamma_s^-} \quad (3.4)$$

The parameters for the steel surface obtained using the above method is given Table 3-2.

Lifshitz-Van der Waals component, γ_1^{LW} (mJ/m ²)	Acid component, γ_1^+ (mJ/m ²)	Base component, γ_1^- (mJ/m ²)	Total, γ_1^{total} (mJ/m ²)
42.10	0.04	3.14	42.10

Table 3-2 Table showing the surface tension components for the steel surface used, obtained by using three different liquids.

3.2.6 Zeta potential measurements

Zeta potentials of the bacterial cells suspended in water and Phosphate buffer solution (PBS) were obtained using zetasizer Nano ZS. The bacterial cells were prepared by rinsing in the centrifuge 3 \times and

suspended in deionized water or PBS at an optical density of 0.2. The prepared solution is placed in the cuvette for measurements.

3.2.7 **Bacterial culture**

The model bacterium selected for this study was *Streptococcus gordonii* DL-1 (NCTC 7868). All the chemicals were purchased from Sigma unless specified.

S. gordonii is a cocci shaped bacteria approximately 1 μm in diameter found in the oral cavity. It is found to be one of the early colonizers of the dental plaque. It is observed that *S. gordonii* colonizes within two hours after which other oral bacteria attach to form a complex dental plaque. Hence, *S. gordonii* is selected as a model organism for the experiments.

S. gordonii stock from -80°C has been thawed and streaked on Todd Hewitt agar plates and incubated for 48 h at 37°C . Single colonies were separated and incubated in liquid Todd Hewitt broth (THYE) for 24 h at 37°C to obtain stock which originated from a single cell. A sample from the overnight culture was tested for contamination using gram staining. The culture was centrifuged for 10 min at $3600 \times g$ and 20°C . The pellet of bacteria after removing the supernatant was resuspended in 50% THYE broth and 50% glycerol and stored in -80°C . The experiments were carried out from the bacteria from these stocks.

Bacterial growth on steel surfaces is carried out by adding liquid broth and overnight bacterial culture (20 μl / 2 ml) on the well plates containing steel samples. The growth medium used for the bacteria culture is Todd Hewitt broth.

Initially, cell scraper was used to remove the bacteria from materials surface followed by the sonication. However, bacterial cells were found attached on the surfaces. Therefore, imaging techniques have been used for quantification of bacterial attachment.

Bacterial attachment on steel surfaces in static condition is carried out on well plates as explained before. Instead of using the growth medium, the bacterial cells were suspended in Phosphate buffer solution (PBS) (PH 7.2). THYE broth has been replaced with PBS to limit the growth and

division to observe only bacterial attachment on the surfaces. The time limit for the experiments has been set at 30 min so that cell division is unlikely to take place in this time period. The concentration of bacteria on PBS was maintained constant with optical density (OD) of 0.2.

Overnight bacterial culture was centrifuged at 3800 ×g at 10° C for 10 min. The supernatant was removed and the pellet was re-suspended in PBS solution. The concentrated bacterial solution is diluted with sterilized PBS to an optical density of 0.2. This corresponds to a bacterial concentration of approximately 2×10^9 cells/ml.

The correlation between OD and cells/ml is obtained by measuring the Optical density and different concentrations and carrying out dilution series at that concentration to obtain the colony forming units (CFU) per ml.

For static culture conditions, in addition to the bare surfaces, the saliva-coated surfaces have been examined as well. Saliva has been collected from volunteers by Parafilm stimulation. The collected saliva is placed in ice during the process of collection. Ethical consent has been acquired for the saliva donors. Dithiothreitol from 100× stock was diluted to 2.5 mM with saliva and stirred gently on ice for 10 min. The saliva was centrifuged at 15,000 ×g for 20 min at 4°C. The supernatant was separated and added to 3× water, filter sterilized through 0.22 µm pore filter and has been stored at -20°C until used. To coat the steel samples with saliva was diluted with a coating buffer (0.02 M sodium carbonate and 0.02 M sodium bicarbonate at a pH of 9.3.) and 2 ml of the resulting solution is added to the samples in well plates and stored at 4°C overnight. The excess saliva is removed and washed with PBS to obtain the saliva coated samples.

3.2.8 *Dynamic culture condition*

Bacterial experiments under flow conditions have been carried out using a flow chamber designed for the steel samples. The flow chamber was intended to have three parallel chambers, and each chamber houses three different samples of steel.

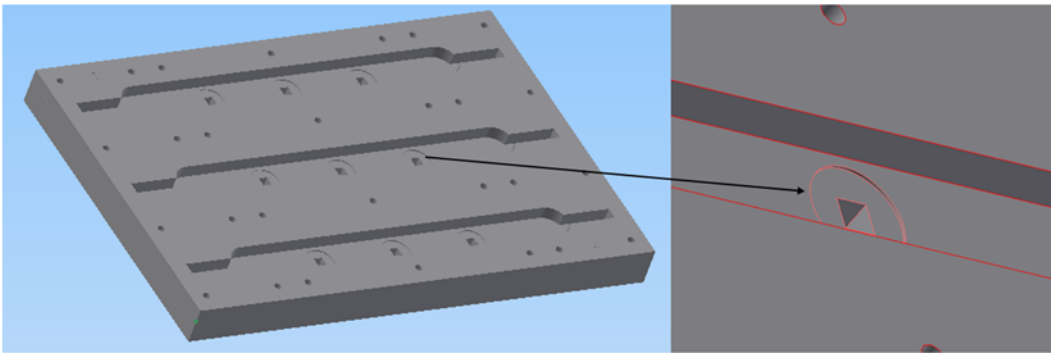


Figure 3:2 CAD design of the flow chamber with parallel flow chambers and each chamber having three slots for accommodating the steel samples.

The flow chamber was fabricated using acrylic sheets of 10 and 5 mm thickness. The chambers were cut from 5 mm thick acrylic and housing for the samples was made from 10 mm thick acrylic sheet so that the samples will be in line with the flow surface thereby reducing flow disruptions. Nitrile rubber gasket sheet was used as sealing between the chamber and the cover. The dimensions of the chambers were 5×15×150 mm. The flow was provided using a peristaltic pump (Watson Marlow 120s/DM3) with three inputs so that identical flow velocities is maintained across the three chambers.

The flow chamber has been designed using Inventor for the fabrication of the chamber. The actual model designed using Inventor has been used in ANSYS for analyzing the flow distribution. The simulation model using ANSYS was tested for the flow conditions used in the experiments, to observe if the fluid flow was uniform over the steel samples placed in the chamber. This was important as the steel samples caused slight protrusions when placed in the chamber. This will guide us where to place the steel samples so that the uniform flow distribution can be achieved (Figure 3:3). The parameters used for the simulation is given Table 3-3.

Properties	Simulation parameters
Maximum inlet fluid velocity (inlet boundary condition)	1.6 cm/s
Fluid density	998.2 kg/m ³
Fluid viscosity	0.001 kg/ms
Outlet boundary condition	Pressure- outlet
Walls of the chamber	No-slip boundary condition

Table 3-3 Parameters used for simulating the fluid flow in the chambers using ANSYS.

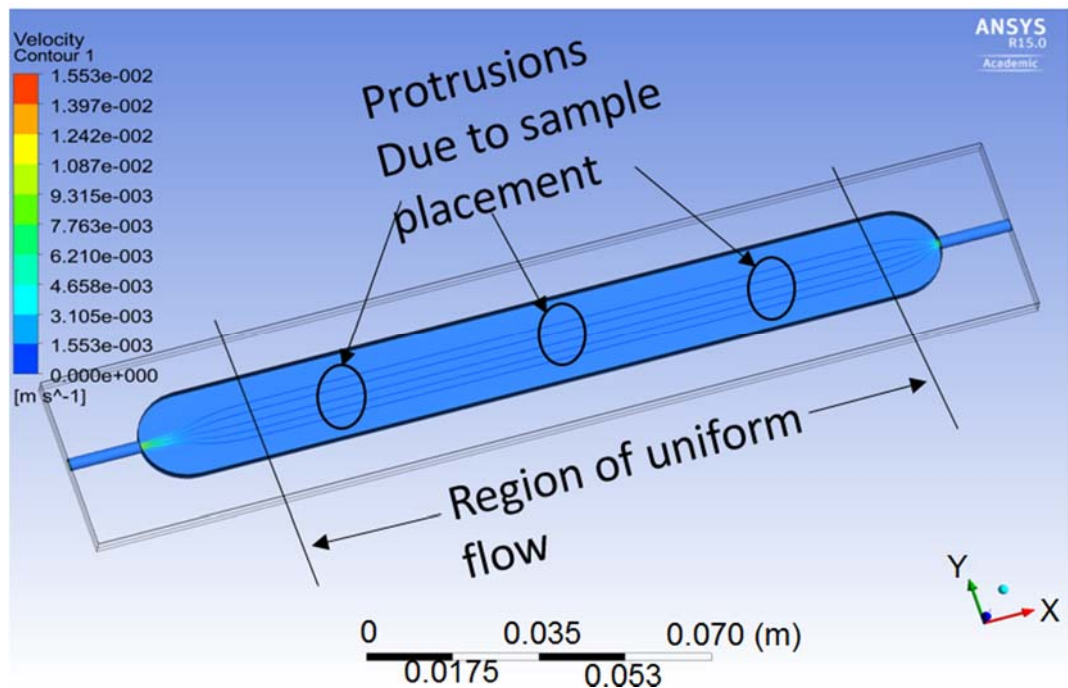


Figure 3:3 ANSYS simulation of one flow chamber. The experimental chamber consists of three identical chambers. No disturbance in the flow was observed in the model.

To study the effect of flow in the stainless steel samples three different flow velocities were selected. Fluid flow was provided using a peristaltic pump and the setup has been placed in an incubator at 37°C to maintain the bacterial cells in an active state.



Figure 3:4 Flow chamber setup for bacterial attachment under flow conditions. The system has three flow chamber with parallel inputs.

Experiments were carried out with three different velocities of 0.125 cm/s, 0.253 cm/s and 0.8 cm/s. The flow rate and pump rpm values for the three velocities are given in Table 3-1.

	Experiment 1	Experiment 2	Experiment 3
Velocity (cm/s)	0.125	0.253	0.8
Flow rate (ml/s)	5.6	11	36
Pump speed (RPM)	16	32	100

Table 3-4 Table showing the flow rates and velocities for the experiments.

3.3 Results and discussion

3.3.1 Sample characterization

The steel samples were examined under profilometer to obtain the profile of the channels and roughness parameters.

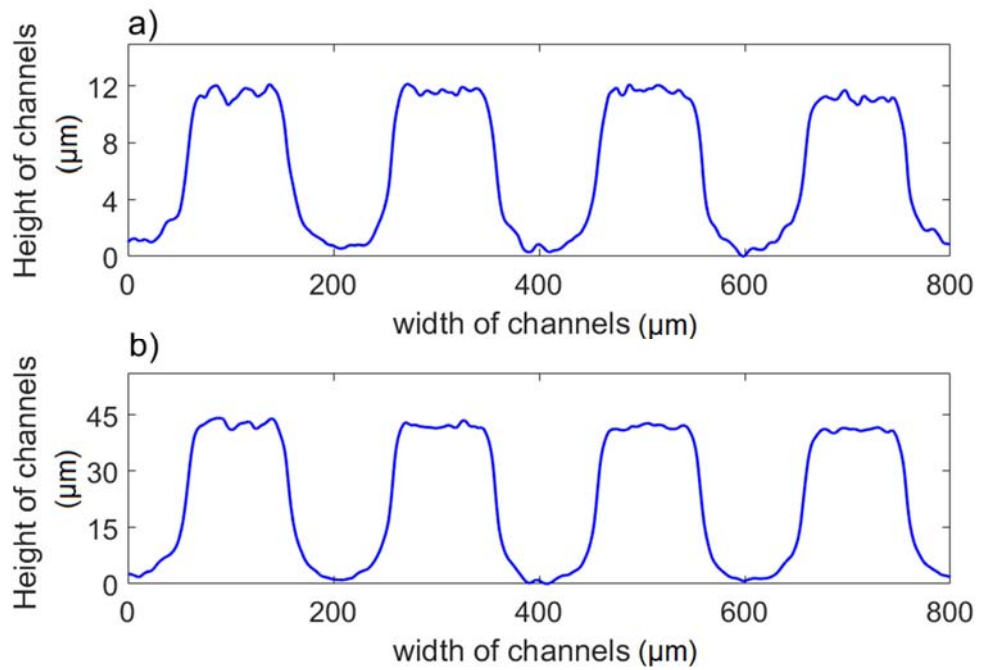


Figure 3:5 Cross-sectional profile for different steel samples a) 10 μm channels and b) 40 μm channels.

As seen from the above image, the channels are not perfect and as the depth increases, the bottom of the channel narrows. This is mainly due to the process of chemical fabrication. Chemical fabrication involves using masks to cover portions not to be etched and the remaining surface is etched in layers. Due to this as the depth and number of layers increase, the surface becomes rougher. To further examine the surface of the chemically etched steel samples SEM images were obtained (see Figure 3:6).

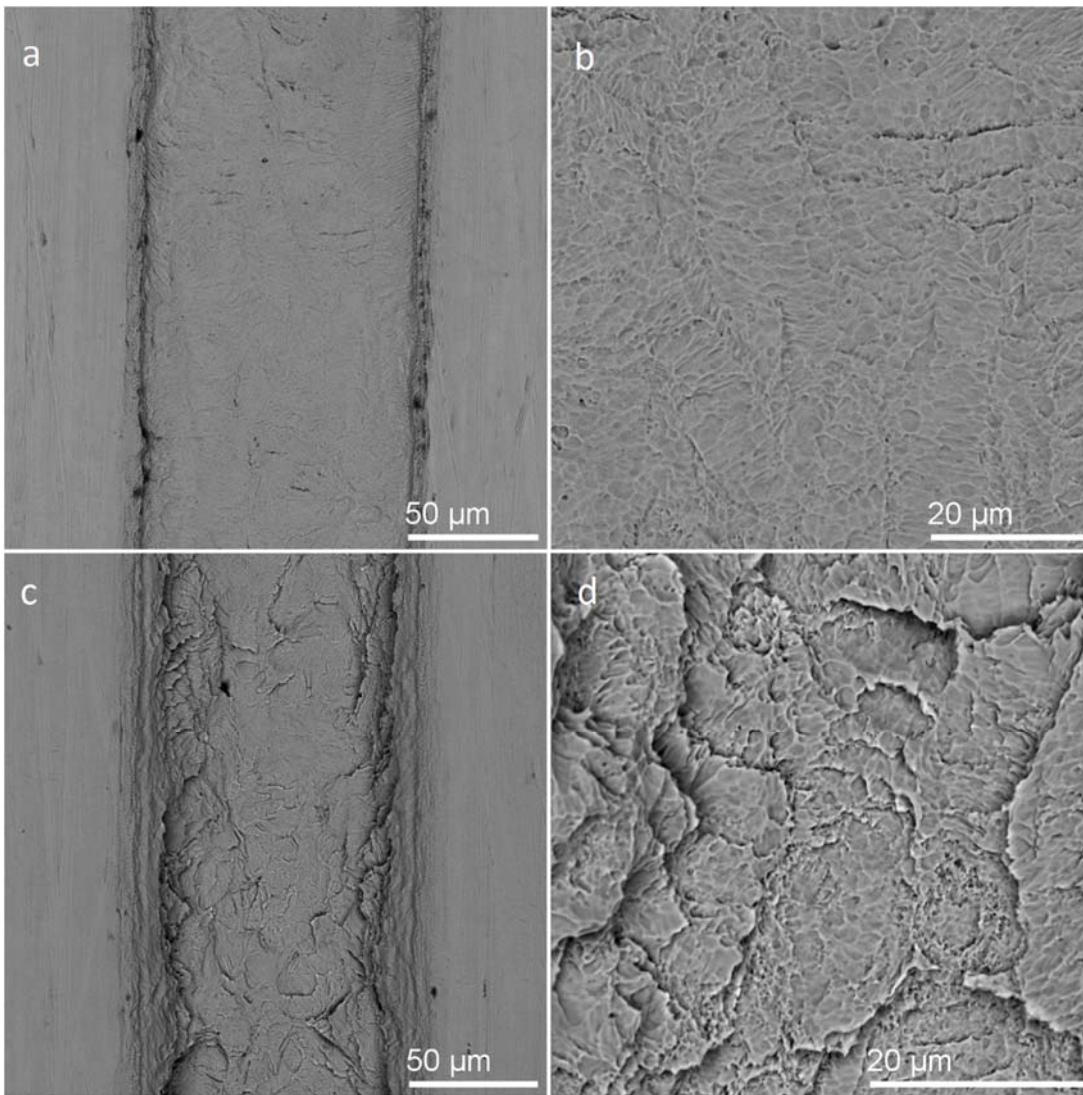


Figure 3:6 SEM images a) 10 μm deep channel b) chemically etched surface inside a 10 μm channel c) 40 μm deep channel d) chemically etched surface inside a 40 μm channel.

From Figure 3:6, the bottom of the channel for 40 μm appears to be rougher and has layered microstructures. The samples have three distinct roughness parameters, the plain samples with natural roughness and the samples with two different depths having two different roughness, which will be quantified by Atomic force microscopy (AFM).

The surfaces above the channels have the same roughness as the plain samples. The roughness parameters for plain, 10 μm and 40 μm depth channels are shown in Table 3-5.

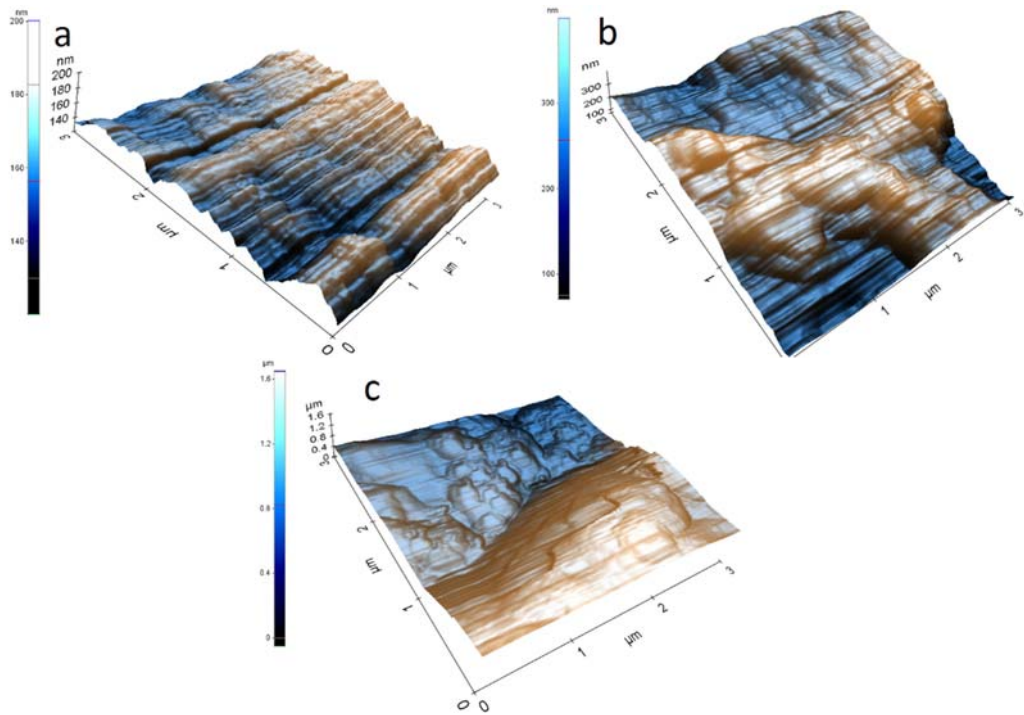


Figure 3:7 AFM images of a) plain samples b) inside 10 μm channel c) inside 40 μm channel.

Surface properties	Plain steel sample	Steel samples with 10 μm channels	Steel samples with 40 μm channels
Average roughness, Ra (nm)	46.9 ± 3.2	55.8 ± 4.6	255.9 ± 28.4
Root mean square Roughness, RMS (nm)	54.5 ± 3.8	71.0 ± 5.9	304.7 ± 35.8
Surface area difference, SAD (%)	3.15	7.54	29.35

Table 3-5 Roughness parameters of different samples obtained by AFM.

As observed from the SEM images, the 40 μm deep channels have the highest average roughness and surface area difference. The roughness parameters allow us to characterize the influence of surface roughness on the attachment of bacteria. The parameters will be used in chapter 4 to computationally model bacterial attachment on steel surfaces.

3.3.2 **Bacterial viability on steel surfaces**

To test the bacterial growth and viability on the steel surfaces, biofilm was grown on the different steel samples. *S. gordonii* was cultured as mentioned in the section 3.2.7. The samples were placed in 12 well plates and 2 ml of THYE broth and 20 µl of overnight bacterial culture was added. The samples were placed in a 37⁰C incubator for overnight growth. The culture is removed and the samples were rinsed 3X to remove any unattached or loosely attached bacteria from the surface. CFU and fluorescence imaging was carried out on the samples to observe the biofilm formed on the steel samples. In order to measure the colony forming units (CFU) from the biofilm formed on the surface two methods were used to remove the bacteria. Cell scraper was used to scrape bacterial cells attached on the surface. But cell scrapers cannot remove the cells in the channels, hence sonication was used to remove the cells in the channels. Figure 3:8 shows the cells removed after scraping and sonicating the samples. From Figure 3:8 it can be observed that the 40 µm channelled samples have higher biofilm growth or CFU/ml compared to other samples.

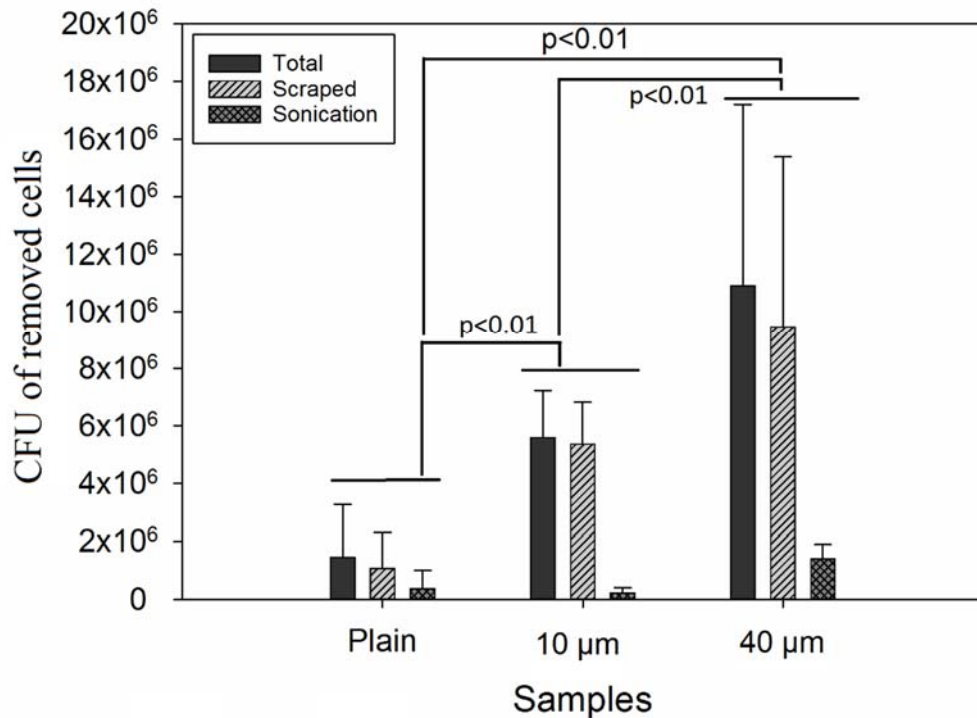


Figure 3:8 Biofilm growth on steel samples. Total CFU from the samples using scraping and sonicating the samples. The scraping corresponds to the removal of bacteria from the top surface of the channelled surfaces and sonication removes the remaining bacteria from inside the channels. The values are mean \pm SD (Standard deviation) of three independent experiments.

After testing the samples for bacterial growth and viability, the study to observe the attachment of bacteria on rough steel surfaces has been carried out. To reduce the complexity and to observe just bacterial attachment and to obtain measurable parameters for the computational model, the following steps were carried out for all attachment experiments.

- The bacterial growth medium was replaced with Phosphate buffer solution (PBS) to reduce the bacterial growth and division.
- The concentration of the cells suspended in the PBS solution was maintained at OD=0.2.
- Experiments were carried out for a timescale of 30 min further to avoid bacteria division.
- After the experiments, the samples were rinsed three times to remove un-attached or weakly attached bacteria based on Figure 3:9

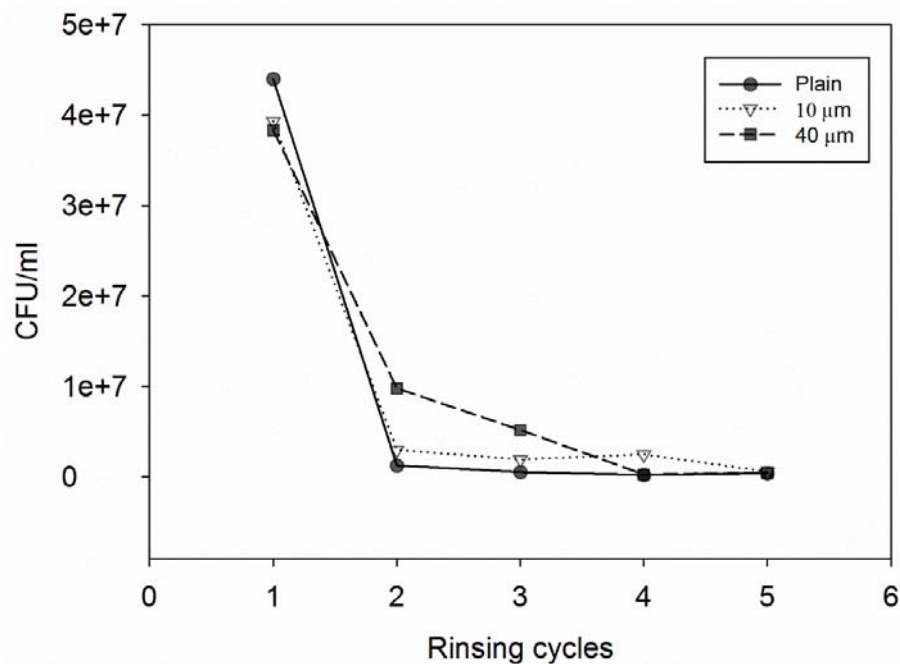


Figure 3:9 Rinsing cycles after bacterial attachment. Bacterial cells in rinsed buffer solution. Unattached bacteria are almost washed after three rinsing cycles.

The commonly suggested protocol to rinse the samples three times was only able to remove the weakly attached bacteria by 90%. When rinsing it five times, the removal rate goes up to 95%, mostly due to the presence of channels. However, there are still some bacteria firmly attached at the corners of channels which cannot be removed by such a method. Therefore, the imaging technique, as described in section 3.3.4, was adopted for quantification of bacterial attachment.

3.3.3 *Optical density measurement*

Optical density (OD) measurement is used to quantify the number of colonies forming units (CFU) per ml. Overnight bacterial culture is centrifuged and the bacterial pellet is suspended in PBS at different concentrations. The bacterial solution at different concentrations is measured for OD and the colony forming units are calculated by serial dilution. From the OD value and the CFU/ml of a particular concentration, the concentration of the bacteria in the solution is correlated. The correlation is between CFU and OD measurements are shown in the following figure.

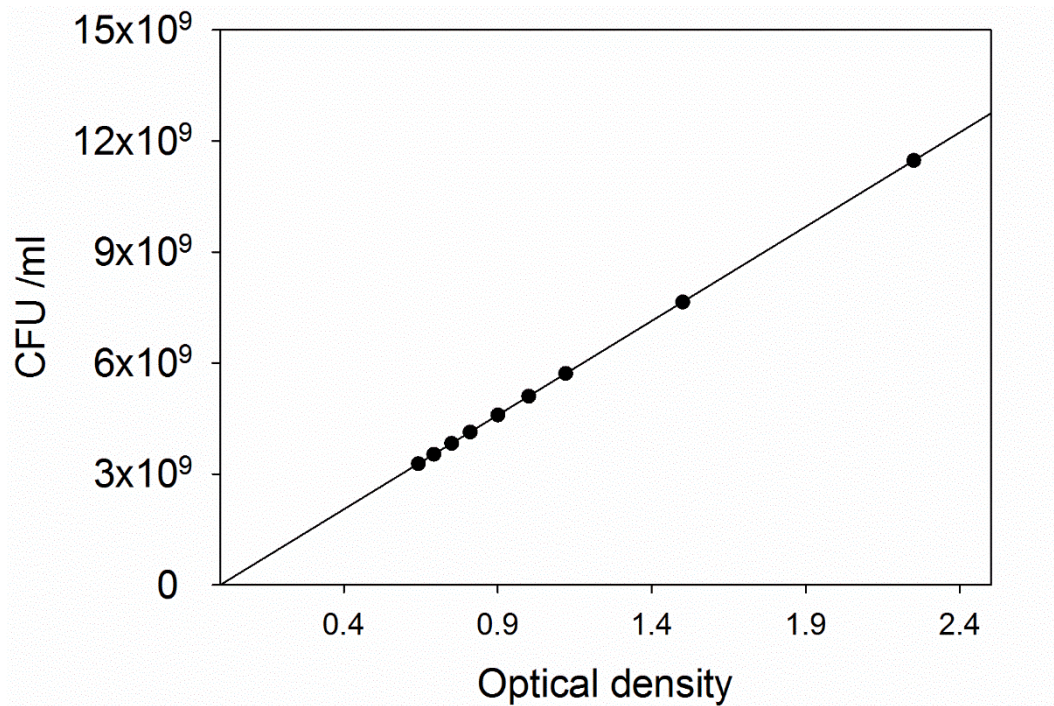


Figure 3:10 Optical density measurements corresponding to the number of colony forming units per ml.

3.3.4 *Fluorescence imaging*

To quantify the bacterial attachment on the steel samples fluorescence imaging has been carried out. DAPI (4', 6-diamidino-2-phenylindole) nucleic acid stain with vector guard has been used to stain the bacterial cells. Zeiss Axioimager 2 microscope has been used for imaging the samples. Oil immersion 63x objective with Apotome was used. Images obtained from the fluorescence microscope has been shown in Figure 3:11.

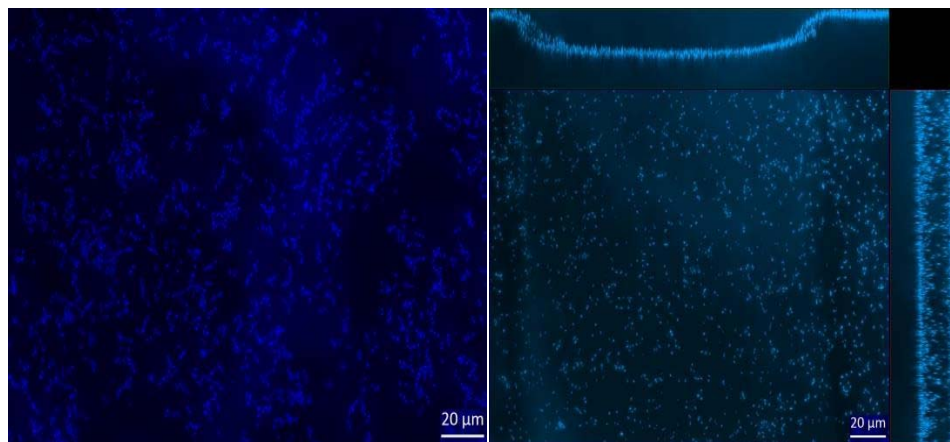


Figure 3:11 Fluorescence images of a) Plain steel samples b) 10µm channelled sample.

Figure 3:11 show attached bacteria on steel surfaces. As seen from the images there is only a monolayer of bacterial cells attached to the surfaces. Hence, microscopy was used to find the surface coverage of the attached cells. Since there is almost no overlap of bacterial cells calculating surface coverage from 2D images was easy and accurate. To confirm these further SEM images were taken to have a closer look at the attached bacteria. Five random spots were selected in each sample for imaging.

The image processing for calculating the surface coverage of the attached bacteria is carried out using MATLAB. The steps used in the image processing is given below.

- The images are imported to MATLAB as .tiff images from the microscope.
- The images are converted to grayscale, a bandpass filter is applied to reduce noise.
- The images are converted to black and white images. The surface has a dark background and the cells are white.
- From this, the area with black pixels and white pixels can be calculated and the ratio gives the surface coverage of the attached cells.
- The parameters for bandpass filter, black and white conversion are kept as constant for all the experiments.

3.3.5 ***Bacterial attachment to static conditions***

Bacterial attachment on static conditions was carried out as detailed in the methods section. The images are captured using microscopy and are processed as mentioned above. Figure 3:12 shows the bacterial attachment on three different types of samples.

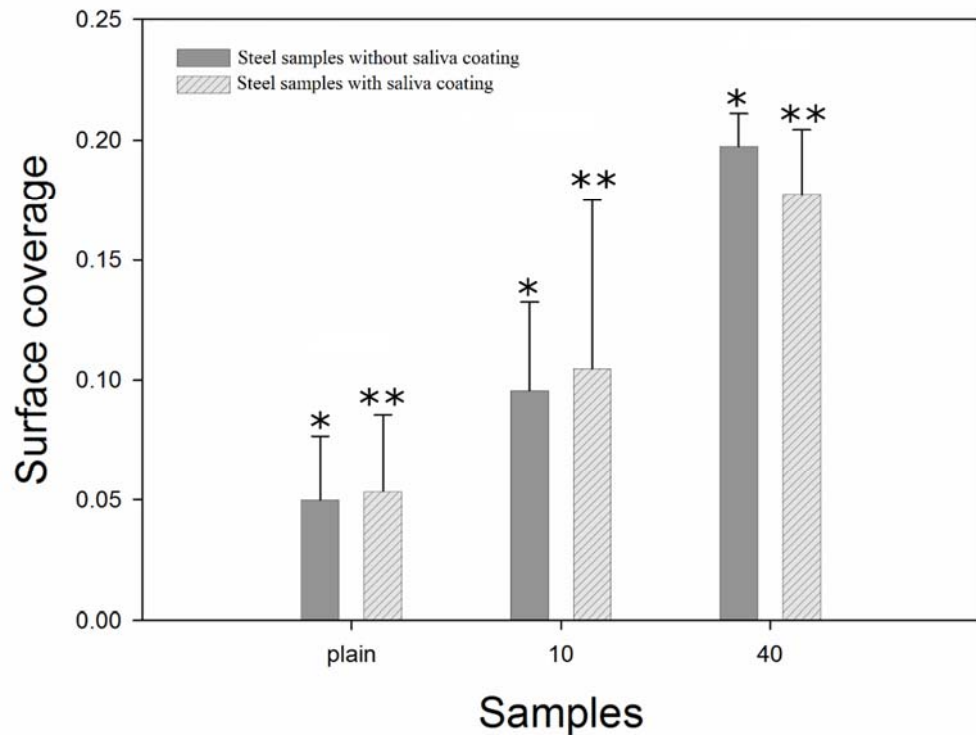


Figure 3:12 Plot showing obtained for the experiments for saliva coated and uncoated surfaces (with p values $** < 0.001$ and $** < 0.0001$, plain steel sample was kept as control and 10 μm and 40 μm channelled samples are compared). The values are mean \pm SD of three independent experiments. The difference between saliva coated and uncoated surfaces were not significant.

As seen in Figure 3:12, the attachment of bacteria to plain surfaces was lower than the channelled surfaces, which have higher roughness parameters due to chemical etching. These results are in correlation with the work by (Boyd *et al.*, 2002), where polished surface similar to the plain surfaces used in current experiments show lower bacterial attachment than the abraded steel surfaces which have higher roughness features. To check the role of conditioning film on altering bacterial attachment and modifying surface properties, an experiment was carried out under static conditions with saliva coated steel surfaces. The samples were inoculated overnight with processed human saliva and coating buffer. The samples are rinsed and the experiment was carried out on these surfaces. Bacterial attachment on saliva coated surfaces is shown in the following figure.

The data from bacterial attachment from bare surfaces and saliva coated surfaces did not show any significant difference. The significance was

calculated using one way ANOVA. It is comparable to a study by (Guan YH *et al.*, 2003) on hydroxyapatite surfaces with saliva coating. The study shows little difference in bacterial adherence on hydroxyapatite surfaces with saliva coating and bare surfaces. Another study carried out by (Lorite *et al.*, 2011) shows that the conditioning film formation due to the presence of culture medium changed surface properties like roughness and hydrophobicity. The examination of surface roughness after the application of condition layer in this case saliva was examined using AFM measurements. The data showed little difference between the surfaces without saliva. The difference might be because of fact as explained by (Lorite *et al.*, 2011), the roughness changes from 5-10 nm after 2 h and changes by 50-100 nm after 20 days. It can be observed that on a smaller time scale and large surface roughness, it has little effect on the initial attachment of bacteria. It is also observed that *S. gordonii* colonizes the oral cavity within two hours, hence the effect of conditioning film on initial attachment might not be profound.

3.3.5.1 **SEM analysis of attached bacteria**

To further observe the bacterial attachment Scanning electron microscopy (SEM) has been employed. The samples after the experiment were prepared for freeze drying. The steps used for sample preparation is given below.

- The steel samples with attached bacteria are immersed in 2% Glutaraldehyde in Sorenson's Phosphate Buffer for fixing the bacterial cells. The samples are kept overnight in 4°C.
- Dehydration of the samples is carried out by transferring the samples to 25%, 50%, 75% and 100% ethanol for 30 min till 75% ethanol and then 1 h for 100% ethanol.
- The samples are freeze-dried and gold coated for SEM imaging.

Images obtained using SEM is given in Figure 3:13.

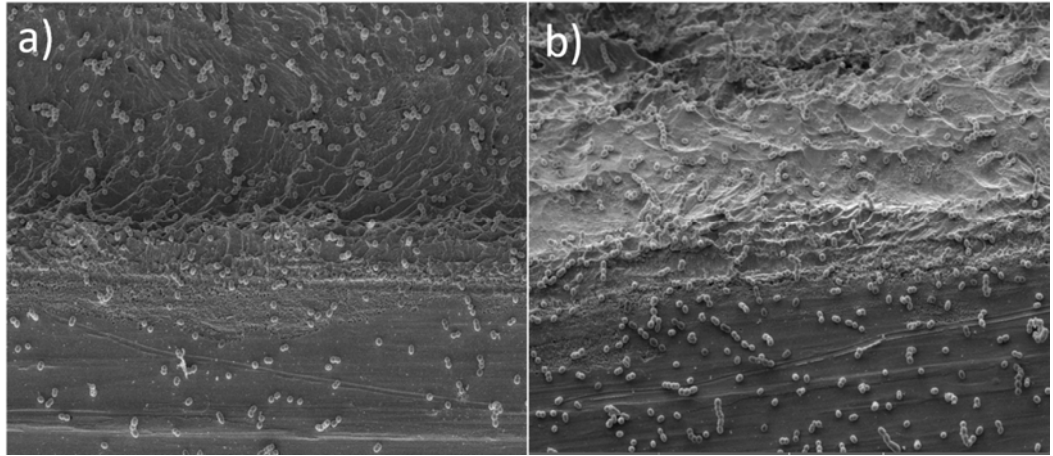


Figure 3:13 SEM images of a) 10 µm depth channel with attached bacteria the upper surface is the on the top and the channel is on the bottom. b) 40 µm depth channel with attached bacteria. The upper surface is at the bottom and the channel is at the top.

In order to validate the calculation of the results using fluorescence microscopy, the SEM images were used to count the cells per $36 \mu\text{m}^2$. The SEM images obtained at 5K resolution was used for this quantification in ImageJ. The images were divided into grids of $6 \times 6 \mu\text{m}$ and the number of cells in 6 random grids were counted. The results are shown in Figure 3:14.

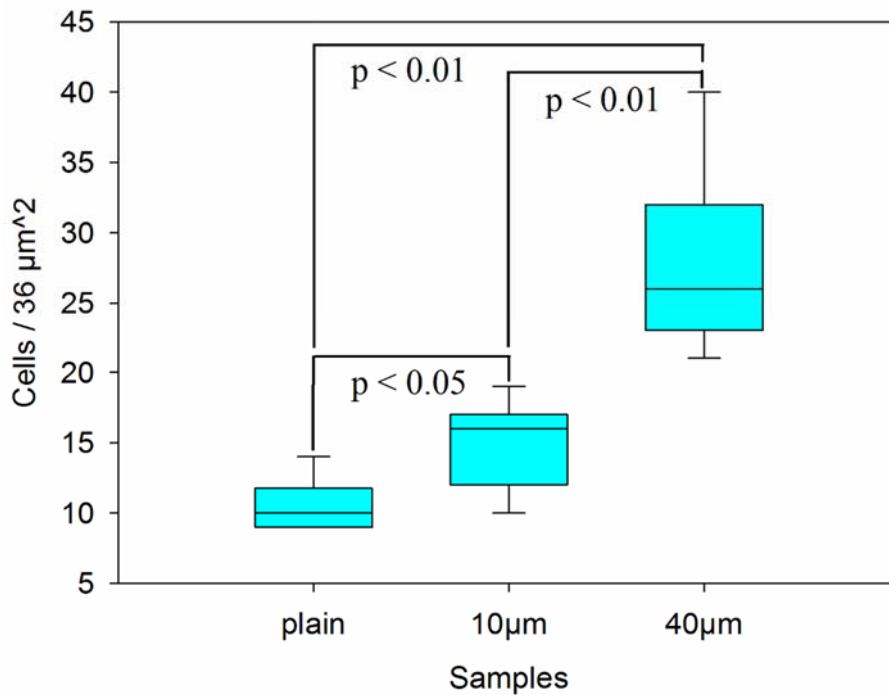


Figure 3:14 Plot showing number of attached bacterial cells on different samples. The 10 and 40 μm data is obtained from inside the channels in the samples. The values shown are median ± SD from three samples for each surface type.

The number of cells per 36 μm² for plain, 10 and 40 μm samples varied from 9-14 cells, 12-19 cells and 21-32 cells respectively. On average the number of bacterial cells attached to the 40 μm channels were higher than the other samples. It has also been observed on higher magnification, the cells attached to peaks of the roughness were considerably higher than the cells attached on the valleys of the roughness as seen in Figure 3:15. This can be explained using the XDLVO discussed in detail in chapter 4.

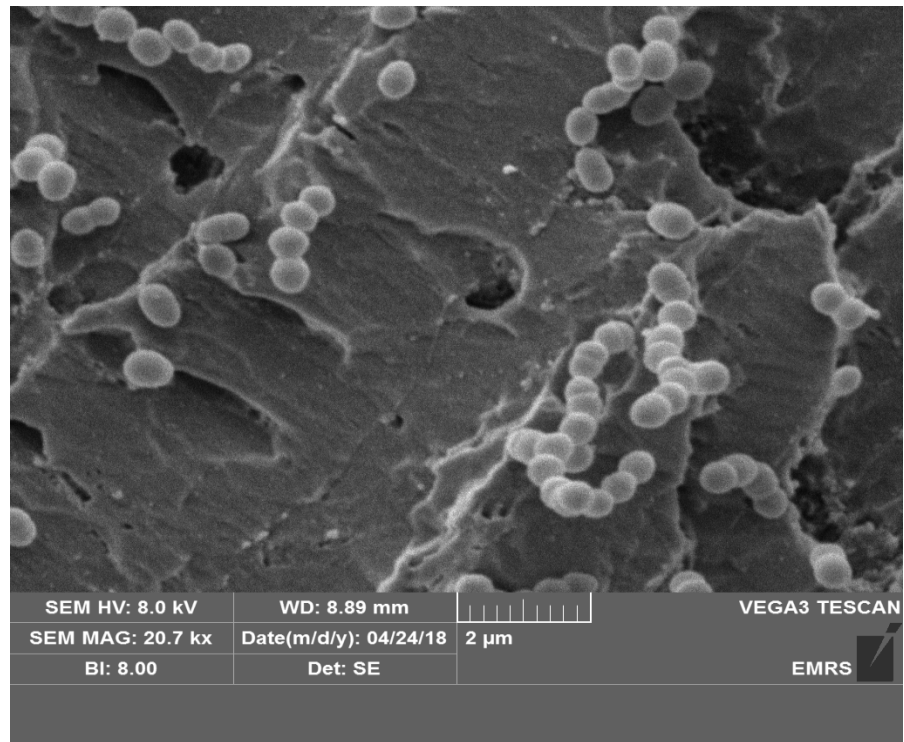


Figure 3:15 SEM image of attached bacteria on to the peaks of the rough surface. The image is obtained from highly rough 40 µm depth channels.

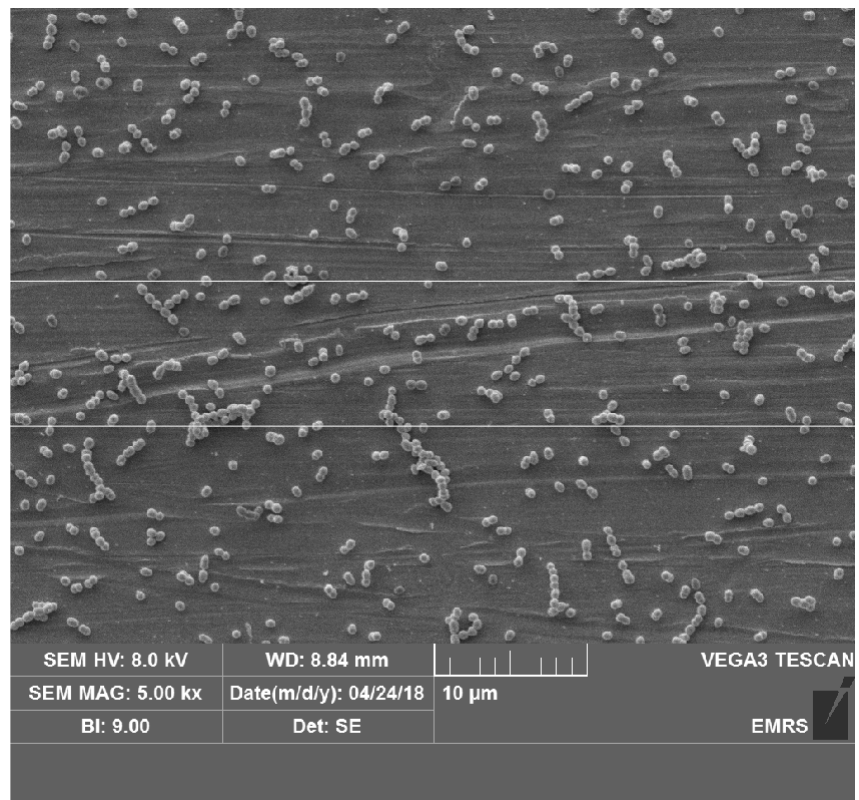


Figure 3:16 SEM image of a plain steel surface. The bacterial cells are observed to have attached randomly on the plain surfaces but along the scratches, through the surface (between the two lines) there seem to be more adhered cells.

As observed from Figure 3:16, when the number of peaks is high the bacterial cells tend to attach on the peaks. It has been observed by (Bakterij, 2014) the bacterial cells orient themselves along the natural ridges in steel surface if the feature is in the same order of the bacterium. On other parts of plain surfaces, the attachment was random. This is in correlation with the current study.

3.3.6 ***Bacterial attachment underflow***

Bacterial attachment underflow is an important condition to be studied as the environment becomes more dynamic compared to static conditions. The parameters involved in carrying the bacterial cells suspended in liquid to the surface are mainly diffusion, drag, and gravity. When the flow condition is taken into account as in most applications convection plays an important role, considering the channelled surfaces.

Experiments were carried out with three different velocities of 0.125 cm/s, 0.253 cm/s and 0.8 cm/s. The flow rate and pump rpm values for the three velocities are given in Table 3-4.

Analysis of the bacterial attachment is carried out similar to the previous study. Figure 3:17 shows the surface coverage of attached bacterial underflow velocity of 0.125 cm/s.

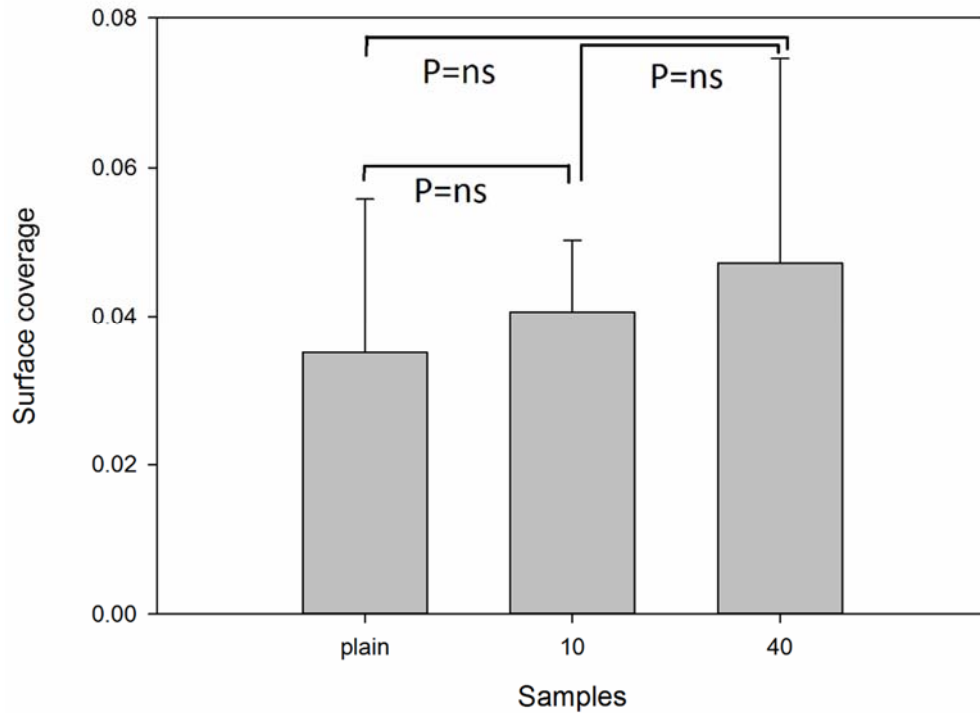


Figure 3:17 Bacterial attachment to steel samples underflow velocity of 0.125 cm/s. The bacterial attachment was uniform throughout all the surfaces and no significant (ns) difference has been observed between different samples. The values shown are mean \pm SD from three independent experiments.

The results are different from that of the attachment under static conditions. One probable reason for the uniform attachment of bacteria on all sample surfaces can be described by the addition of convection. In the case of static conditions, the bacterial cells are transported to the surface only by diffusion, whereas in this case the transportation of the bacterial cells to the surface is aided by diffusion and convection (Busscher and van der Mei, 2006). In static conditions, in addition to diffusion sedimentation is also involved in the transport of bacteria to the surface. The investigation into sedimentation has not been carried out in this study as the experiment times are 30 min in the study and the sedimentation times for bacterial cells is much longer than 30 min. The results for the experiments with a flow velocity of 0.253 cm/s are given Figure 3:18.

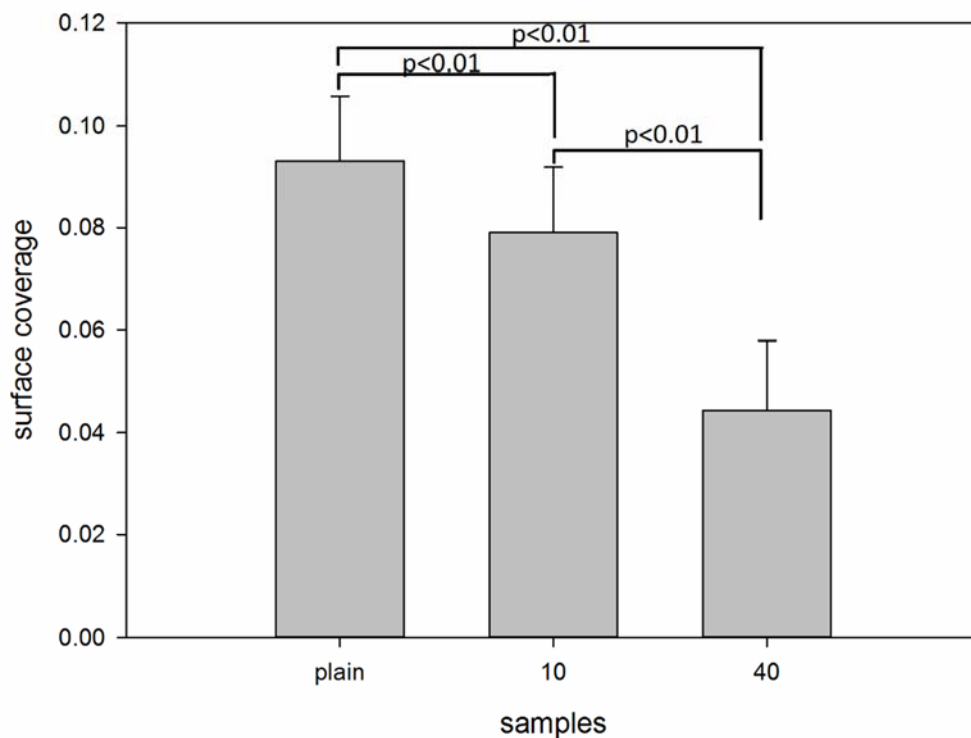


Figure 3:18 Bacterial attachment to steel samples underflow velocity of 0.253 cm/s. The statistical analysis showed a significant difference between all three sample surfaces ($p < 0.01$). The values shown are mean \pm SD from three independent experiments.

The results for the experiments under fluid velocity of 0.253 cm/s showed a more significant difference to that of the previous experiments. The data for attachment under static condition and velocity of 0.125 cm/s have higher bacterial adhesion on 40 μm followed by 10 μm and plain surfaces. In the current experiment, the trend has been reversed with 40 μm channel surfaces having the lowest bacterial adherence. The surface coverage for the plain and 10 μm surfaces have increased in this particular velocity while the attachment on 40 μm surfaces is almost the same as the coverage obtained from the previous experiment. The final experiment for bacterial attachment under fluid flow has been studied with a flow velocity of 0.8 cm/s and the results are shown in Figure 3:19. The flow velocities are chosen to be relevant to the shear rates in the oral cavity (Paramonova *et al.*, 2009).

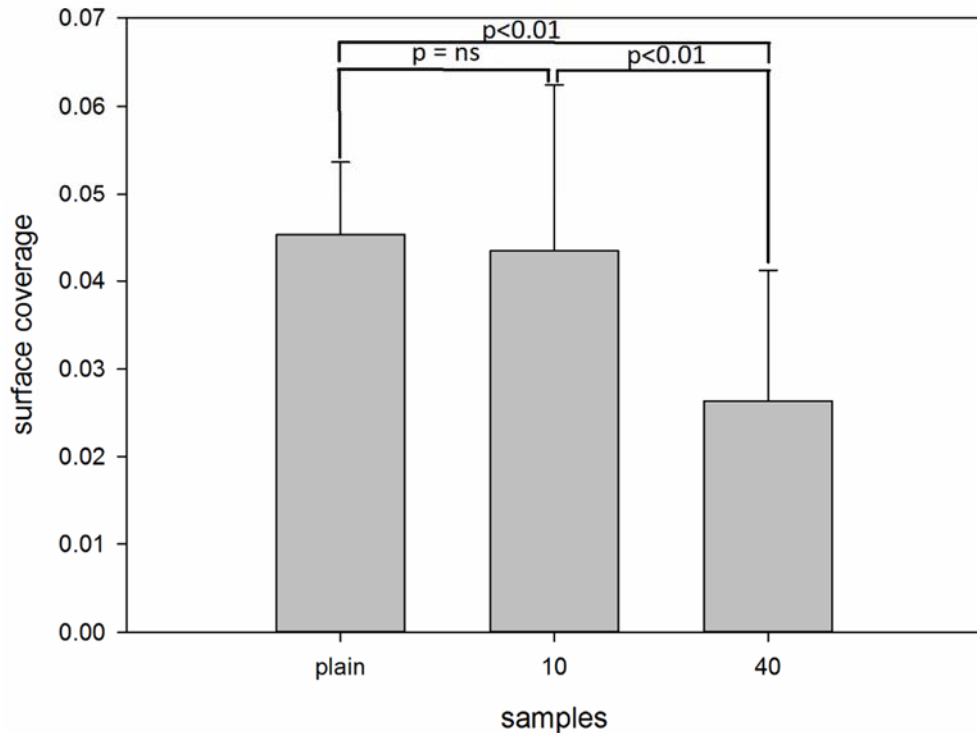


Figure 3:19 Bacterial attachment to steel samples underflow velocity of 0.8 cm/s. Statistical analysis showed no significant difference between 10 μm and other two samples, however, there was significance between plain and 40 μm samples with $p < 0.05$. The values shown are mean \pm SD from three independent experiments.

From the data, it can be observed 40 μm channels have the lowest bacterial attachment. To further understand the effect of each sample on bacterial attachment under different flow conditions, the bacterial attachment on each type of sample is compared with different flow conditions as shown in Figure 3:20. The plain and 10 μm samples at 0.125 cm/s and 0.8 cm/s showed no significant difference. On the other hand, 40 μm samples at 0.125 cm/s and 0.253 cm/s showed no significant difference.

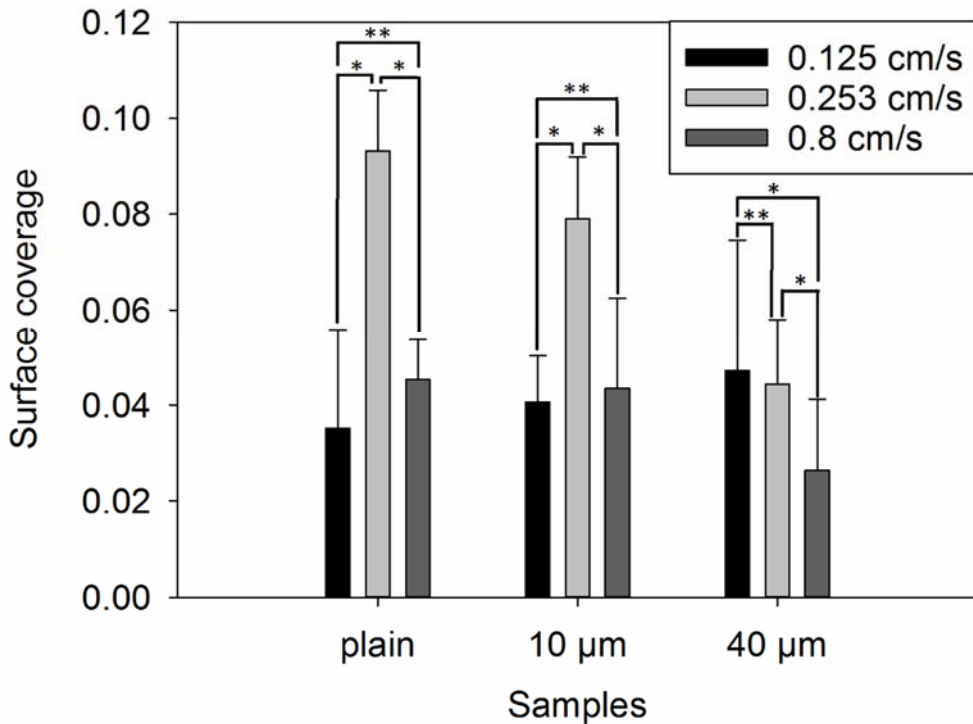


Figure 3:20 Bacterial attachment on steel samples under three different flow conditions (with p values * < 0.01 and ** = no significance). Plain and 10 µm samples did not have any significance between 0.125 cm/s and 0.253 cm/s. 40 µm samples did not show any significance between 0.125 cm/s and 0.253 cm/s. The values shown are mean ± SD from three independent experiments for each flow velocity.

From Figure 3:20 it can be seen, fluid flow has not altered the bacterial attachment on plain surfaces. In the case of 10 µm depth channels, there is a difference in surface coverage for attachment under static and flow conditions (Figure 3:12 and Figure 3:20). Statistical analysis of the data from 10 µm channelled samples shows a significant difference between the static and flow conditions in general. However, the particular flow velocity of 0.253 cm/s also shows a significant difference between the other two flow velocities, similar to the plain samples. In the case of 40 µm channelled samples, except for the velocities of 0.253 cm/s and 0.8 cm/s all other combinations show a significant difference in the data set. The varying difference in the 40 µm channelled surface has the highest surface roughness. Although for static conditions it can be argued that surface roughness has greater influence in the bacterial attachment, the presence of topographies has no impact under static conditions as the mode of bacterial transfer to the surface is only diffusion (Busscher and van der

Mei, 2006). The phenomenon behind the bacterial cells reaching the vicinity of the surface is the same for all the samples under static conditions. Once the cells reach the interaction force boundary layer as discussed in chapter 4 the effect of surface properties such as roughness and XDLVO interactions come into play and the higher rough surface influences bacterial attachment as observed. In the presence of flow over topographical features, convection of the cells plays an important role. As seen in chapter 4 the topographical features can cause recirculation regions of fluid inside the channels, thereby preventing the transport of cells. This phenomenon of recirculation in the topographies can be the main reason for the decrease in bacterial attachment in the channelled samples. As seen in the SEM images Figure 3:13 the roughness play a vital role when there is no flow. The influence of roughness can be observed from the SEM images, the number of bacterial cells per unit area is higher for surfaces with higher roughness (Figure 3:14). The results are in comparison with a study carried out by (Dantas *et al.*, 2016) where Acrylic Polymethyl Methacrylate surfaces were investigated for the attachment of oral bacteria. It has also been observed that *Streptococci* adhered stronger to rougher surfaces. This has been explained by (Mei *et al.*, 2011) as the adhesion forces and the strengthening increases with increasing roughness. As a result of this, the number of bacterial cells attached to rougher surfaces should be higher as observed in bacterial adhesion in static conditions. In another study by (Riedewald, 2006) it has been observed that the bacterial attachment increases only after an average roughness of 0.8 μm . This study contradicts the current study, as the bacterial attachment increases with the increasing roughness and the average roughness of the steel samples are well below 0.8 μm (maximum $R_a = 256 \text{ nm}$ in this study).

3.4 Conclusions

The effect of surface roughness and flow conditions on the bacterial attachment was studied in this chapter. The surface roughness, bacterial and surface properties influenced the bacterial attachment under static conditions. However, the overall trend in bacterial attachment changes under fluid flow in the micro topographies. The effect of roughness (Mei *et*

al., 2011; Abban *et al.*, 2012; Dantas *et al.*, 2016; Sharma *et al.*, 2016), surface properties (Absolom *et al.*, 1983; Balazs *et al.*, 2003; Missirlis and Katsikogianni, 2007; Tuson and Weibel, 2013) and flow conditions (Busscher and van der Mei, 2006; Bahar *et al.*, 2010; Drescher *et al.*, 2011; Lecuyer *et al.*, 2011; Molaei and Sheng, 2016) on bacterial adhesion has been studied previously, although the combination of these effects have not been studied in detail. The flow velocities in the channels and the effect of the flow in the attachment of bacteria will be investigated in detail in the next chapter using computational modelling.

4 Computational modelling of bacterial attachment on steel surfaces

4.1 Introduction

The study of bacterial attachment carried out in the previous chapter will be validated using a computational model. Computational models are a powerful tool to model bacterial interactions. In the experimental work, changing one of the parameters might change characteristics of another parameter or it will be difficult to alter individual properties. Problems such as this can be easily overcome by the use of computational models. Computational models have been used intensely to study different characteristics of a biofilm from attachment, growth, division, sensing, and detachment.

The individual-based method is one of the complex and robust methods for modelling biofilms. Individual-based models have been employed mostly in studies requiring individual bacterial properties in the community such as competition (Alpkvist *et al.*, 2006; Head *et al.*, 2017), interactions between bacteria (Jayathilake *et al.*, 2017). Although individual-based models are effective, the cost of computation increases with an increase in the number of cells. On the continuum side, the biofilm can be represented as a continuous liquid instead of individual particles. For representing individual bacteria a continuum medium can be considered as bacterial cells in the liquid and the diffusion constant can be used to represent the bacteria. Compared to the individual model a continuum model is faster, in the current study as bacteria-bacteria interactions are not considered using a continuum model will be effective. In the scope of bacterial attachment, many computational studies have been carried out using thermodynamic theory (Ista and López, 2013), Derjaguin, Landau, Verway, and Overbeek (DLVO) theory (Katsikogianni and Missirlis, 2010). Work has also been carried out to model the effect of fluid flow and diffusion, convection (El Moustaid *et al.*, 2013). Most of the studies have studied the influence of one particular property influencing attachment and not a combination of the properties. A two-dimensional model is to be developed by solving the Navier-Stokes equation in two-dimensional form. In two-dimensional form stream function-vorticity method is used to solve the Navier-Stokes equation. The effect of surface properties on the

attachment of bacteria is to be implemented using surface element integration (SEI) and extended DLVO theory.

4.2 Numerical methods

The surface roughness parameters of the steel samples measured in Chapter 3 are incorporated in the computational model by recreating the rough surface using the average roughness, root mean square value and surface area difference.

4.2.1 *Surface element integration*

A sample surface of $3 \times 3 \mu\text{m}$ was analyzed using AFM to obtain roughness parameters of the steel surfaces used in the study. The average roughness, surface area difference, and root mean square roughness is used to computationally recreate the sample surface. C++ was used as the programming tool for recreating the surface by surface element integration (SEI) and modelling bacterial attachment. The surface is recreated by distributing hemispheres of the random radii with a mean value as the average roughness of the sample. The total number of asperities is determined numerically by comparing the surface area difference of the experimental sample and the computationally recreated surface. The locations of the asperities are also selected randomly using a unit normal distribution. As the computation is carried out on a Cartesian grid of $3 \times 3 \mu\text{m}$, the locations of the asperities do not coincide with the grid locations. Hence, the recreated surface and the hemisphere locations are interpolated to the original mesh.

The evaluation of interaction energy between a rough surface and a spherical bacteria is calculated using surface element integration which is based on Derjaguin's approximation. The interactions between two spheres, according to Derjaguin's approximation were calculated as an integral of infinitesimal surface elements having a planar geometry (parallel elements) (Hoek *et al.*, 2003). The SEI technique is similar but the procedure is applied to the actual interacting bodies, the statistically developed rough surface and bacterium. The computation is carried using a cylindrical coordinate system with the origin at the bacterial center. For a spherical particle only the lower half of the particle will be exposed to the

surface, hence the calculations are carried out only for a hemisphere instead of a sphere as shown in Figure 4:1. The equation governing the SEI for calculating the interaction energy between the bacteria and surface is

$$U(D) = \int_0^{2\pi} \int_0^r U(h) r dr d\theta \quad (4.1)$$

where,

h , the vertical distance between a surface element of the bacterial surface and a point on the surface.

$U(D)$, net interaction potential between the bacteria of diameter D and the surface.

$U(h)$, the interaction energy due to XDLVO forces.

The bacteria is moved across its coordinates (x_c, y_c) over the rough surface with coordinates (x_i, y_i) at the mean distance D . At each location of the bacteria centre, the projected area of the bacteria over the recreated rough surface is determined using the inequality,

$$(x_i - x_c)^2 + (y_i - y_c)^2 < (a + a_i)^2 \quad (4.2)$$

where,

a_i , the radius of the i^{th} asperity

a , the radius of the bacteria.

The interaction energy is calculated for the asperities which are satisfied by the equation above. The height h between the particle and surface is calculated in Cartesian coordinates as below.

$$h = D + a - \sqrt{a^2 - r^2} - \sqrt{a_i^2 - r_i^2} \quad (4.3)$$

$$h = D + a - \sqrt{a^2 - r^2} + \sqrt{a_i^2 - r_i^2} \quad (4.4)$$

$$h = D + a - \sqrt{a^2 - r^2} \quad (4.5)$$

where,

r_i , the radial distance between the asperity centre and surface

The equation 4.3 above is used to find the vertical distance between bacteria surface and rough surface when there is a protrusion directly below and equation 4.4 to find the distance when there is a depression below. When the surface is flat without any asperities the equation 4.5 is used.

The equations 4.3 and 4.4 should be employed only when the bacterial surface does not overlap with the space occupied by a protrusion or depression. This condition is given by the following equation

$$(x - x_i)^2 + (y - y_i)^2 > a_i^2 \quad (4.6)$$

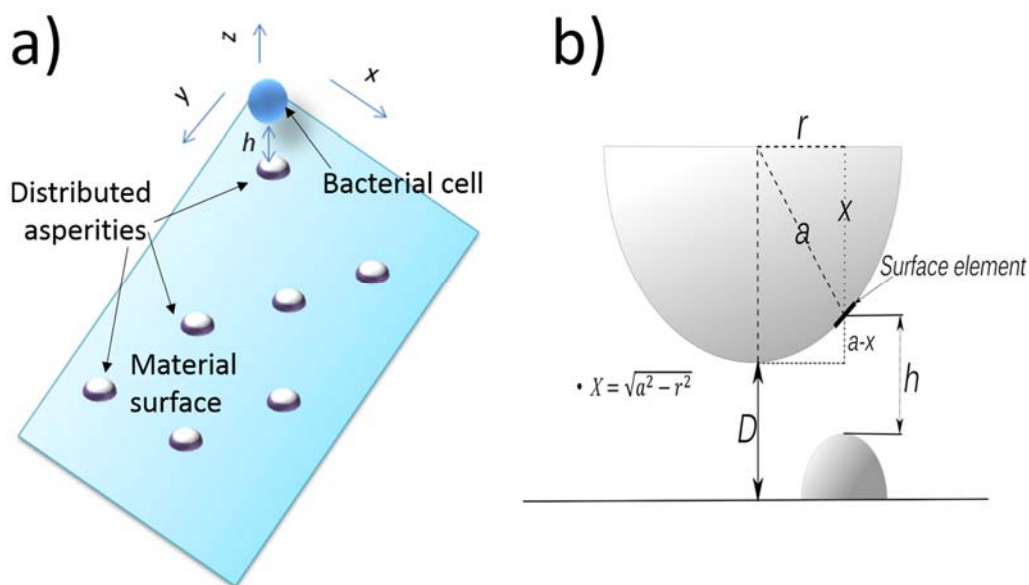


Figure 4:1 (a) Schematic diagram of a bacterial cell and computationally recreated material surface. (b) Schematic diagram showing the calculation of separation distance between an approaching particle and asperity on the surface.

The separation distance h between the bacteria and the surface is calculated according to the above Figure 4:1 and using the equations 4.3 – 4.6. The separation distance calculated is used to calculate the interaction energy of the discrete surface element with the surface. The process of calculating the total interaction energy for a bacterial cell is carried out for the lower side of the bacteria for $r = 0$ to a (radius of bacteria).

4.2.2 XDLVO theory

The total interaction energy required for bacteria to adhere to surfaces is calculated based on extended DLVO theory (Van Oss, 1989). The

interaction energy is expressed as a sum of Lifshitz Van Der Waals (LW) interactions, Electrostatic (EL) interactions, and Acid-base (AB) interactions as

$$\Phi_{bls} = \Phi_{bls}^{LW} + \Phi_{bls}^{EL} + \Phi_{bls}^{AB} \quad (4.7)$$

4.2.2.1.1 Lifshitz Van Der Waals potential

The Van Der Waals interactions include three interactions namely Keesom (dipole-dipole), Debye (dipole-induced dipole) and London (induced dipole-induced dipole) interactions. The net interaction potential due to Van Der Waals forces is given by the equation

$$\Phi^{LW}(h) = -\frac{A_h}{12\pi h^2} \quad (4.8)$$

where,

$$A_h = -12\pi h_0^2 \Delta G_{LW}, \text{ the Hamaker constant (Joule)} \quad (4.9)$$

$h_0 = 0.158$ nm, the minimum separation distance due to Born repulsion and

$$\Delta G_{LW} = 2 \left(\sqrt{\gamma_l^{LW}} - \sqrt{\gamma_s^{LW}} \right) \left(\sqrt{\gamma_b^{LW}} - \sqrt{\gamma_l^{LW}} \right) \quad (4.10)$$

ΔG_{LW} , is the Lifshitz Van Der Waals free energy per unit area between the substrate (s) and bacteria (b) immersed in a liquid (l). The subscripts l, s, b represent the liquid, substrate and bacteria respectively.

4.2.2.1.2 Acid-Base interaction potential

The acid-base interactions consist of electron-donor, electron-acceptor and hydrophobic and hydrogen bonding interactions. The interaction potential as a result of these acid-base interactions are given by

$$\Phi^{AB}(h) = \Delta G_{AB} \exp\left(\frac{h_0 - h}{\lambda}\right) \quad (4.11)$$

where,

$$\begin{aligned}\Delta G_{AB} = & 2\sqrt{\gamma_1^+}(\sqrt{\gamma_s^-} + \sqrt{\gamma_b^-} - \sqrt{\gamma_1^-}) \\ & + 2\sqrt{\gamma_1^-}(\sqrt{\gamma_s^+} + \sqrt{\gamma_b^+} - \sqrt{\gamma_1^+}) \\ & - 2\left(\sqrt{\gamma_s^+\gamma_b^-} + \sqrt{\gamma_s^-\gamma_b^+}\right)\end{aligned}\quad (4.12)$$

The acid-base free energy per unit area between bacteria and surface γ_b^- and γ_b^+ are the bacterial electron donor, electron acceptor surface tension parameters.

These values can be obtained using the contact angle analysis by

$$\gamma_1(1 + \cos\theta) = 2\sqrt{\gamma_1^{LW}\gamma_b^{LW}} + 2\sqrt{\gamma_b^+\gamma_1^-} + \sqrt{\gamma_b^-\gamma_1^+} \quad (4.13)$$

$$\gamma_1 = \gamma_1^{LW} + \gamma_1^{AB} \quad (4.14)$$

$\gamma_1^{AB} = 2\sqrt{\gamma_b^+\gamma_b^-}$ The Lewis acid base surface tension component.

The bacterial surface tension parameters are obtained by solving the above equation and the acid-base free energy is obtained.

$\lambda \cong 1$ nm, characteristic decay length of acid base interactions in water.

4.2.2.1.3 Electrostatic interaction potential

The electrostatic interactions result from the overlapping electrical double layers between the surface and the bacterium and it is given by the equation

$$\Phi^{EL}(h) = \varepsilon\varepsilon_0\psi_b\psi_s \left[\frac{\psi_b^2 + \psi_s^2}{2\psi_b\psi_s} (1 - \coth(kh)) + \frac{1}{\sinh(kh)} \right] \quad (4.15)$$

where,

$\varepsilon_0 = 8.854 \times 10^{-12}$, Permittivity of vacuum in C. V⁻¹. m⁻¹

$\varepsilon = 78.5$, relative permittivity of water at 25 degree Celsius.

ψ_b, ψ_s , the zeta potential of the bacterial cell (b) and surface (s) in mV

k , the inverse Debye screening length in m⁻¹.

The zeta potentials and surface tension parameters can be obtained experimentally or from literature for different types of surfaces and bacterial cells (Ammar *et al.*, 2015; Cao *et al.*, 2018). The total interaction energy thus can be expressed as the sum of three interactions.

4.2.3 **Navier-Stokes equation**

Navier-Stokes equation in stream function-vorticity form has been solved using the finite difference method for fluid flow over the surfaces. By using this method the three primitive variables (velocities in two dimensions and pressure) are not directly solved but are obtained by solving stream function and vorticity. The current study is carried out in 2D and the equations have to be solved only for the velocity terms and pressure term from Navier-Stokes equations is not required. As Stream function vorticity method allows easier interpretation of the results as the pressure term doesn't have to be solved in this form and computationally it is less expensive as only two equations have to be solved instead of three equations using primitive variables for two dimensions.

4.2.3.1 **Vorticity, ω**

Vorticity is a measure of the local spin of a fluid element and it is the difference between the gradients of flow in the two directions for a 2D flow. In a two dimensional flow the vorticity vector is perpendicular to the direction of the fluid flow. It can be represented as

$$\omega = \frac{\partial v}{\partial x} - \frac{\partial u}{\partial y} \quad (4.16)$$

4.2.3.2 **Stream-function, Ψ**

A Streamline is the path traced by a massless particle as it moves along the flow of the fluid. Stream function is constant along each streamline of a non-divergent flow. The velocity components can be expressed as derivatives of scalar stream function such as,

$$u = -\frac{\partial \Psi}{\partial y} \text{ and } v = \frac{\partial \Psi}{\partial x} \quad (4.17)$$

The Navier-Stokes equation, in two-dimensional form, can be written as,

Momentum for x-direction in 2D

$$\rho \left[\frac{\partial u}{\partial t} + u \frac{\partial u}{\partial x} + v \frac{\partial u}{\partial y} \right] = -\frac{\partial p}{\partial x} + \mu \left(\frac{\partial^2 u}{\partial x^2} + \frac{\partial^2 u}{\partial y^2} \right) \quad (4.18)$$

Momentum for y-direction in 2D

$$\rho \left[\frac{\partial v}{\partial t} + u \frac{\partial v}{\partial x} + v \frac{\partial v}{\partial y} \right] = -\frac{\partial p}{\partial y} + \mu \left(\frac{\partial^2 v}{\partial x^2} + \frac{\partial^2 v}{\partial y^2} \right) \quad (4.19)$$

The continuity equation is expressed as,

$$\frac{\partial u}{\partial x} + \frac{\partial v}{\partial y} = 0 \quad (4.20)$$

On applying partially derivation by $\frac{\partial}{\partial y}$ to equation (4.19) and $\frac{\partial}{\partial x}$ to equation (4.21) and subtracting the equations, we get

$$\begin{aligned} \rho \left[\frac{\partial}{\partial t} \left(\frac{\partial u}{\partial y} - \frac{\partial v}{\partial x} \right) + u \frac{\partial}{\partial x} \left(\frac{\partial u}{\partial y} - \frac{\partial v}{\partial x} \right) + v \frac{\partial}{\partial y} \left(\frac{\partial u}{\partial y} - \frac{\partial v}{\partial x} \right) \right] \\ = \mu \frac{\partial^2}{\partial x^2} \left(\frac{\partial u}{\partial y} - \frac{\partial v}{\partial x} \right) + \mu \frac{\partial^2}{\partial y^2} \left(\frac{\partial u}{\partial y} - \frac{\partial v}{\partial x} \right) \end{aligned} \quad (4.21)$$

Substituting, the equation (4.16), the expression for vorticity in equation (4.21), we can arrive at the vorticity transport equation as

$$\rho \left[\frac{\partial \omega}{\partial t} + u \frac{\partial \omega}{\partial x} + v \frac{\partial \omega}{\partial y} \right] = \mu \left[\frac{\partial^2 \omega}{\partial x^2} + \frac{\partial^2 \omega}{\partial y^2} \right] \quad (4.22)$$

The velocity terms u and v in the above equation can be represented in terms of stream function as in equation (4.17), thus removing the primitive terms from the above equation.

$$\rho \left[\frac{\partial \omega}{\partial t} + \frac{\partial \Psi}{\partial y} \frac{\partial \omega}{\partial x} - \frac{\partial \Psi}{\partial x} \frac{\partial \omega}{\partial y} \right] = \mu \left[\frac{\partial^2 \omega}{\partial x^2} + \frac{\partial^2 \omega}{\partial y^2} \right] \quad (4.23)$$

From equation (4.17), on partially deriving u component by x and partially deriving v component by y and subtracting the two resulting equations, we arrive at

$$\frac{\partial^2 \Psi}{\partial x^2} + \frac{\partial^2 \Psi}{\partial y^2} = \frac{\partial v}{\partial x} - \frac{\partial u}{\partial y} = \omega \quad (4.24)$$

The equations (4.23) and (4.24) are collectively known as the stream function-vorticity formulation for the 2D Navier-Stokes equation. The above equation is solved and the velocity can be derived using the stream function equation. The fluid field is calculated using discretizing the equations (4.23) and (4.24) and solving using finite difference method.

4.2.4 *Diffusion – convection*

The continuum model for bacterial attachment and nutrient transfer to the biofilm are to be modelled using diffusion-convection equation.

To start with studying the bacterial adhesion using XDLVO theory, diffusion equation is solved where bacteria is represented by the concentration of the medium. By this method, individual bacteria is not analyzed and a continuum approach is carried out. The bacterial cells present in the medium is represented as the concentration of the liquid and the diffusion coefficient D is calculated as

$$D = \frac{kT}{6\pi\mu r} \quad (4.25)$$

where,

r, radius of the particle

μ , viscosity

k, Boltzmann's constant and t the temperature.

The diffusion-convection reaction is represented using the following equation

$$\frac{\partial c}{\partial t} = \nabla(D \cdot \nabla c) - \nabla(\vec{u} \cdot c) + R \quad (4.26)$$

where,

c , concentration

\vec{u} , velocity

R , reaction term.

4.2.5 *Finite difference method.*

The Navier-Stokes equation and diffusion-convection equations have to be discretized in order to arrive at the numerical solutions. The finite difference method is selected for this study. The computational domain is divided into a uniform Cartesian grid as in the following Figure 4:2. In order to solve a partial differential equation, at node (i, j) the value is approximated from the neighbouring grid values by the use of Taylor's theorem. Therefore, the initial and boundary conditions for the problem must be defined correctly in order to define the problem clearly.

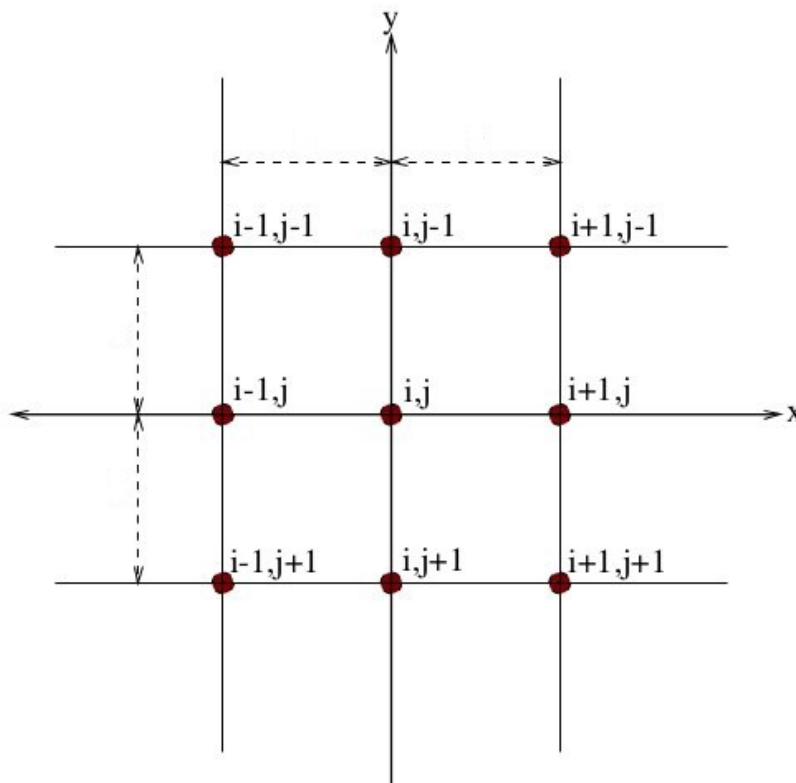


Figure 4:2 An uniform Cartesian grid used to discretize the computational domain.

By using the finite difference method, the solution for a partial differential equation can be calculated by different differencing methods as shown below.

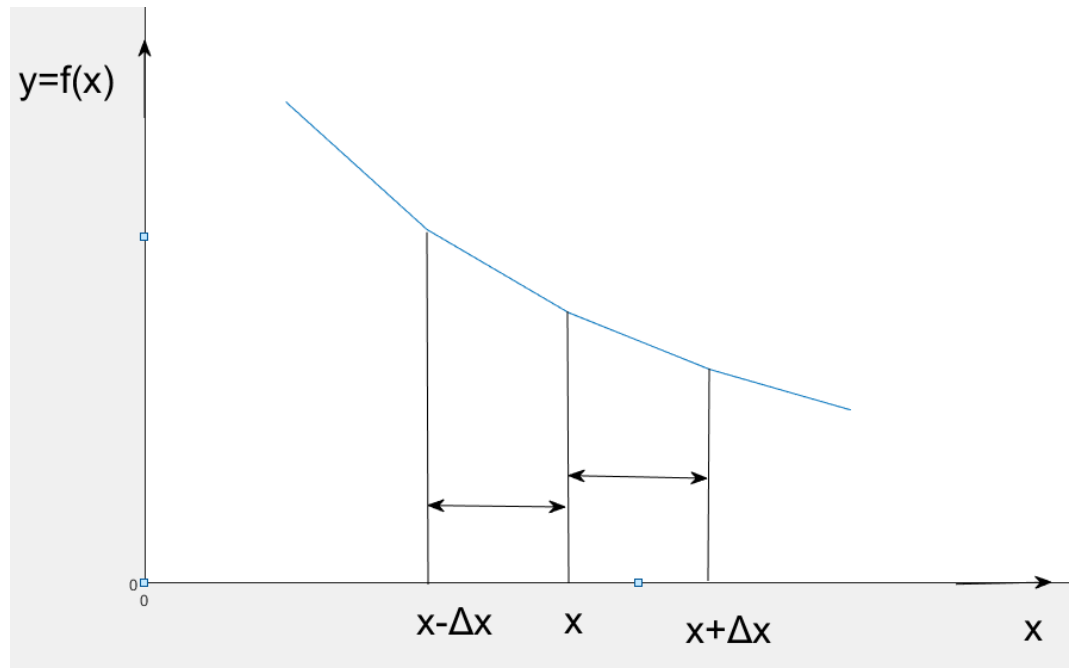


Figure 4:3 A simple function y plotted against x describing the finite difference method.

In the forward finite difference, the derivative at the current step x can be calculated using the value at the next step $x + \Delta x$ using Taylor's series as shown

$$f(x + \Delta x) = f(x) + \Delta x f'(x) + \frac{\Delta x^2}{2!} f''(x) + O(\Delta x^3) \quad (4.27)$$

$$f'(x) = \frac{f(x + \Delta x) - f(x)}{\Delta x} + O(\Delta x^2) \quad (4.28)$$

Similarly, the derivative of the function can be calculated by using the previous value $x - \Delta x$ can be calculated called the backward finite difference, using Taylor series

$$f(x - \Delta x) = f(x) - \Delta x f'(x) + \frac{\Delta x^2}{2!} f''(x) + O(\Delta x^3) \quad (4.29)$$

$$f'(x) = \frac{f(x) - f(x - \Delta x)}{\Delta x} + O(\Delta x^2) \quad (4.30)$$

By subtracting equation (4.27) and equation (4.29), by use of both the next and previous steps the derivative can be obtained by the central difference method.

$$f'(x) = \frac{f(x + \Delta x) - f(x - \Delta x)}{2\Delta x} + O(\Delta x^2) \quad (4.31)$$

Similarly, the second order derivative can be solved by adding the equations equation (4.27) and equation (4.29) as shown below.

$$f(x + \Delta x) + f(x - \Delta x) = 2f(x) + \Delta x^2 f''(x) + O(\Delta x^3) \quad (4.32)$$

$$f''(x) = \frac{f(x + \Delta x) - 2f(x) + f(x - \Delta x)}{\Delta x^2} + O(\Delta x^3) \quad (4.33)$$

By using the above equations, the first and second order partial derivate in time and length can be solved.

4.2.6 **Bacterial adhesion**

Bacterial deposition using diffusion equation is modelled using XDLVO theory. The effect of XDLVO theory is imposed in terms of the reaction term in the diffusion equation (Ammar *et al.*, 2015). The modified diffusion-convection equation is given by

$$\frac{\partial c}{\partial t} = \nabla \cdot (D \cdot \nabla c) - \nabla \cdot (\vec{u} \cdot c) + \nabla \cdot \left(\frac{Dc}{kT} \nabla \phi \right) \quad (4.34)$$

where,

\vec{u} , the velocity of the liquid inside the channel

ϕ , the interaction energy for adhesion.

The region of interaction energy is of the order of Debye length. This region is referred to as an interaction force boundary layer (IFBL) as in Figure 4.4. The thickness of the interaction force boundary layer is very

thin compared to the diffusion boundary layer δ_D the order of this diffusion boundary layer is given by

$$S_c^{1/3} \delta_\theta \quad (4.35)$$

where,

S_c , Schmidt number.

δ_θ , viscous boundary layer.

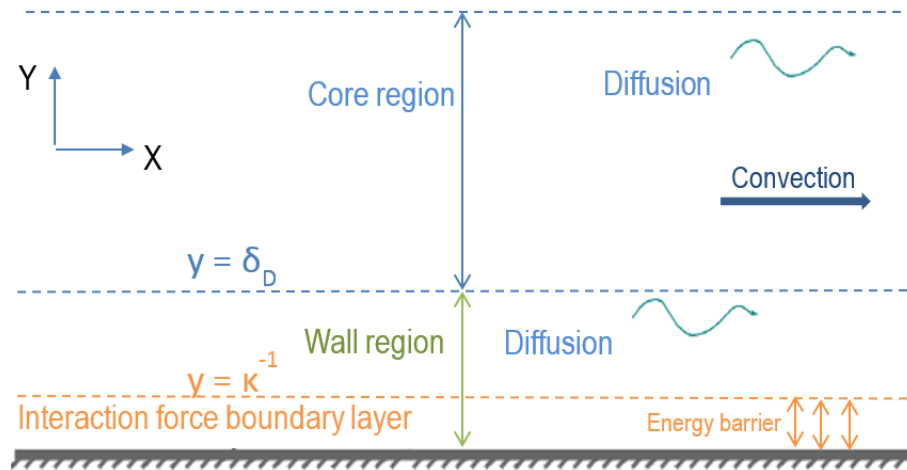


Figure 4:4 Representation of interaction force boundary layer (IFBL) and diffusion and convection (Ammar *et al.*, 2015).

As this region of adhesion is very small compared to the height of the channel, the convective flux in the wall region is neglected and assuming a steady state, the equation (4.34) can be written as

$$\nabla \cdot \left(D \nabla c + \frac{Dc}{kT} \nabla \phi \right) = 0 \quad (4.36)$$

For the wall region, $\frac{\partial^2 c}{\partial x^2} \ll \frac{\partial^2 c}{\partial y^2}$, the above equation can be written as,

$$\frac{\partial}{\partial y} \left(D \frac{\partial c}{\partial y} + \frac{Dc}{kT} \frac{\partial \phi}{\partial y} \right) = 0 \quad (4.37)$$

Integrating the equation,

$$\left(D \frac{\partial c}{\partial y} + \frac{Dc}{kT} \frac{\partial \phi}{\partial y} \right) = j(x) \quad (4.38)$$

The equation is a first-order reaction at the wall as,

$$j(x) = -K_d c_0 \quad (4.39)$$

where, $c_0 = (x, y = 0)$ the concentration at the wall, the rate constant K_d is given by,

$$K_d = \frac{D}{\int_0^\delta [\alpha e^{\phi/kT} - 1] dy} \quad (4.40)$$

a, Stokes correction factor as given by (Bowen *et al.*, 1976)

$\delta \cong \delta_D$, thickness of the wall layer

The flux of the bacterial cells arriving at the interaction force boundary layer is mainly due to diffusion, motility, and gravity as convection is very negligible at this boundary layer

$$-K_d c_0 = -D \frac{\partial c}{\partial y} + (u_s + u_m) c_0 \quad (4.41)$$

The concentration gradient near the wall (at $y = 0$) in the above equation can be further approximated as

$$\frac{\partial c}{\partial y} \cong \frac{c_\delta - c_0}{\delta} \quad (4.42)$$

where, $c_0 = c_\delta \beta$

$$\beta = \frac{D}{\delta \left(K_d + \frac{D}{\delta} \right)} \quad (4.43)$$

4.2.6.1 **Numerical steps**

- The fluid flow for the required flow channel is computed by solving Navier-Stokes equations as discussed above.
- The diffusion-convection equation without the reaction term in equation (4.34) is solved for the entire flow channel.
- The bacterial deposition using XDLVO theory is imposed in the model using the boundary condition for the wall concentration c_0 .
- Periodic boundary conditions are to be used for inlet and outlet of the channel as only a small section of the channel is simulated.

4.3 Results and discussion

4.3.1 Simulation of bacterial deposition in static conditions

The diffusion-convection equation with zero boundary conditions represents a bacterial adhesion process. With this condition, the deposition rate was higher than the experimental results from the literature. Hence XDLVO theory was used as explained in the Numerical method section and the interaction energy from the XDLVO theory was imposed in terms of the rate constant in the boundary condition for the lower wall of the channel. The interaction energy between bacteria and rough surface is calculated as mentioned below.

The rough surface is recreated from the average roughness, SAD parameters from the AFM measurements. Hemispheres were spread out on the recreated surface. The radii of the asperities were normally distributed with the mean of the average roughness. The number of asperities is decided by the SAD. The histogram of the distribution of asperities is given Figure 4:5.

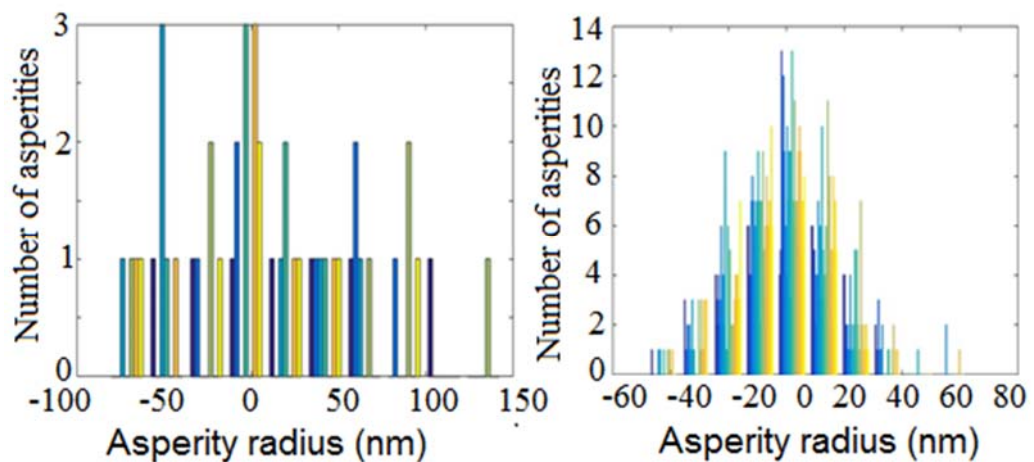


Figure 4:5 Histogram showing the distribution of asperities for surface recreation a) SAD= 3.15% and Ra=10.5 nm b) SAD=3.15% and Ra = 45.24 nm. The positive radius represents the protrusions (convex surfaces) above the mean plane and negative radius represents the depressions (concave surfaces) below the mean plane of the samples.

From the above histograms it can be seen that for the same SAD and lower Ra, the surface has many rough features with smaller valleys and peaks and for same SAD and higher Ra the rough features are less but the valleys and peaks are higher. This creates the changes in the overall

potential of the surface. For a smooth surface the interaction potential is constant throughout the surface, but the interaction changes with the roughness dimensions for the rough surfaces.

	Plain Steel samples		Steel samples with 10 μm channels		Steel samples with 40 μm channels	
	AFM	Simulation	AFM	Simulation	AFM	Simulation
Average roughness (nm)	46.95	45.24	55.81	56.62	255.93	254.87
RMS Roughness (nm)	54.52	53.95	71.06	69.28	304.74	303.76
Surface area difference (%)	3.15	3.15	7.54	7.539	29.35	29.27

Table 4-1 Experimental roughness parameters obtained using atomic force microscopy (AFM) and re-created surface roughness parameters by simulation.

The interaction energy between the bacteria and the rough recreated surface is calculated as described in the numerical section. The interaction energy for different rough surfaces is given in Figure 4:6.

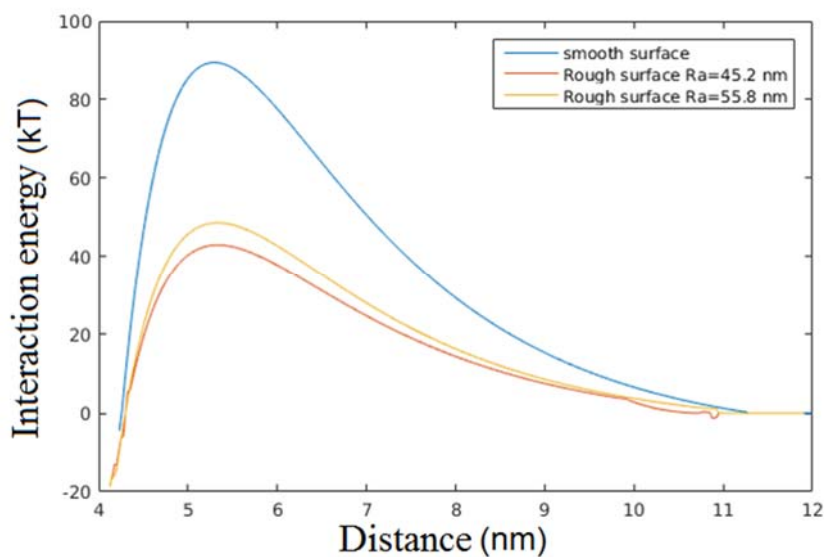


Figure 4:6 Interaction energy curves for different average roughness at an ionic strength of 20 mM and zeta potential of 10 mV

4.3.1.1 Surface energy and zeta potential measurements

The surface energy components of bacteria and zeta potentials were calculated as mentioned in the experiments section. The table of values is shown in Table 4-2. These experimental values are used in the numerical model.

	Zeta potentials, mV	Acid component, γ_1^+ (mJ/m ²)	Lifshitz-Van der Waals component, γ_1^{LW} (mJ/m ²)	Base component, γ_1^- (mJ/m ²)
Stainless steel	-25.00	41.4	0.04	3.14
Bacteria	-10.0	25.26	0.430	4.686

Table 4-2 Zeta potentials and surface tension values of bacteria and stainless steel

In addition to surface roughness, the zeta potentials and ionic strength of the bacteria, surface, and liquid also have a high impact on the interaction energy. With the increase in roughness, the height of the interaction barrier is reduced. The zeta potential and ionic strength change the location of the interaction barrier. The following graph shows the interaction energy as a function of separation height for different zeta potentials of the bacteria.

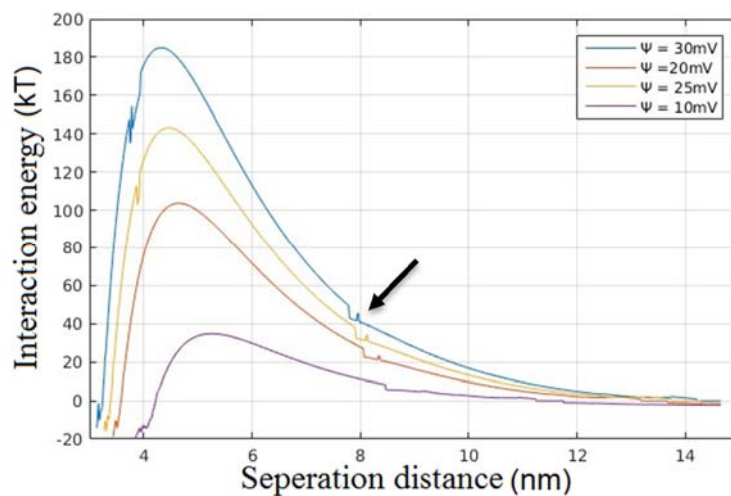


Figure 4:7 Interaction energy curves for different zeta potentials of the bacteria using ionic strength of 20 mM and average roughness as 55.8 nm. The arrow shows temporary fluctuations in the interaction energy.

From Figure 4:7 it can be seen that the changes in zeta potential shift the interaction barrier of the system.

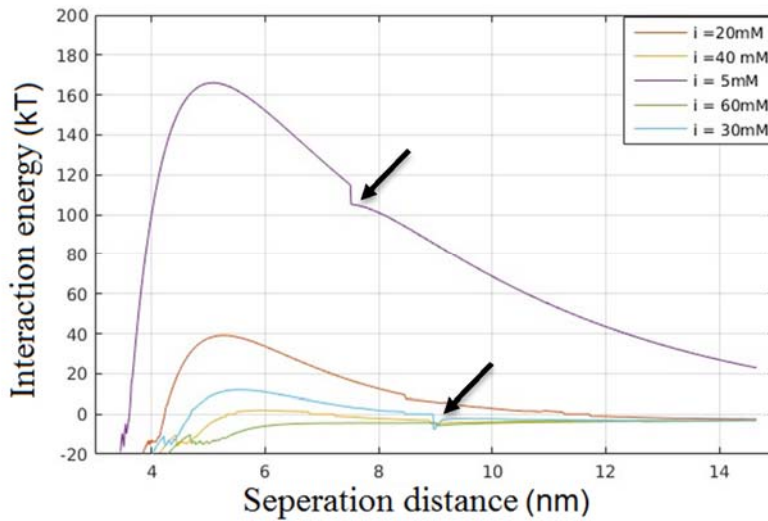


Figure 4:8 Interaction energy curves for different ionic strengths using zeta potential of bacteria as -10 mV and average roughness as 55.8 nm. The arrows shows temporary fluctuations in the interaction energy.

From the

Figure 4:8 it can be seen that the ionic strength of the liquid medium also has greater effects in the total interaction energy (Janjaroen *et al.*, 2013; Ammar *et al.*, 2015). As the ionic strength of the medium increases to 60 mM, there are no repulsive forces but only attractive forces are present. The above two effects due to the zeta potential and ionic strength are the result of changes in electrostatic potentials. The fluctuations in the curves as shown using the arrows in Figure 4:7 and Figure 4:8 are not caused due to the step size or grid size used in the finite difference method. It might be due to the presence of large asperities which can cause temporary fluctuations in the calculated net potential.

4.3.2 **Bacterial deposition on sample surfaces**

The diffusion-convection equation in combination with the SEI technique and XDLVO theory has been used to compute the bacterial deposition on different surfaces. The developed codes are first validated with known literature to determine if the computation is carried out correctly.

4.3.2.1 Validation of the computational code

The Navier-Stokes equation solved in stream function-vorticity method using finite difference method was used to compute lid-driven cavity flow and the results were compared with the work carried out by (Aydin and Fenner, 2001). The schematic representation of the lid-driven cavity flow and boundary conditions used are shown in Figure 4:9.

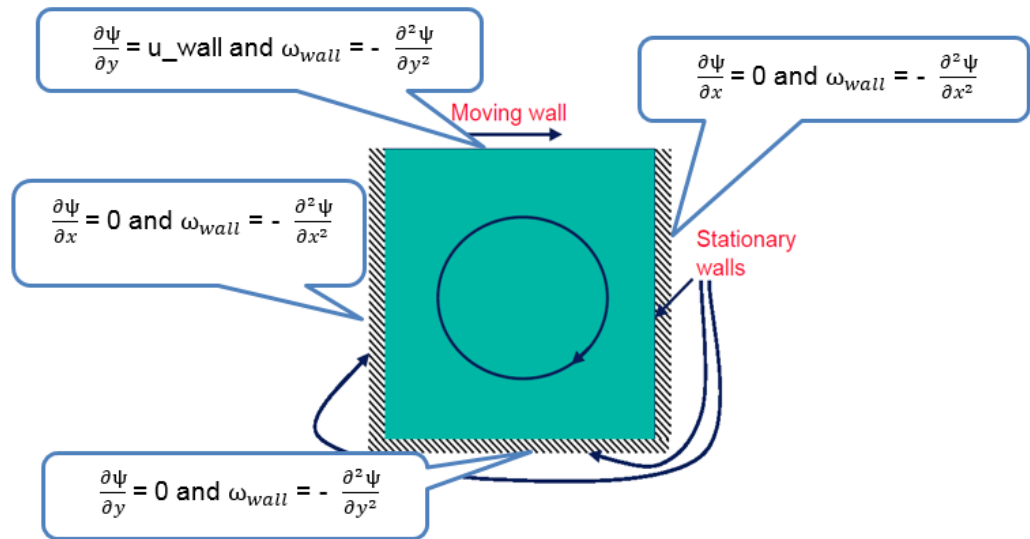


Figure 4:9 Schematic representation of the lid-driven cavity flow and different boundary conditions used at the walls.

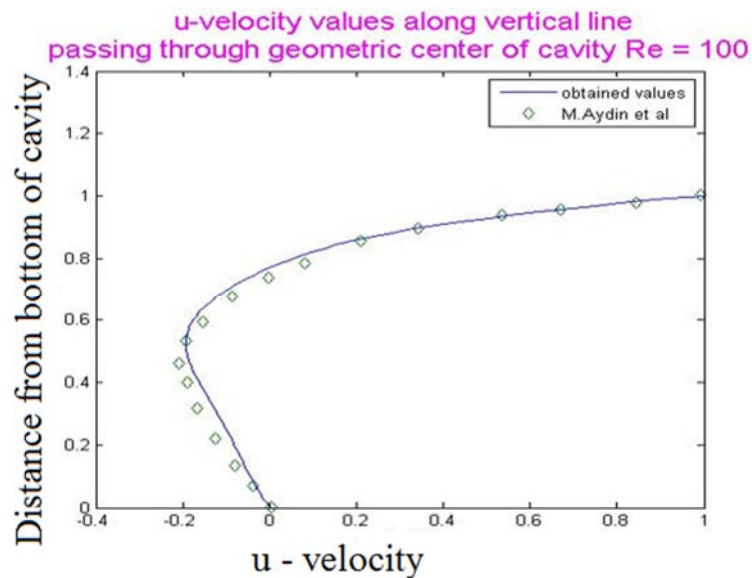


Figure 4:10 Velocity of the fluid in the direction of the moving wall along the vertical line passing through the centre of the cavity was derived and compared with the results of (Aydin and Fenner, 2001).

The interaction energy calculated for a rough surface and bacteria using XDLVO theory and surface element integration is used to calculate the rate constant using the equation

$$K_d = \frac{D}{\int_0^\delta [\alpha e^{\phi/kT} - 1] dy} \quad (4.44)$$

The rate constant is used as a boundary condition in diffusion-convection migration equation described in section 4.2.3.1. The rate of bacteria deposition on the surface is given by Equation (4.44) and we can then convert the deposition rate to total bacterial mass for the time period of 30 min identical to the experimental measurements. As the density and geometry of such bacteria are well defined, the deposited mass per unit length can then be converted to the surface coverage to enable the direct comparison to the experimental measurement. These simulated results are depicted in Figure 4:11.

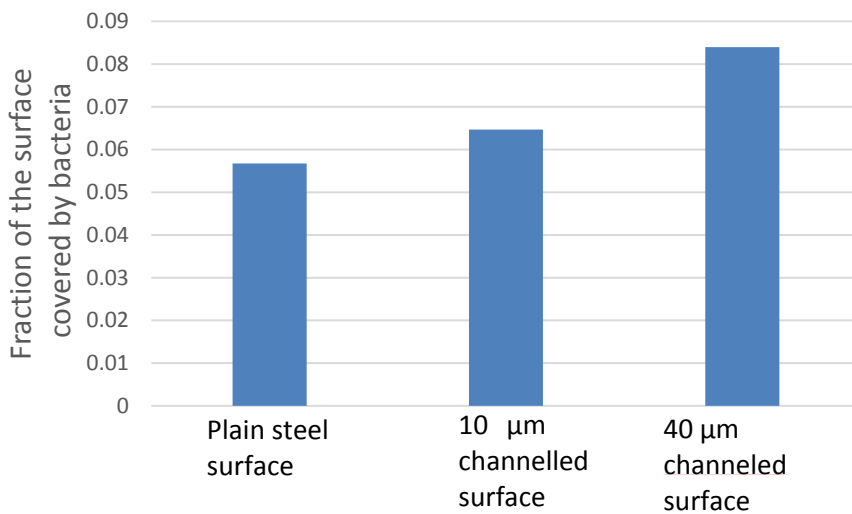


Figure 4:11 Surface coverage on different samples from the diffusion equation by using interaction energy values for different rough surfaces.

The difference in the surface coverage of the attached bacteria should be mainly attributed to the changes in the topography and roughness of the surfaces. The surface roughness of the channels increases with increase in depth due to the chemical etching. As a result, the samples with higher channel depth have higher surface roughness. The results show that an increase in roughness reduces the interaction energy barrier of the bacteria, resulting in increased attachment. It has been also observed that

the experiments with saliva-coated surfaces do not have major differences with the uncoated surfaces. This can be attributed to the fact that the surface roughness in the current samples are high enough and the features cannot be masked by the thin coating of the saliva as observed in nanoscale roughness. To investigate how the topographies induce recirculation and the effect of convection in the deposition of the bacterial cells, different flows as discussed in chapter 3 have been applied.

4.3.2.2 *Bacterial deposition under fluid flow*

The diffusion-convection equation is solved as mentioned in the methods section. The parameters for the simulations were same as for the static conditions, except fluid flow for the channel geometries were computed. The steady state flow field is used to solve the diffusion-convection equation.

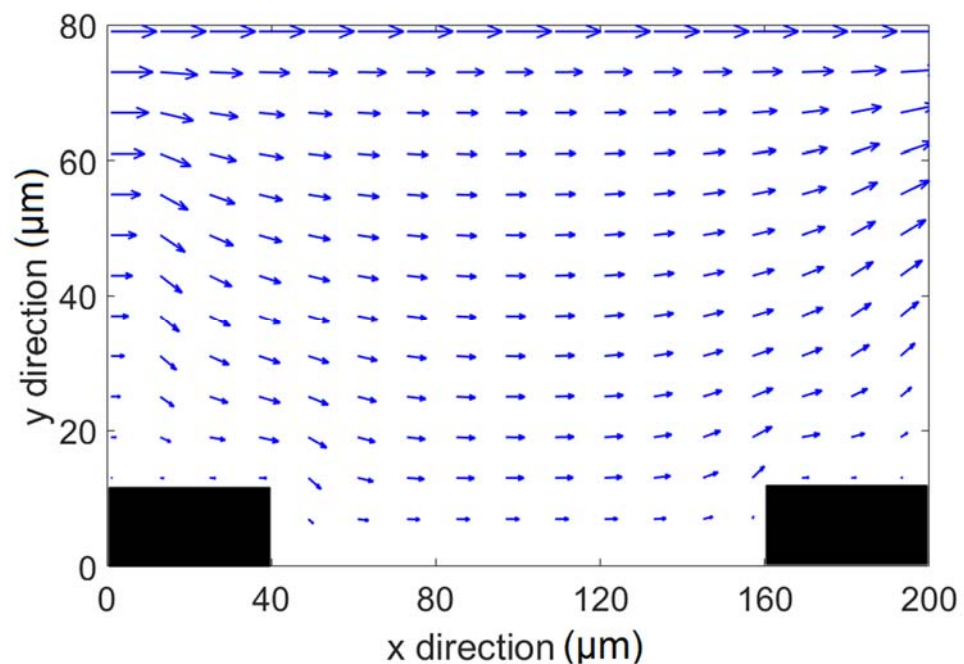


Figure 4:12 Flow profile across a 10 μm depth channel used for the computational model. The profiles used in the computational model are perfect rectangles whereas in the actual steel samples the surfaces were curved inside the channels.

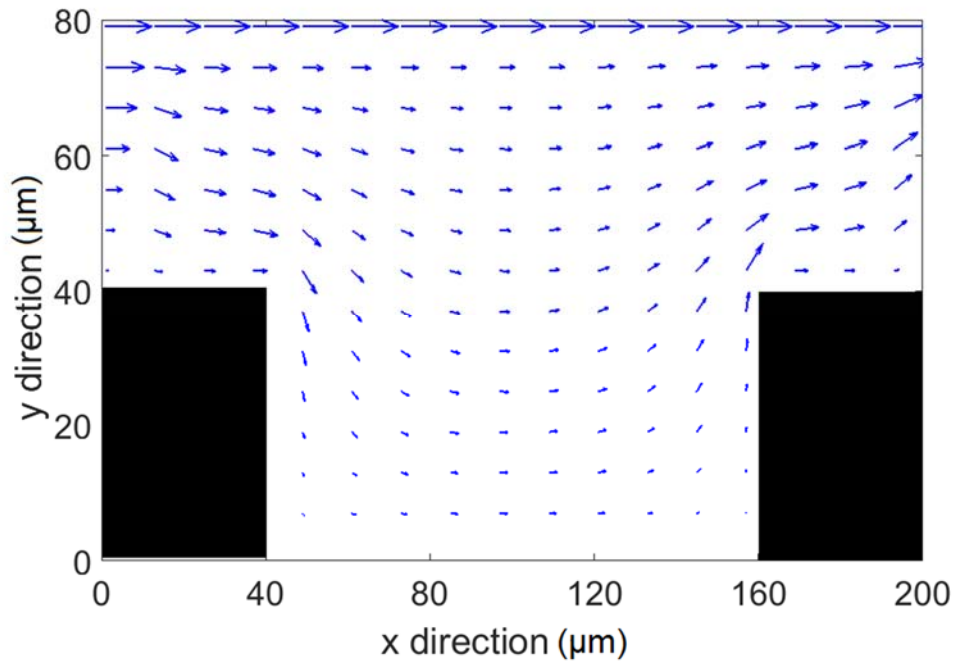


Figure 4:13 Flow velocity over a 40 μm depth channel showing the channel profile used in the computation. It can be observed, that due to the depth of the channel, the bacterial transport due to convection to the bottom of the 40 μm channel is reduced

The above figures Figure 4:12 and Figure 4:13 shows the velocity profile across the two-channel surfaces. The convection of the bacterial cells under flow can be influenced by the height of the topographies. The flow velocity at the bottom of the 40 μm channel is relatively lower than the 10 μm depth channel. The flow velocity calculated as seen above is used to solve the diffusion-convection equation with the XDLVO interactions in the bottom boundary layer. The results are provided in Figure 4:14. The simulation results for multiple simulations had only slight deviations hence, the error bars are not shown in the figures.

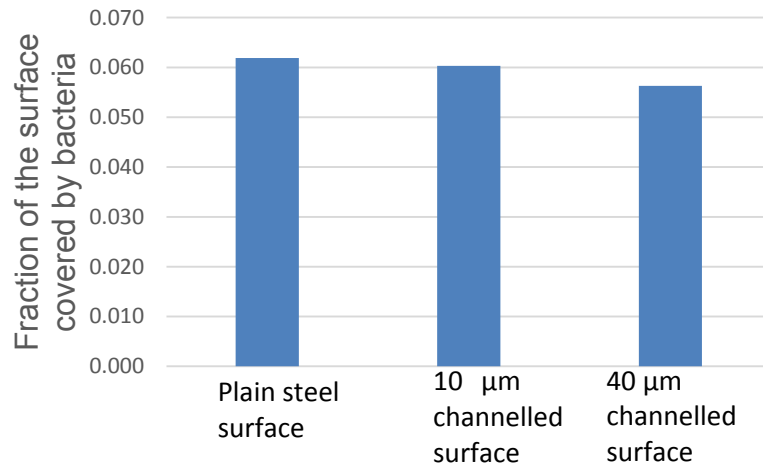


Figure 4:14: Surface coverage calculation of deposited bacterial cells using diffusion-convection equation, with an inlet velocity of 0.125 cm/s.

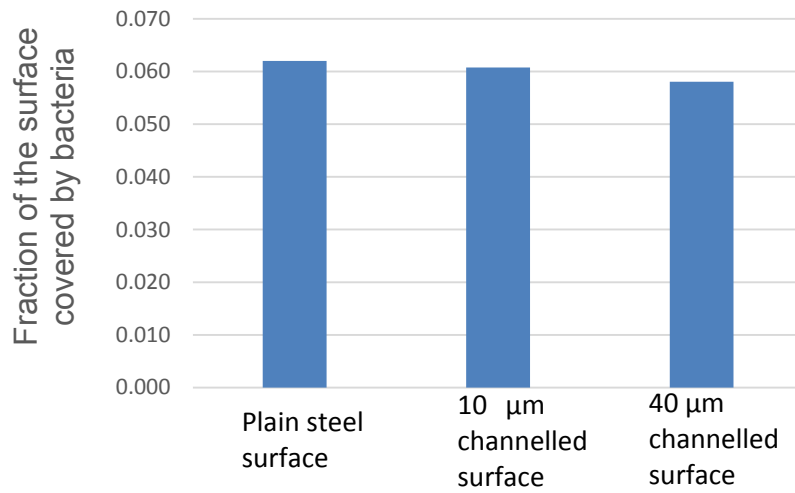


Figure 4:15 Surface coverage calculation of deposited bacterial cells using diffusion-convection equation, with an inlet velocity of 0.253 cm/s.

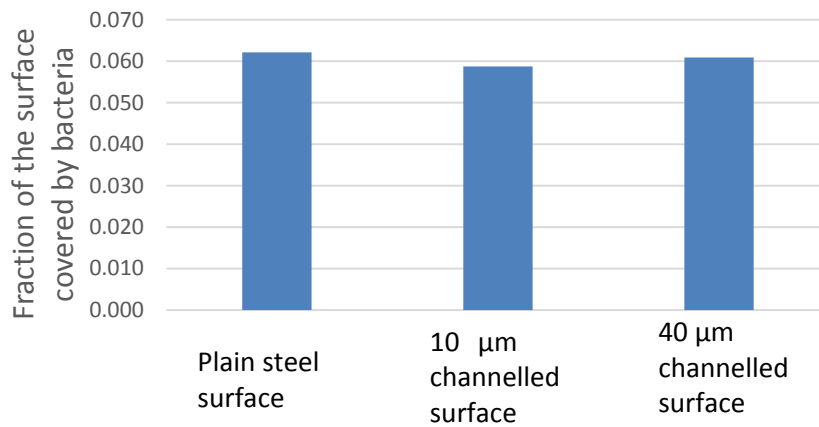


Figure 4:16 Surface coverage calculation of deposited bacterial cells using diffusion-convection equation, with an inlet velocity of 0.8 cm/s.

The deposition for two lower velocities are similar and to the experimental observations made in chapter 3. The computational model predicts higher surface coverage for the 40μm channels compared to the experimental results as shown in section 3.3.6. On observing the deposition rates calculated for the geometry of 40 μm channels, the channel walls are considered to be vertical in the model, as shown in the flow profiles Figure 4:12 and Figure 4:13, but the actual channels have curved edges and the bottom in 'U' shaped and not flat. The deposition rates at the bottom of the channel were still lower than the other two geometries, the rates at the top of the channel near the corners were high and it is because of this region the overall surface coverage of the geometry is high. The higher deposition rate is due to the high flow velocity and can, therefore, higher flux in the corners. As seen from experimental images, the corners attract more bacterial cells than the bottom of the channels. But at a higher velocity not all the cells in this high flux region can attach to the surface due to the presence of high stress due to the velocity field. This might be one of the possible reasons for the difference between the experiment and computational model at high velocity. The slight increase in deposition as observed for 0.8 cm/s can be attributed to the convection of mass is more as the velocity magnitude is affected by the depth of the channel and at the high velocity the magnitude inside the channel should be higher than the two other cases of 0.125 cm/s and 0.253 cm/s. In a study by (Wang *et al.*, 2013) it has been observed that the increase in shear increases attachment until a critical shear, where forces due to XDLVO interactions

are higher the shear force, after which the attachment was observed to have reduced.

The computational model agreed well with the bacterial attachment experiments on static conditions. This is similar to a study by (Mei *et al.*, 2011) where the bacterial attachment increases with increasing roughness under static conditions. The difference in the surface coverage between the experiments and computational model can be attributed to the surface appendages. It has been recently shown by (Back *et al.*, 2017) the fibrillary adhesion of *S. gordonii* employs a catch clamp mechanism to adhere to host surfaces. Another study by (Wilson *et al.*, 2005) shows the influence of proteins in material-cell interactions. The liquid medium, in which the bacterial cells are suspended can contain proteins, which mostly gets adsorbed to the material surface prior to the attachment of bacteria. In such a case the material properties are masked and the bacterial cells adhered to these masking proteins.

4.3.3 **Modelling bacterial attachment on nanostructured titanium surfaces.**

Further, to the modelling work carried on steel surfaces, bacterial attachment on nanostructured titanium surfaces was carried out using the C++ code. Titanium surfaces have been widely used in surgical implants and biomedical devices similar to the steel surfaces, due to their good mechanical properties, corrosion resistance, and bio-compatibility. Three different titanium surfaces were considered for this study, and the SEM images of the surfaces are shown in Figure 4:17 (Cao *et al.*, 2018).

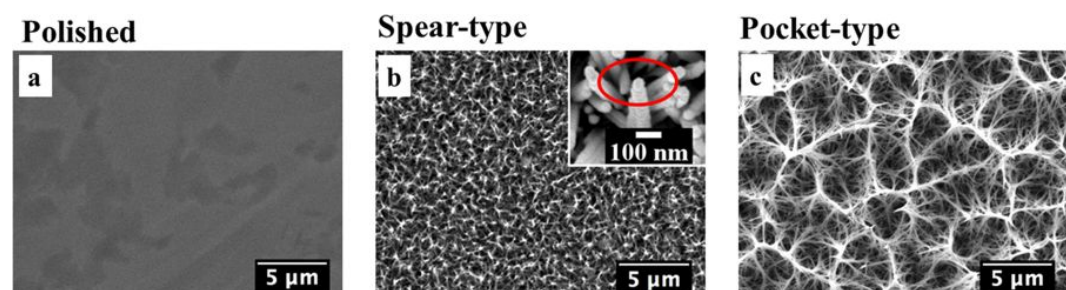


Figure 4:17 SEM images of three titanium surfaces a) Polished titanium surface b) Spear-type surface with dense equally spaced short and thin nanostructure spears. C) The pocket-type surface formed by the intertwining of longer and wider Nano-spears (Cao *et al.*, 2018).

The structures are characterized using an AFM and parameters such as average roughness, RMS, Surface area and size of the spears were obtained as mentioned in (Cao *et al.*, 2018). The following table shows the different parameters.

Surfaces	Ra (nm)	RMS (nm)	Surface area (μm^2)	Spear Size (nm)	Overview
Polished	13.2 \pm 2.3	32 \pm 4.2	100.8	N/A	Flat surface with no nanostructure
Spear-type	195.0 \pm 6.5	245 \pm 7.6	200.5	70	Short and thin Nano-structures similar to a spear shape
Pocket-type	479 \pm 15.3	619 \pm 12.5	1425.8	100	Porous surface with pore diameters ranging from 3 to 5 μm

Table 4-3 Roughness parameters of the different titanium samples obtained using AFM across a projected surface area of 100 μm^2 (Cao *et al.*, 2018).

On further observation, the Pocket-type samples had a normal distribution of the clusters whereas the Spear-type samples were evenly distributed. The computational code has been modified to fit this difference during the surface recreation phase from the roughness parameters. The asperities were normally distributed for Pocket-type surfaces and for the spear-type samples the asperities were uniformly distributed. The zeta potentials for the titanium and given bacteria were -30 mV and -8 mv respectively. The ionic strength was set at 10 mM and contact angle measurements were used for van der Waals potential calculations. The XDLVO simulations of the different surfaces are shown below.

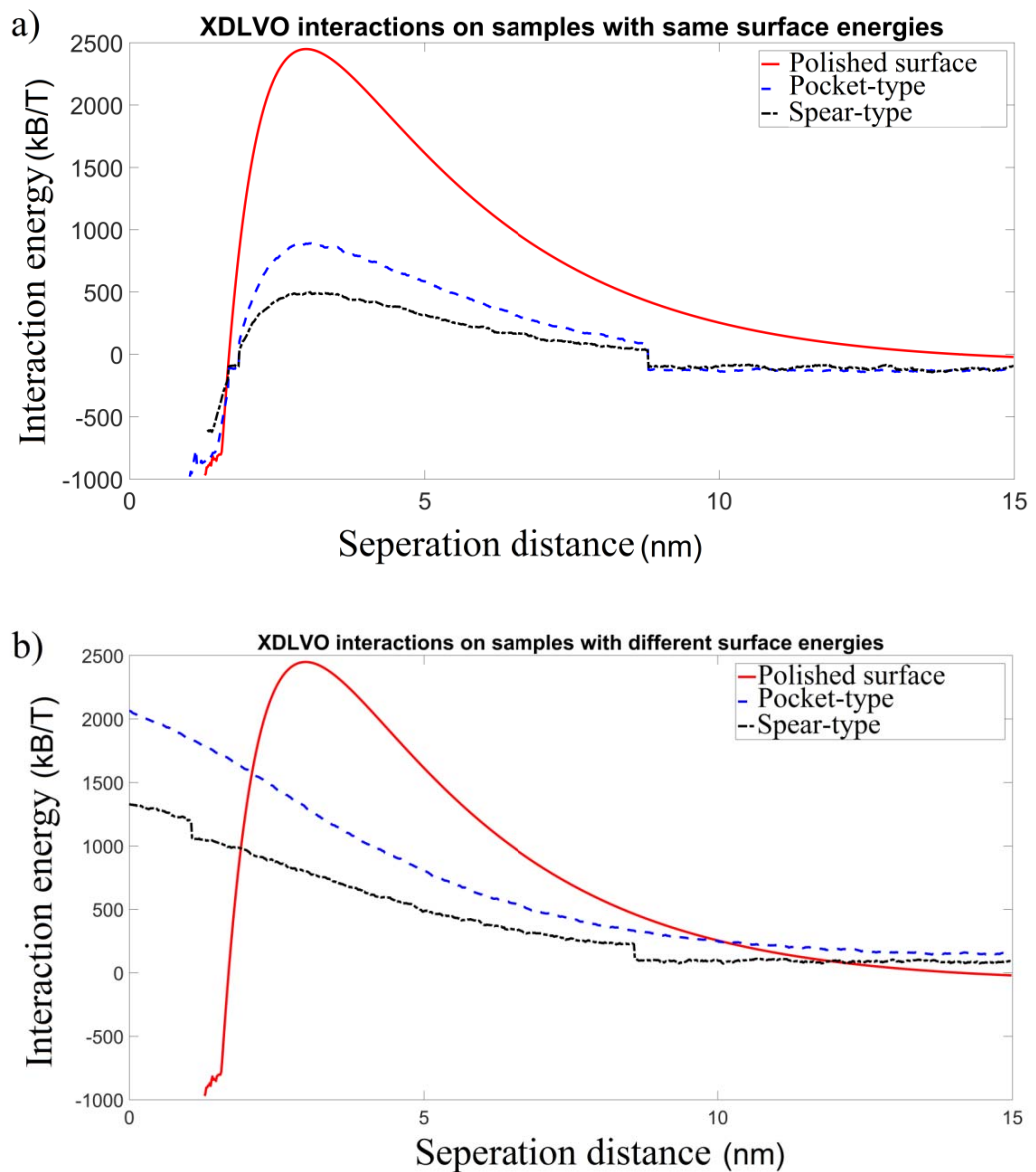


Figure 4:18 Interaction energy for titanium surfaces. a) Interaction energy curves for three different titanium surfaces using respective surface roughness parameters but with same surface energy parameters as obtained from the polished surface. b) Interaction energy curves for three surfaces using different surface roughness parameters and different surface energy parameters as measured on the respective titanium surfaces.

From the figures, it can be observed that the spear type surfaces have the lowest energy barrier to overcome (< 500) and the plain surfaces have the highest energy barrier i.e. more energy is required for the bacteria to reach the surface. But as observed by (Cao *et al.*, 2018) the spear type has the lowest attachment of biofilm on contrary to the computational model. The experiments mentioned in the study are carried out for biofilm growth and the computational model can only predict the initial attachment of bacterial

cells. Another factor influencing attachment not accounted in the model is the adsorption of proteins from the liquid medium to the surface (Wilson *et al.*, 2005).

4.4 Conclusions

A computational model has been developed to study the combined effects of flow, surface chemistry and surface roughness in the attachment of bacteria. In addition to the surface roughness, surface topography has also been employed to study the effect of bacterial attachment on steel surfaces. The computational model was validated using the biofilm experiments with the same properties, and the surface coverage of both the experimental and computational methods are qualitatively comparable. The computational model can be employed to determine the bacterial deposition on different material surfaces. The computational model can be employed to determine surface mechanical properties like topography, surface finishing for anti-bacterial surfaces from the known parameters such as fluid medium, bacteria, and material chemistry. By the use of this model, favorable parameters for anti-bacterial properties can be determined which will help in the development of anti-bacterial engineered surfaces.

5 Biofilm Deformation underflow

5.1 Introduction

Biofilm deformation and detachment due to maturation or fluid stress is the last stage of the biofilm cycle. The interaction between shear stress due to fluid flow and biofilm is a dynamic deformation, which can be related to structural and material characteristics of the biofilm. Mechanical removal of biofilms are employed in the oral cavity (Kolenbrander *et al.*, 2002), medical devices (Alfa and Howie, 2009) and industrial setups (Al Ashhab *et al.*, 2017). To study biofilm deformation under controlled fluid flow, it is good to use microfluidic channels sitting on top of an inverted optical microscope (Kim *et al.*, 2012). The small size of the chambers and transparency allows the real-time study of biofilm deformation subjected to various hydrodynamic conditions. With the advanced techniques of image analysis, it enables the determination of viscoelastic properties of biofilms at small scale. The channels are fabricated by means of soft lithography.

5.2 Experimental methods

5.2.1 Lithography

The microfluidic channels are fabricated by soft lithography. It is the method of replicating PDMS channels using silicon moulds fabricated using photolithography. The moulds are fabricated from silicon wafers. The silicon wafers are treated with a negative, epoxy based photoresist SU-8 3025. The wafer is cleaned, placed on the spinner and the photoresist is applied at the centre of the wafer (1 ml/ 1 inch of wafer diameter) and the substrate is baked at 95°C after spinning. The developed mask with the channels features is placed on the substrate. The next step is the exposure to UV light (350-400 nm) to cure the photoresist. As SU-8 is a negative photoresist, the portion exposed to the light becomes insoluble to the photoresist developer. A developer is used to remove the unexposed portion of the surface. Chemical etching is used to remove the areas not covered by the treated photoresist. This results in forming the structures on the wafer. A chemical resist stripper is used to remove the cured photoresist. The silicon wafer now consists of protruding parts which form the different channels. The silicon wafer can be used multiple times to replicate the channels formed using photolithography.

The process of fabricating microfluidic channels from silicon wafers is known as soft lithography. The PDMS (SYLGARD184) is prepared by mixing the elastomer base and the curing agent (cross linker) at a ratio of 10:1. The mixture is placed in a vacuum chamber for degassing. The vacuum pump is run for up to 5 min and the chamber is vented. The process is repeated until the mixture is free of any air bubbles. The silicon wafer is placed on a hot plate at 65⁰C. The PDMS is poured over the wafer avoiding any bubbles. The temperature is maintained for a period of 60 min to cure the PDMS. After curing the PDMS is stripped from the mould and individual channels are cut using a scalpel. A biopsy punch is held perpendicular to the surface of the channels to punch access holes to the channels. The channels and microscopic slides are cleaned to remove any dust on the surfaces. The channels and slides are placed in plasma cleaner. The plasma reacts to the glass and PDMS and SI-OH bonds are formed on the surfaces as a result. When the PDMS channels are placed on the glass slides the SI-CH₃ bonds recombine to form SI-O-SI bonds thus sealing the channels with the glass slides. The microfluidic channels prepared by soft lithography can be used to grow biofilms and carry out micro PIV analysis, for velocity calculations. The methods of Particle imaging is given below.

5.2.2 ***Particle velocimetry***

One of the successful techniques for quantifying flow around a biofilm in microenvironment is particle Velocimetry. Particle Velocimetry can be divided into Particle Tracking Velocimetry and Particle Image Velocimetry. The common principle for both the methods is tracking particles suspended in the fluid flow. The particles are selected so that it doesn't cause any flow disruptions and it is assumed the particles follow the flow of fluid. Continuous imaging is carried out with the help of high-speed cameras. The particle displacement in successive image frames over the time between the image-pairs, from which the velocity of the fluid is obtained. Particle Tracking Velocimetry works by following the path of individual particles and calculating the velocity. By this technique, the computation becomes very expensive as the number of particles increase. On the other hand, PIV works by cross-correlating small sections of

images called interrogation areas, with the next image. A normal setup of a PIV system is shown in Figure 5:1.

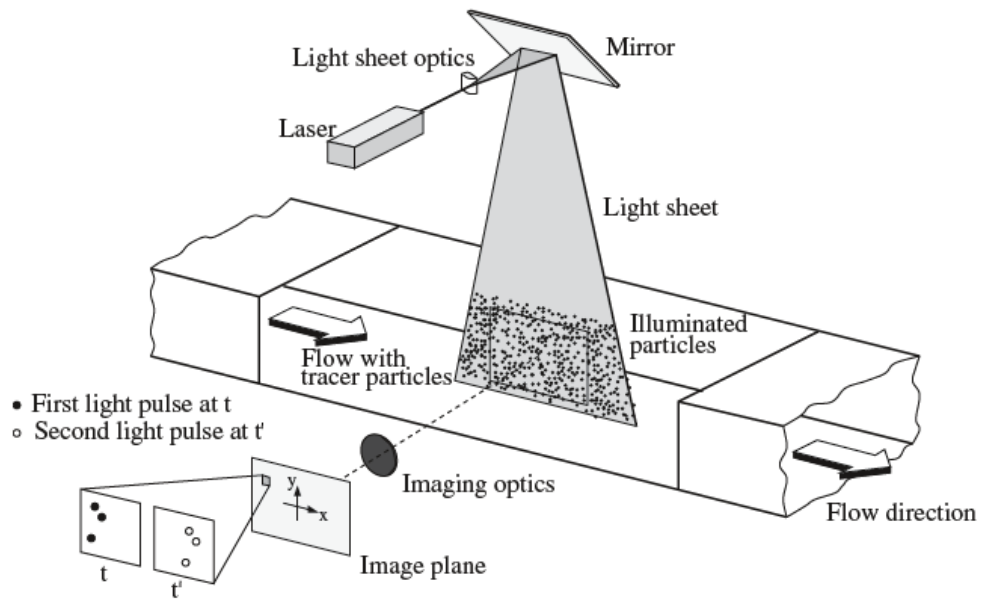


Figure 5:1 A schematic of the laser illuminated PIV system. The laser is pulsed at a high speed and illuminates the particles suspended in the flow. By this method, the particle streaking effect, which is common in traditional micro PIV can be avoided (Raffel *et al.*, 2018).

5.2.2.1 *Micro PIV*

Traditional PIV systems are used in wind tunnels and flow chambers (Raffel *et al.*, 2018). In applications like biofilm development, it is important to determine flow field at the micron level. A typical micro PIV system consists of a microfluidic device, a microscope, a laser, and a camera. The setup of a micro PIV system is shown in Figure 5:2.

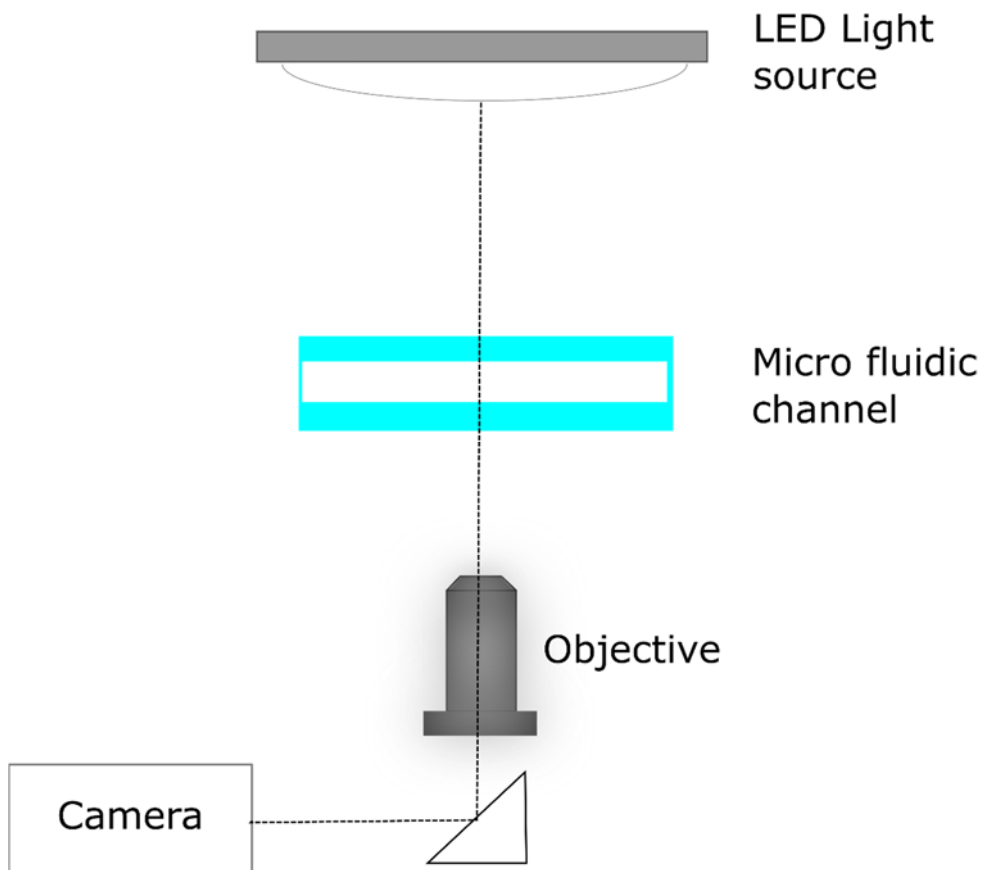


Figure 5:2 Schematic representation of a micro PIV system. Instead of a laser illumination light source such as LED is used. The microfluidic chamber is usually driven by a syringe pump. The light passing through the microfluidic chamber is captured using a high-speed camera.

5.2.2.2 *Direct cross-correlation*

In the digital PIV, the digital images acquired are pixilated and hence it is discretized. The intensity value of each pixel is usually represented by 8 bits (0-255). The discretized cross-covariance can be expressed in a discrete domain as

$$C(r, s) = \frac{1}{M * N} \sum_{m=1}^M \sum_{n=1}^N [f(m, n) - \bar{f}] [f(m + r, n + s) - \bar{g}] \quad (5.1)$$

Where, $f(m, n)$ and $g(m, n)$ is the consecutive sample images M, N are the number of rows and columns in the images and C is the correlation function. (r, s) represents the position for calculation and \bar{f}, \bar{g} are the mean intensity of the interrogation windows f, g . As the images are discretized, the cross correlation of the domain will result in integer values. The peak value as shown below after cross correlation for the image gives the particle shift in pixels with an error of ± 0.5 pixel.

5.2.2.3 Fast Fourier Transform

The direct cross-correlation method is computationally expensive when applied to large image data sets. An alternate method for computing the cross-correlation is by Fast Fourier transforms (FFT) (Dabiri, 2006). It is carried out by means of correlation theorem as the cross-correlation of two functions is equivalent to multiplication of complex conjugates of their Fourier transforms. The correlation theorem derived using Fourier theory is shown below. Let k , be the wave number which is expressed as a function of λ , the wavelength as

$$k = 1/\lambda \quad (5.2)$$

The Fourier transform F and inverse Fourier transform f can be expressed as

$$F(k) = \int_{-\infty}^{+\infty} f(x)e^{2\pi ikx} dx \quad (5.3)$$

$$f(x) = \int_{-\infty}^{+\infty} F(k)e^{-2\pi ikx} dk \quad (5.4)$$

The correlation between two functions $f(x)$ and $g(x + \Delta x)$ can be derived as,

$$\begin{aligned} C_{fg}(\Delta x) &= \int_{-\infty}^{+\infty} f(x)g(x + \Delta x) dx \\ &= \int_{-\infty}^{+\infty} \left(\int_{-\infty}^{+\infty} F(k)e^{-2\pi ikx} dk \int_{-\infty}^{+\infty} G(k')e^{-2\pi ik'(x+\Delta x)} dk' \right) dx \\ &= \int_{-\infty}^{+\infty} \int_{-\infty}^{+\infty} F(k)G(k')e^{-2\pi ik'\Delta x} \left(\int_{-\infty}^{+\infty} e^{-2\pi i(k'-k)x} dx \right) dkdk' \\ &= \int_{-\infty}^{+\infty} \int_{-\infty}^{+\infty} F(k)G(k')e^{-2\pi ik'\Delta x} \delta(k' - k) dkdk' \\ &= \int_{-\infty}^{+\infty} F(k)G(k)e^{-2\pi ik\Delta x} dk \end{aligned}$$

$$= f^{-1}[F(k)G(k)] \quad (5.5)$$

This theorem is shown for one dimension and can be applied in a similar fashion to two or more dimensional problems.

The implementation of FFT reduces the computation from $O[N^2]$ to $O[N \log_2 N]$ operations. The interrogation areas of two images are converted to two-dimensional FFT's and complex conjugate multiplication is carried out on these resulting FFTs. The result is inverse Fourier transformed to produce cross-correlation in spatial dimensions.

The input to the FFT correlation is assumed to be periodic, hence the output, correlation data is periodic. If the displacement is greater than half the sample size N , the measured displacement is the difference between the actual displacement and the sample size (Raffel *et al.*, 2018). In these cases, the interrogation window size should be increased or the timing between the images should be reduced to avoid aliasing of the output as this will violate the Nyquist sampling criterion. Therefore, the maximum displacement obtained using FFT cross-correlation is limited half the sample size. For example, if the interrogation area is 64×64 pixels the maximum displacement that can be obtained is limited to 32 pixels for an image pair. Hence, 50% overlap is considered for the interrogation areas in the analysis. A general rule practiced for FFT correlation in PIV is to keep the maximum displacement of the particles to 25% of the interrogation window, also known as a one-quarter rule. The method of cross-correlation described above is shown in Figure 5:3.

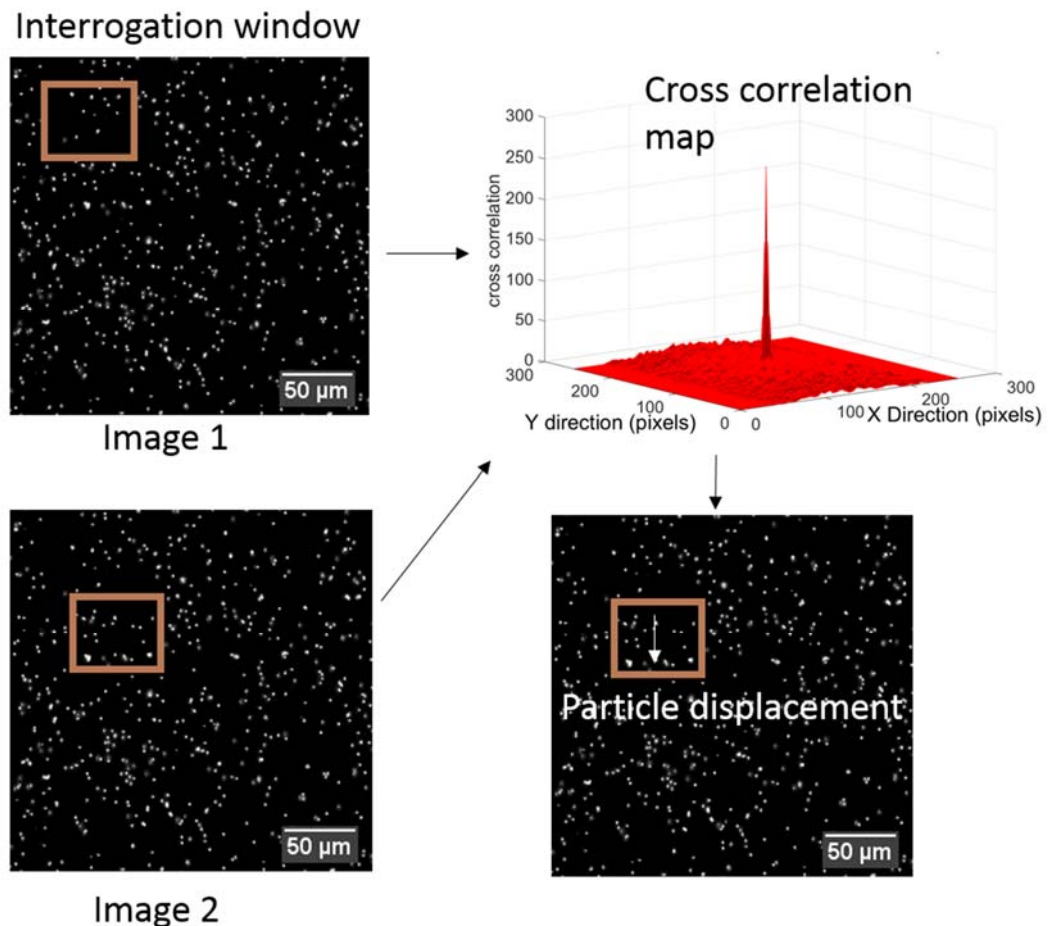


Figure 5:3 Cross-correlation and particle displacement from image pairs with particles of diameter $1\ \mu\text{m}$. The images are cut into smaller images of interrogation areas and are cross-correlated with the next frame. The highest peak in the correlation map is the corresponding movement in length and the time between frames can be used to calculate velocity.

5.2.2.4 *Phase contrast microscopy*

Phase contrast microscopy has been employed for this current study. The light waves passing through the sample i.e., biofilm, liquid medium, and particles have different refractive indices and the phase of the light waves can be reduced by up to one-fourth of the original phase. As the resulting amplitude is not changed the difference between the light rays cannot be observed as in bright field microscopy. Phase contrast microscopy transforms the changes in phase to amplitude differences. The phase contrast microscopy can be divided into two types, dark phase contrast, and bright phase contrast. In dark phase contrast the objects in the light path appear darker than the surrounding and in bright phase contrast, the objects appear brighter than the surrounding. The following Figure 5:4 shows the two types of imaging. Bright phase contrast is used in the

experiments as the particles appear brighter as this is easier to process the images for PIV calculations.

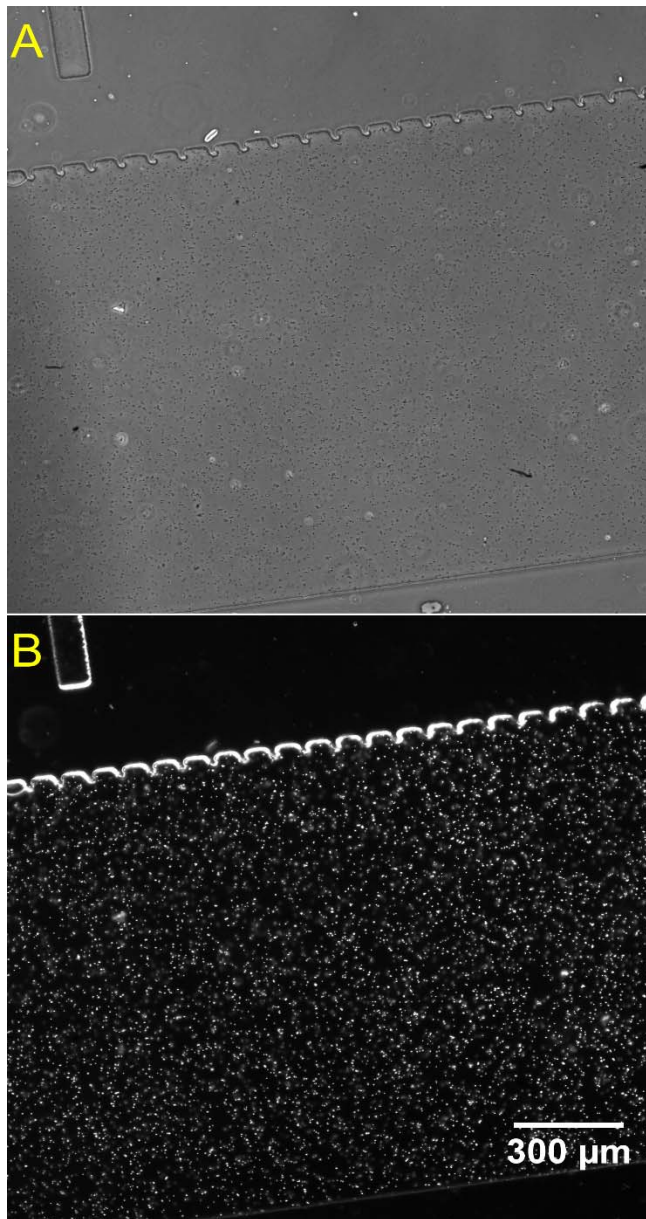


Figure 5:4 a) Dark phase contrast image of $0.5\ \mu\text{m}$ particles underflow b) Bright phase contrast image of $0.5\ \mu\text{m}$ particles underflow.

5.2.2.1 **Signal to noise ratio:**

PIV calculations are prone to noise and it is inherent to PIV data. Sources contributing to the noise include background, optical distortion and light to name a few. In addition to this, calculation errors can arise from particle seeding, image resolution, and interrogation region sizes. The cross-correlation output represents the combined effects due to different errors mentioned above and it is the probability distribution of all image pattern displacements between two images. In order to quantify the errors in PIV

measurement, the cross-correlation data is checked for the signal to noise ratio (SNR). Different measures of SNR are used in PIV measurements such as Primary peak ratio (PPR), peak to root mean square ratio (PRMSR) and peak to correlation energy (PCE). The following figure shows the calculation of PPR using the primary and secondary peaks from the correlation data. The equation for PPR is given below

$$\text{PPR} = \frac{C_m}{C_2} \quad (5.6)$$

The PPR is mostly used in PIV calculations as a measure of SNR. From the above equation, if the primary and secondary peaks have the same correlation output, the value will be 1. Generally, a measure of 1.2 is considered to validate the output as acceptable. For the following figure, a PPR value of 1.51 was obtained (Figure 5:5). For the calculation, two images with background subtraction were considered. To demonstrate the effect of background noise on images, the same calculation as mentioned above was performed on the images with the background. It can be observed from Figure 5:5 that the SNR of the image pair was very low and it resulted in a PPR value of 1.14 (Figure 5:6).

Another measure analyzed for SNR in the current study is peak to root mean square ratio (PRMSR). It is defined as the ratio of the square of the magnitude of the primary peak in the cross-correlation peak to the root mean square. PRMSR is expressed as

$$\text{PRMSR} = \frac{|C_m|^2}{C_{\text{rms}}^2} \quad (5.7)$$

The noise part, C_{rms} is the root mean square of the correlation values below the threshold, which is half the magnitude of the peak correlation value. It can be calculated as,

$$C_{\text{rms}} = \sqrt{\frac{1}{N} \sum_{i=0}^{C_m/2} |C(i)|^2} \quad (5.8)$$

Figure 5:5 and Figure 5:6 shows the thresholds for an image with and without background noise. It can be observed from the figures, the area of

the correlation plane above the threshold is larger in the noisy image compared to the image without background noise, hence lower signal to noise ratio. The cleaned image has a PRMSR value of 24.3 and the noisy image has a value of 14.

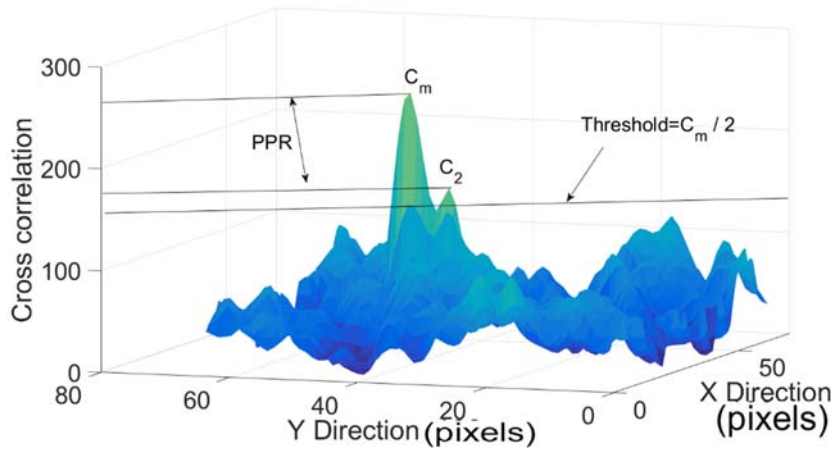


Figure 5:5 2D representation of the cross-correlation output. SNR can be calculated using the primary and secondary peaks of the correlation output. C_m , represents the height of the primary peak and C_2 is the height of the secondary peak. The ratio between the primary and secondary peak is the Primary peak ratio (PPR) used to quantify the correlation uncertainties. For this example, the $PPR = 1.51$.

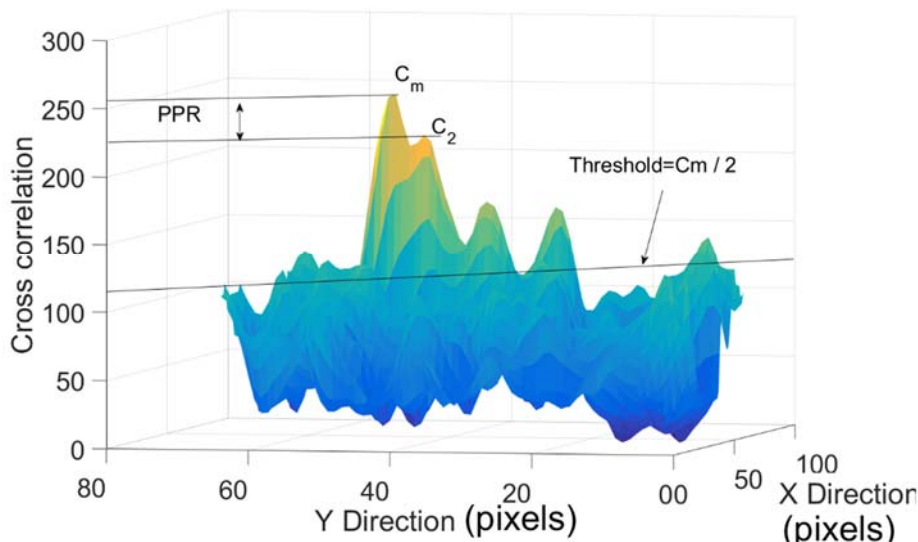


Figure 5:6 2D representation of the cross-correlation output of a pair of images separated by time dt and with background noise. The PPR value is lower than that of noise removed image ($PPR=1.4$). The area above the threshold is also greater in comparison to Figure 5:5, decreasing the PRMSR value.

5.2.3 Velocity profile in microchannels:

The flow velocity calculated by micro PIV should be analyzed with theoretical calculation, for the technique validation. The flow in a microfluidic device can be analytically calculated using Poiseuille flow. A typical flow velocity profile inside a rectangular chamber is shown in the following Figure 5:7.

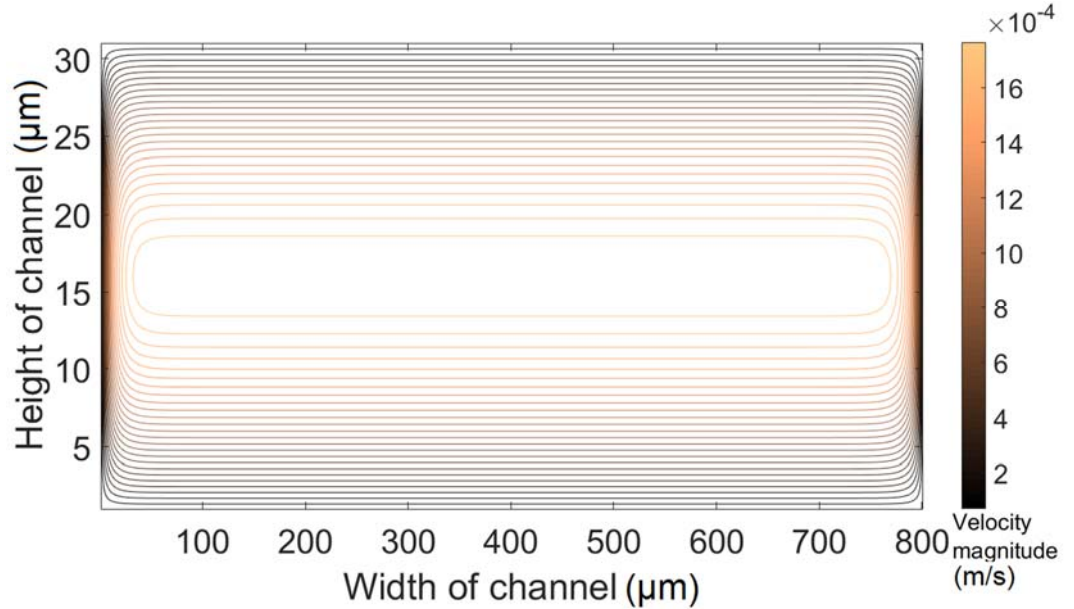


Figure 5:7 Contours corresponding to the velocity field u_x for Poiseuille flow inside a rectangular microfluidic chamber of height 30 μm , width 800 μm .

The velocity field for the Poiseuille flow can be described using the following formula as given by (Bruus, 2008),

$$u_x(y, z) = \frac{4h^2 \Delta p}{\pi^3 \eta L} \sum_{m, \text{odd}} \frac{1}{n^3} \left(1 - \frac{\cosh(n\pi \frac{y}{h})}{\cosh(n\pi \frac{w}{2h})} \right) \sin(n\pi \frac{z}{h}) \quad (5.9)$$

On integrating the above velocity equation, the flow rate Q can be calculated as

$$Q = 2 \int_0^{w/2} dy \int_0^h dz u_x(y, z) \quad (5.10)$$

$$= \frac{4h^2\Delta p}{\pi^3\eta L} \sum_{m,\text{odd}}^{\infty} \frac{1}{n^3} \frac{2h}{n\pi} \left(w - \frac{2h}{n\pi} \tanh\left(n\pi \frac{w}{2h}\right) \right) \quad (5.11)$$

$$= \frac{h^3w\Delta p}{12\eta L} \left(1 - \sum_{m,\text{odd}}^{\infty} \frac{1}{n^5} \frac{192h}{\pi^5w} \tanh\left(n\pi \frac{w}{2h}\right) \right) \quad (5.12)$$

By approximating $h/w = 0$ (considering the channel much wider compared to height), we get

$$Q = \frac{h^3w\Delta p}{12\eta L} \left(1 - \frac{192h}{\pi^5w} \sum_{m,\text{odd}}^{\infty} \frac{1}{n^5} \right) \quad (5.13)$$

$$Q \approx \frac{h^3w\Delta p}{12\eta L} \left(1 - 0.630 \frac{h}{w} \right) \quad (5.14)$$

By using the equations (5.14) and (5.9) the velocity profile across a microfluidic channel of width 800 μm and height of 30 μm can be calculated. From equation (5.14) pressure can be calculated. For a known case of the volumetric flow rate of 50 $\mu\text{l/h}$, the pressure change across the channel is calculated as 1.814 μPa . From this pressure drop, the velocity profile across the height of the channel is calculated using the equation (5.9). The analytically calculated velocity profile is shown in Figure 5:8. The experimental velocity profile, calculated using PIV is also observed to be parabolic, similar to the analytical calculation.

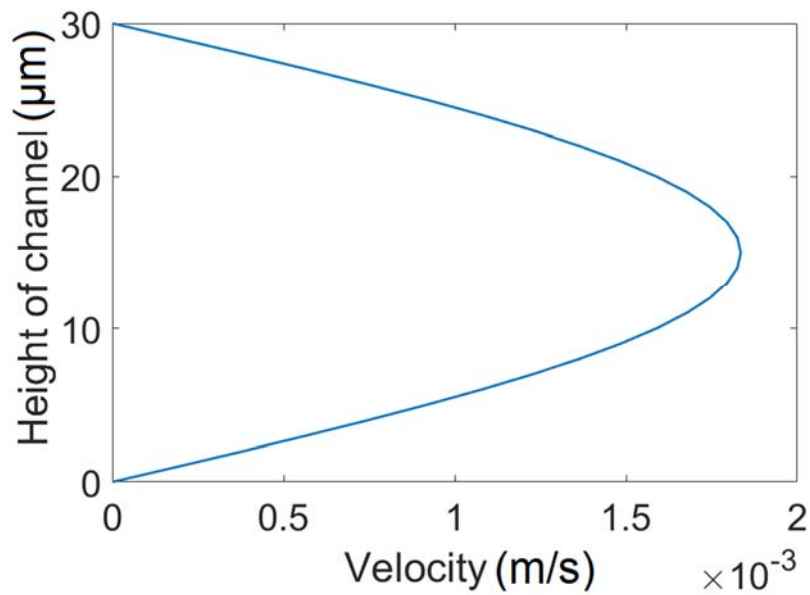


Figure 5:8 Analytical velocity profile for a flow rate of 100 $\mu\text{l/h}$ for the channel of height 30 μm , width 800 μm .

Figure 5:8 shows the parabolic velocity field across the height of the channel. In order to validate the theoretical calculation with the experiment, the velocity across the width of the channel was compared. The velocity across the height of the channel cannot be calculated experimentally since the images are obtained for one height (corresponding to the depth of focus of the lens).

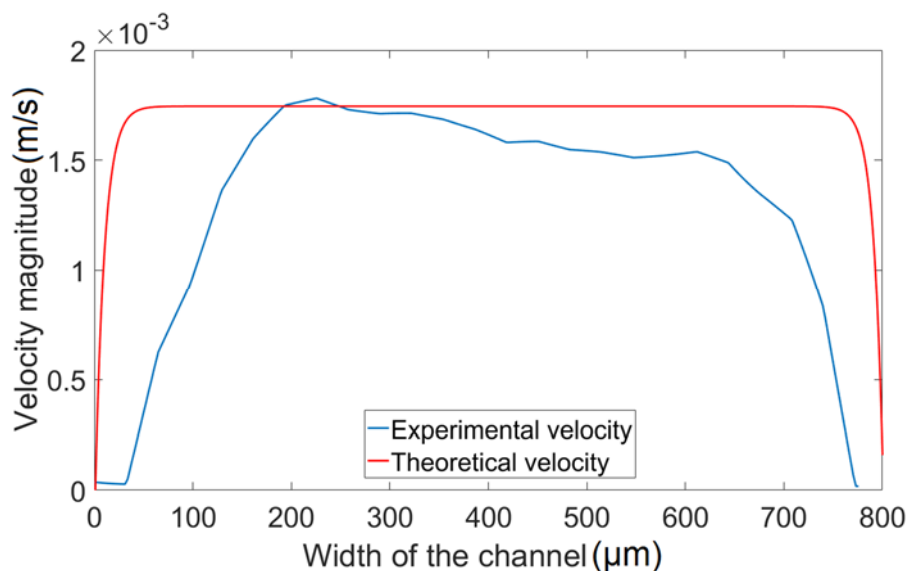


Figure 5:9 Theoretical and experimental velocity magnitude across the width of the channel. The width of the channel was 800 μm and the height was 30 μm . The flow velocity used in the calculations was 100 $\mu\text{l/h}$. The velocity profile corresponding to theoretical velocity is for the middle of the channel (30 μm)

From the Figure 5:9, it can be observed, the PIV calculation quantitatively matches with the theoretical calculation for Poiseuille flow. As with any experiments, there is a slight deviation. This deviation between the two velocities can be attributed to differences in the actual flow using the syringe pump in the experiments and the depth of focus in experiments cannot be obtained accurately. Having validated the velocity calculations, to calculate the stresses in the fluid, pressure across the channel was calculated.

5.2.1 **Pressure Calculation:**

After obtaining the velocity fields from PIV calculations, the pressure is calculated using an open source code MATLAB code known as Queen 2 (Dabiri *et al.*, 2014). The calculation is based on the integration of the pressure term in the Navier-Stokes equation.

$$\nabla p = -\rho \left(\frac{Du}{Dt} - \nu \nabla^2 u \right) \quad (5.15)$$

where,

p , the pressure,

ν , the dynamic viscosity and

$\frac{Du}{Dt}$, the material derivate of velocity.

The solid structure in the study is the viscoelastic biofilm matrix, made of bacterial cells and EPS matrix, which deforms due to the fluid velocity and the biofilm structure in the fluid path influences the fluid velocity in turn.

The material derivative for fluid-structure interactions can be derived from two sequential velocity fields as given by (Dabiri *et al.*, 2014) using the following formula

$$\frac{Du}{Dt}(x_i, t_i) \approx \frac{U_{PIV}(x_i^a, t_2) - U_{PIV}(x_i^a, t_1)}{t_2 - t_1} \quad (5.16)$$

And x_i^a can be expressed as

$$x_i^a = x_i + \left(\frac{U_{PIV}(x_i, t_1) + U_{PIV}(x_i, t_2)}{2} \right) (t_2 - t_1) \quad (5.17)$$

The above equation is similar to the Crank-Nicolson scheme (Dabiri *et al.*, 2014).

From the above equation, the pressure between two points can be calculated by integrating between the two points. The integration of pressure term between two points (x_1 and x_2) can be calculated as

$$p_2 - p_1 = \int_{x_1}^{x_2} \nabla p dx \quad (5.18)$$

The measurement of pressure by the above equation can accumulate errors due to integration. Hence, the algorithm uses multiple independent paths for integration to obtain the value of pressure at a point, as pressure is a scalar quantity and the value is independent of its integration path for the flow velocities used in the study, as shown by (Dabiri *et al.*, 2014). The pressure at each grid point is calculated by eight integration points originating from the boundary and traversing to the grid point. By using the calculated pressure and the velocity obtained from the micro PIV, the stresses in the fluid medium acting on the biofilm surface can be determined.

5.3 Experimental setup

5.3.1 Image Acquisition

Photron Fastcam mini UX has been used to acquire the images. A 10× (Nikon) Phase objective was used to acquire images at a speed of 8000 fps and the individual image size was 288×640 pixels. The pixel size of the sensor is 10 μm×10 μm, at a magnification of 10× each pixel size corresponds to 1 μm in the images. The particles used for the experiments are 1 μm and image size of each particle is 1 μm. The captured images are imported to the computer in TIFF image format for further processing.

5.3.2 Recording techniques:

The recording techniques for the PIV can be broadly classified into two categories namely, single frame/ multi-exposure PIV and multi-frame/

single exposure PIV. In the first method, a single frame contains particle images at different time steps. The directional component of the resolved velocity cannot be resolved by this method without using additional methods such as displacement biasing or colour coding. This problem can be overcome by the use of high frame rate digital cameras by using multi-frame/ single exposure PIV. In this method, each particle image at different time steps is stored in different frames. The following figure illustrates the difference between the two methods.

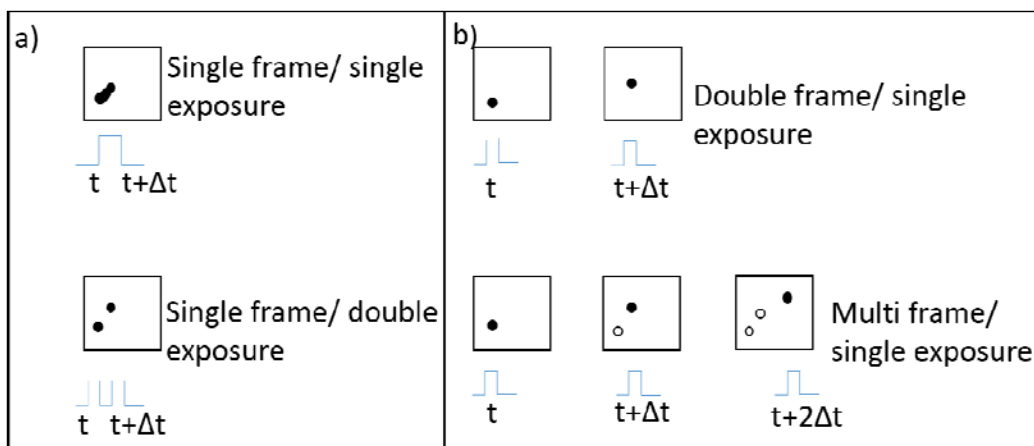


Figure 5:10 a) Illustration of single frame multiple exposure methods. The images of particles are recorded in the same frame by this method. b) Illustration of multiple frame single exposure methods. Each frame contains only one image of the moving particle. The dark circles represent an image captured in the current frame and hollow circles represent the image captured in the previous frames.

5.3.3 Syringe pump operation

The syringe pump is programmed to ramp up to different flow rates (5000, 10000, 25000, 50000 $\mu\text{l/h}$) and to ramp down to zero as shown in Figure 5:11. This is carried out to capture the compression and relaxation of the biofilm during the flow. The total time for ramping up and down is maintained as 12 s as the camera capacity at 8000 fps is 14 s.

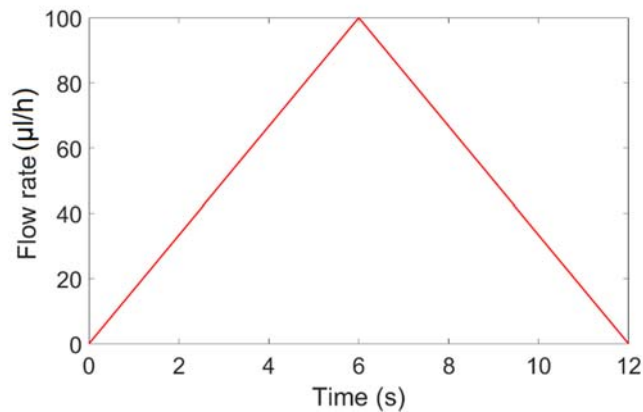


Figure 5:11 A Sample flow rate ramp used in the experiments. The flow rate is ramped to the maximum in a time span of 6 s and then ramped down to zero in the next 6 s.

5.3.4 **Bacteria culture**

The experiments for biofilm deformation is carried out in the microfluidic chambers fabricated as mentioned above. *Bacillus subtilis* stock is thawed and 10 µl is added to 20 ml Tris (Tris (hydroxymethyl) aminomethane) and placed in a shaker overnight to prepare the liquid culture.

5.3.5 **Microfluidics setup**

The cultures are injected into the channels using a syringe pump at 35 µl/h. The flow rate is maintained for 2 h to allow bacterial cells to attach to the walls of the chambers. The culture solution is removed and culture broth is injected into the system. Bubbles are avoided carefully during the above process. The flow is maintained at 35 µl/h for 36-48 h to allow biofilm formation. Once the biofilm is formed, the pump is run at higher flow rate (500 µl/h) to remove any loosely attached clumps of biofilm from the channel. In order to observe and calculate flow velocity, 1 µm polystyrene beads are added to the culture broth. Biofilm experiments are carried out by ramping the flow rate (Figure 5:11) and observing the biofilm deformation. One of the initial steps is calculating the velocity field by Particle Image Velocimetry (PIV).

5.3.6 **Image Pre-processing**

Image pre-processing is carried out to remove the background noise in the image so that the particles in the flow are clearly visible for further processing. Pre-processing is done using MATLAB R2016. In the first step the interface, biofilm (solid region) and fluid flow (liquid region) are

separated and written as two separate image files. This step is carried out to reduce processing times in later stages and to obtain the interface so that the deformation rate can be calculated. The following figure shows the original image and the separated images.

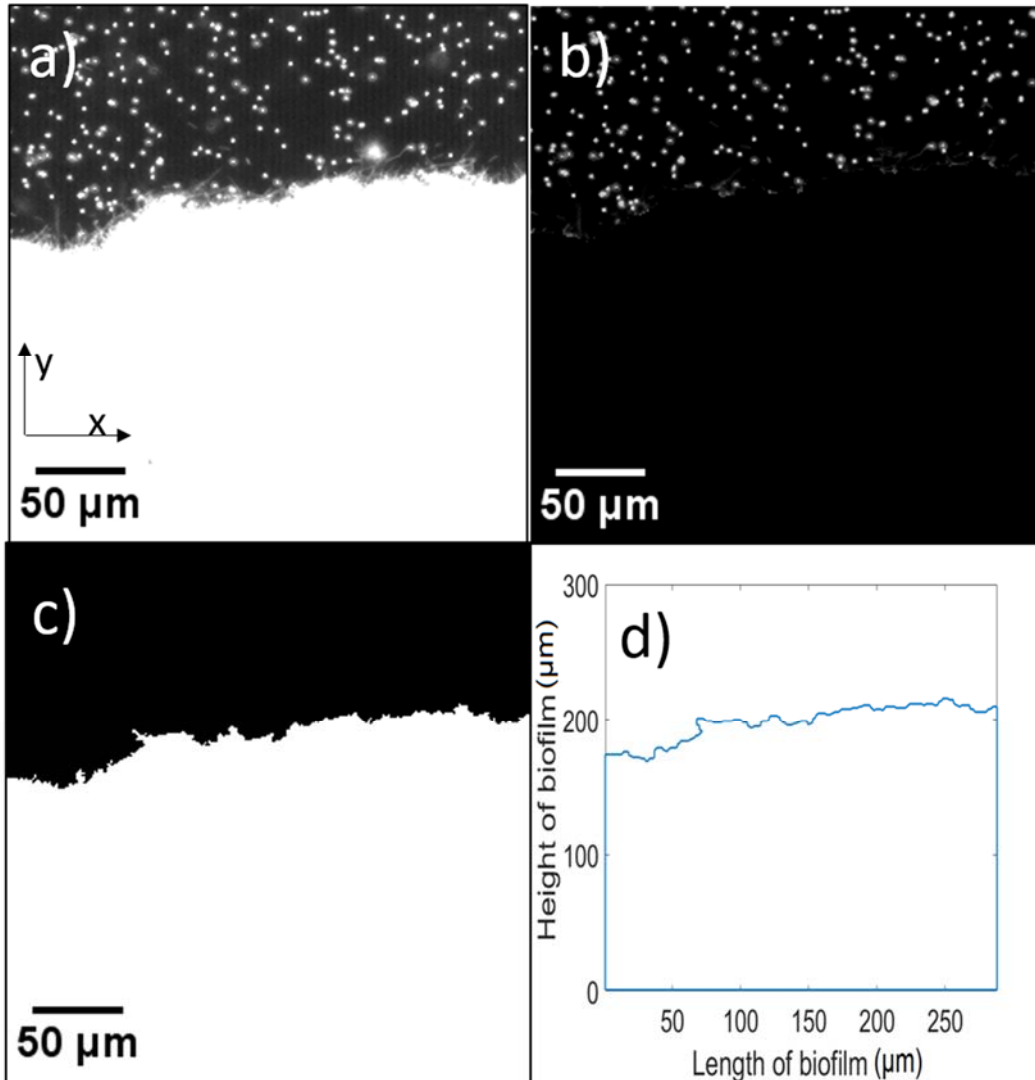


Figure 5:12 Image Pre-processing a) Original image showing biofilm underflow. b) Image showing only the particles suspended in the fluid c) Image showing the solid regions of the image d) Biofilm interface derived from the image.

The background from the images with the particles is removed by taking an average of the 5000 images from the total images. The average is then subtracted from the images to remove the background. The following figure shows the subtracted image.

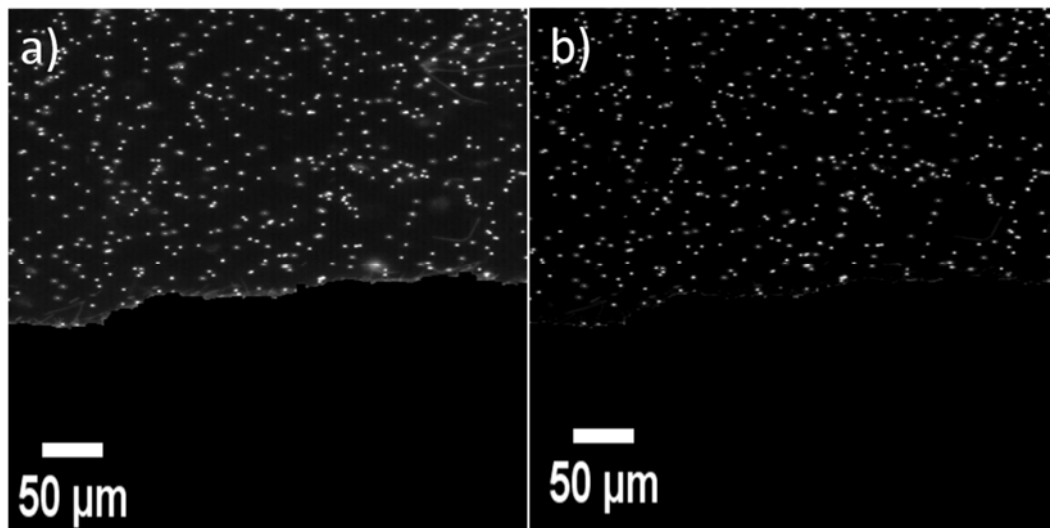


Figure 5:13 Background removal from images a) Image with the background noise b) Image after subtracting the background noise.

5.3.7 Processing

An FFT cross-correlation PIV technique as mentioned in the methods was carried out on the pre-processed images. A square interrogation window with multi-pass algorithm was used to resolve the flow field. An interrogation window with 64×64 pixels with 50% overlap was used for the first pass to resolve the flow field. The second pass was carried out using a 32×32 interrogation window with 50% overlap. The following figures show the velocity field obtained using PIV and the ramp in fluid flow.

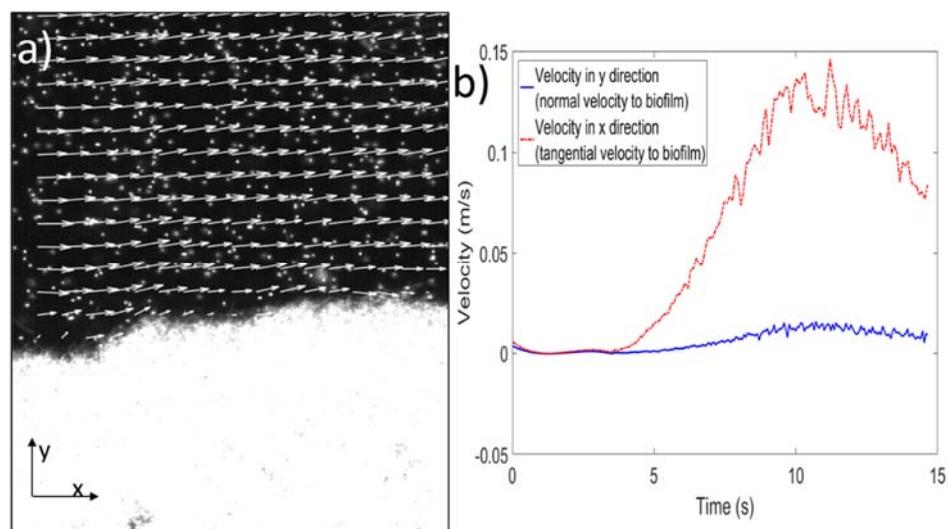


Figure 5:14 PIV processing a) PIV velocity field obtained using a multi-pass algorithm using 64 (pass 1) and 32 (pass 2) interrogation windows and FFT cross-correlation. The velocities are calculated by taking median from a 5×5 window near the biofilm surface. b) The normal and tangential velocity near the surface of the biofilm at different times.

The biofilms were grown in microfluidic chambers as mentioned above. Different flow rates were used and the deformation of the biofilm was observed using high-speed imaging. The required flow rates are provided using a syringe pump.

5.4 Results and discussion

In the current study three cases of 1000 $\mu\text{l/h}$, 5000 $\mu\text{l/h}$ and 25000 $\mu\text{l/h}$ flow rates are used to study the deformation of the biofilm. To calculate the stress acting on the biofilm surface, the pressure was calculated according to the above-mentioned method. The velocity profiles tangential to the biofilm surface is shown in Figure 5:15 below. Although the velocity profile used is a ramp, the final velocities inside the flow channels have not returned to zero. It is due to the limitation in the imaging capacity, as the high-speed camera can store only limited images. The capture time of the camera cannot be increased under such high-speed imaging, hence images cannot be acquired until the flow returns to zero.

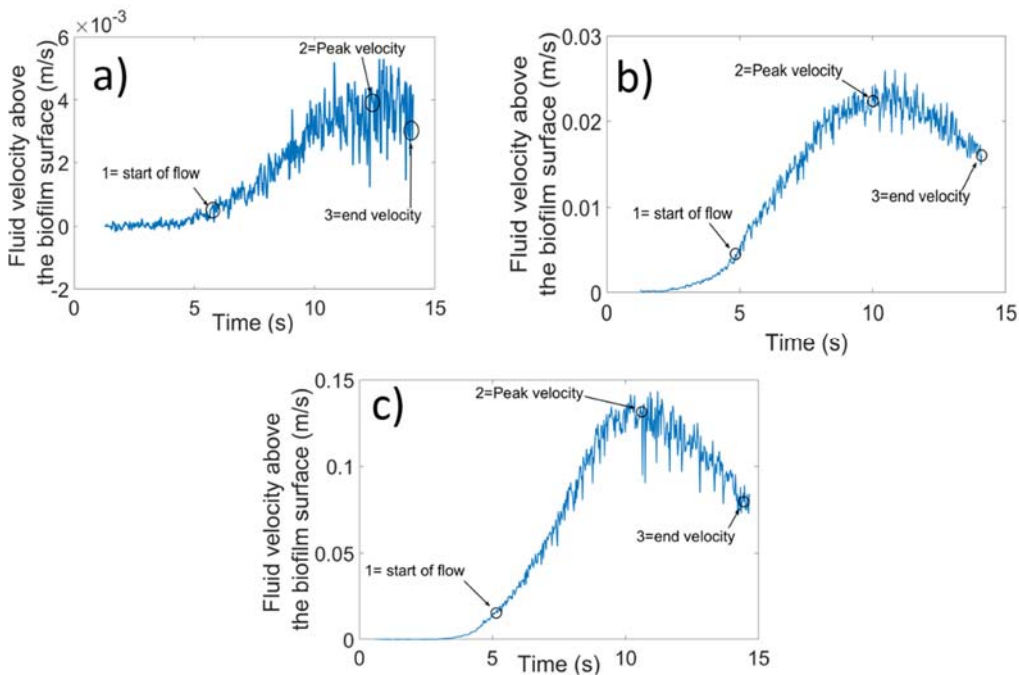


Figure 5:15 Plots showing the velocity profile for different flow rates. The increase and decrease in velocities as provided by the syringe pump can be observed a) Velocity profile recorded for 1000 $\mu\text{l/h}$ showing the different times for the plots shown in Figure 5:16. b) Velocity profile calculated for a flow rate of 5000 $\mu\text{l/h}$ and different times corresponding to Figure 5:17. c) Velocity profile for 25000 $\mu\text{l/h}$ showing the times points in Figure 5:18

The following figures show the magnitude of velocity and the calculated pressure for three different time points as shown in Figure 5:15. The first image pair (first column) shows the velocity and pressure before the flow is ramped. The second image shows the velocity and pressure at the highest flow rate and the third subplot shows the velocity magnitude and velocity at the end of the recording, during the ramp down period.

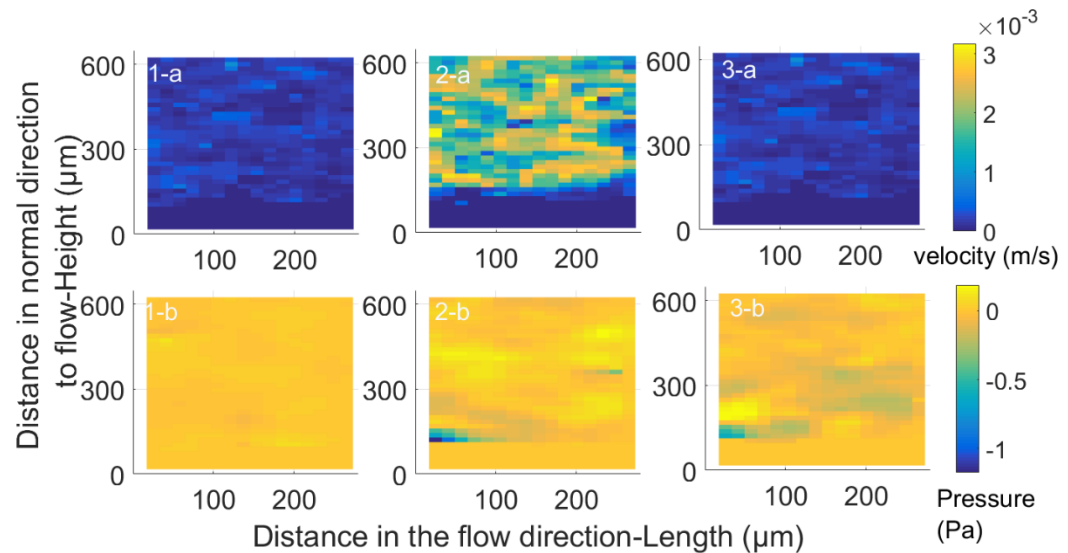


Figure 5:16 Contour plots showing the velocity magnitude (a) and the pressure (b) for a flow rate of 1000 $\mu\text{l/h}$ at different time points as shown in Figure 5:15 (a). The numbers 1, 2, 3 shows the velocity and pressure at times 4 s, 6 s and 10.48 s.

From the above Figure 5:16, it can be observed that the final velocity at time t_3 is not completely zero. But the velocity differences between the three-time points can be seen. The pressure across the channel due to the fluid at the rate of 1000 $\mu\text{l/h}$ is small and it can be seen from the above figure. But the variations in the pressure due to the flow can be observed in Figure 5:17 for a maximum flow rate of 5000 $\mu\text{l/h}$. The maximum velocity magnitude in the channel was 0.023 m/s and a maximum pressure of 0.2 Pa was observed. It can also be clearly observed in this figure, the biofilm surface has no velocity or pressure values. The calculations are carried out only in the liquid portion of the images.

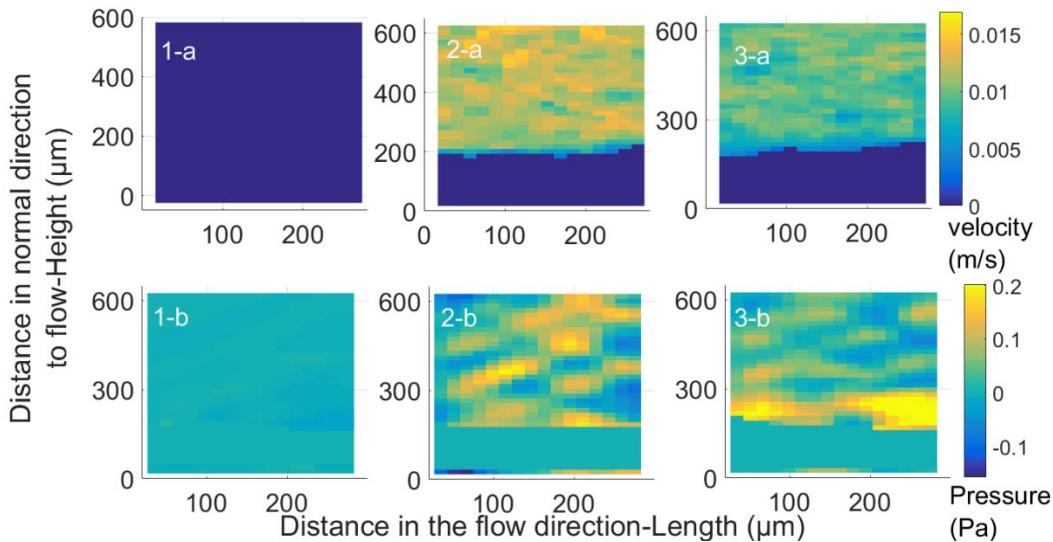


Figure 5:17 Contour plots showing the velocity magnitude (a) and the pressure (b) for the flow rate of 5000 $\mu\text{l/h}$ at different time points as shown in Figure 5:15 (b). The numbers 1, 2, 3 shows the velocity and pressure at times 5 s, 10 s, and 14 s. The dark regions at the bottom of each plot is the biofilm.

Figure 5:18 shows the pressure and velocity calculations for the flow rate of 25000 $\mu\text{l/h}$. The maximum velocity attained in this experiment was 0.14 m/s and maximum pressure attained was 5 Pa.

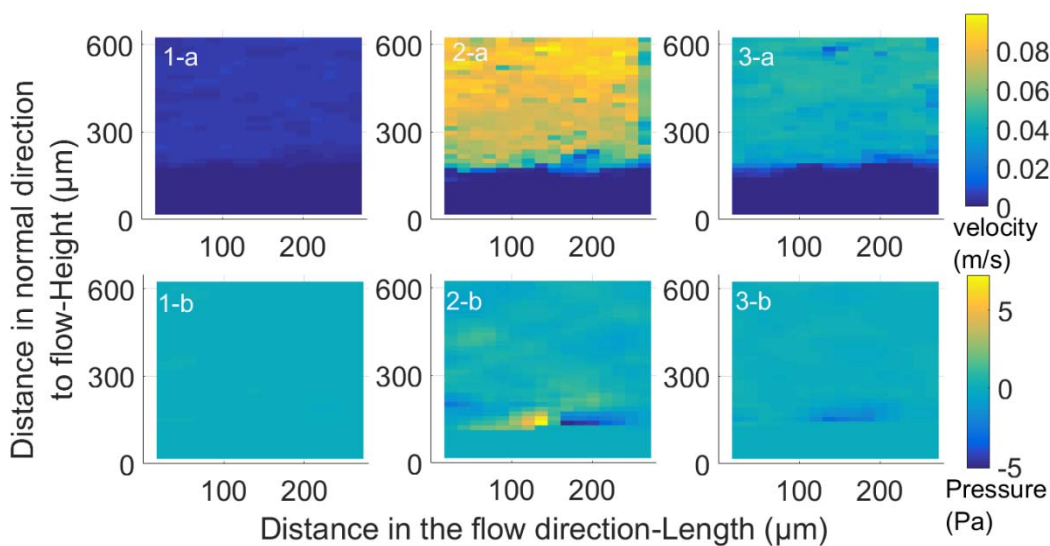


Figure 5:18 Images showing the velocity magnitude (a) and the pressure (b) at three different time points for the maximum flow rate of 25000 $\mu\text{l/h}$. The numbers 1, 2, 3 shows the velocity and pressure at times 5 s, 10 s, and 14 s. The dark regions at the bottom of each plot is the biofilm.

As seen from the above plots, the maximum velocities attained near the surface of the biofilm is proportional to the flow rates. For the maximum

flow rate of 25,000 $\mu\text{l/h}$, a peak velocity of 0.14 m/s was attained. In all the three cases the velocity is ramped up and then down to observe the effect of stress loading and unloading for the biofilm. It can be observed from the figures, there are fluctuations in the calculated velocity. This is inherent in the PIV analysis. From the flow velocity and pressure values obtained using the queen 2 MATLAB code, stress components due to the fluid flow have been calculated. The stress acting on the biofilm due to the fluid can be divided into normal and tangential stress.

By using the velocity values and the pressure values the stresses are computed using the following equation.

$$\overline{\sigma_{ij}} = -p\delta_{ij} + 2\mu\epsilon_{ij} \quad (5.19)$$

$$\epsilon_{ij} = \left(\frac{\partial \overline{u_i}}{\partial x_j} + \frac{\partial \overline{v_j}}{\partial x_i} \right) \quad \delta_{ij} = 1 \text{ if } i = j$$

$$\delta_{ij} = 0 \text{ if } i \neq j$$

The strain experienced by the biofilm due to the stresses acting on the biofilm surface is calculated by the following formula

$$\epsilon = \frac{\Delta L}{L} \quad (5.20)$$

where, length L is the thickness of the biofilm in the normal direction to the flow velocity. ΔL , is the change in length of the biofilm.

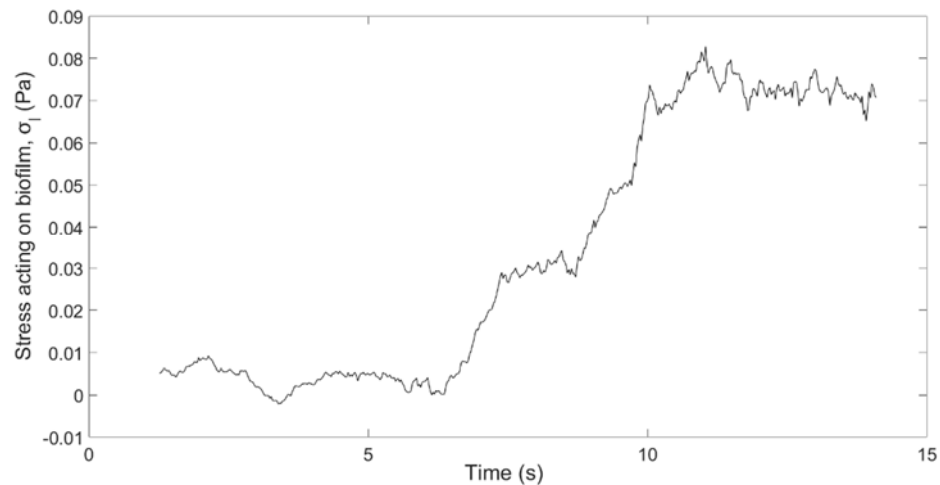


Figure 5:19 Stress vs time for the flow rate of 1000 $\mu\text{l/h}$. The total stress in the fluid flow near the biofilm surface.

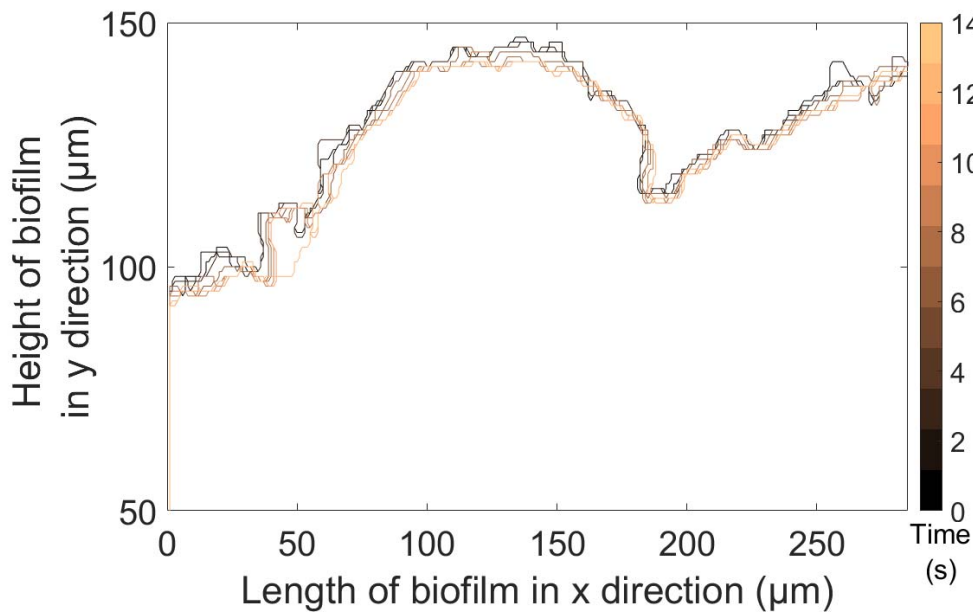


Figure 5:20 The interface of biofilm showing the deformation over time for maximum total stress of 0.08 Pa. The biofilm thickness is altered by the fluid stresses acting on the biofilm surface.

The biofilm deformation for a small flow rate of 1000 $\mu\text{l/h}$ and the stresses due to the flow is shown in the above figures. Maximum total stress of 0.08 Pa was reached in the experiment. The corresponding deformation of the biofilm shows the biofilm has not recovered to the original shape after undergoing the deformation.

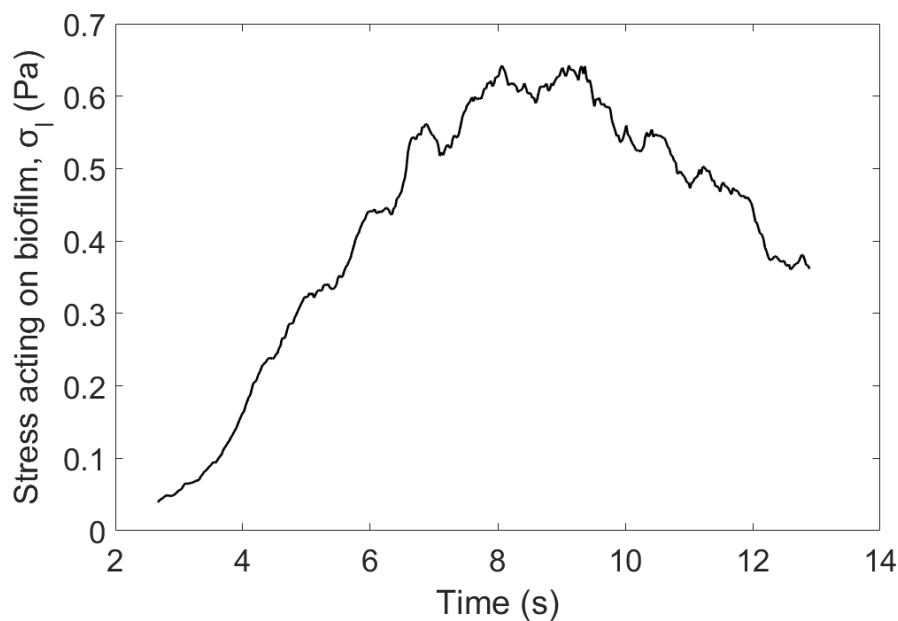


Figure 5:21 Stress vs time for the flow rate of 5000 $\mu\text{l/h}$. The total stress in the fluid flow near the biofilm surface.

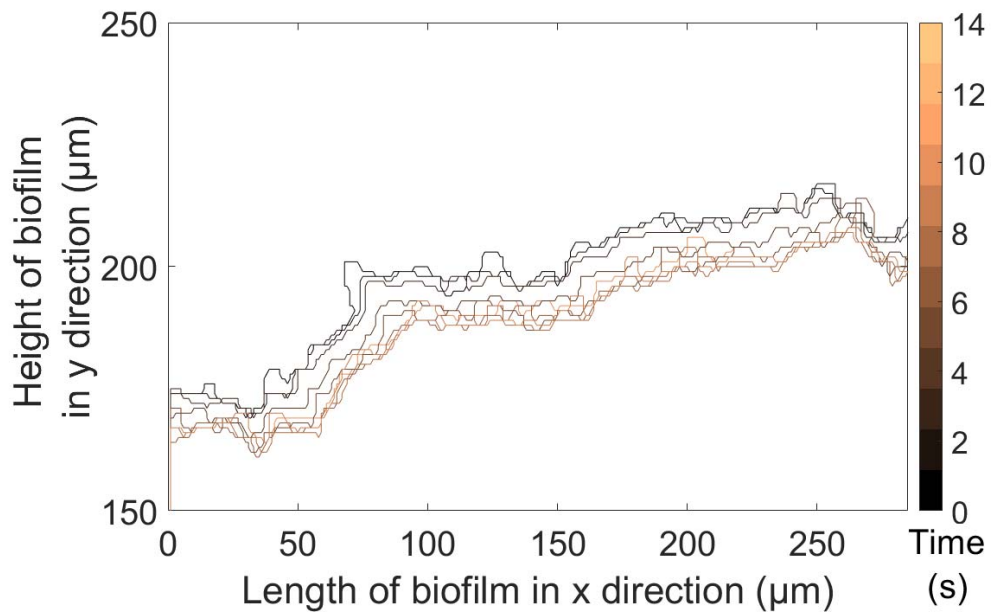


Figure 5:22 The interface of biofilm showing the deformation over time for maximum total stress of 0.8 Pa. The increased deformation compared to the lower flow rate has been observed.

The above figures show increased deformation of the biofilm due to the increase in flow rate. The total stress acting on the biofilm has been increased by an order and the deformation observed is also higher compared to the lower flow rate.

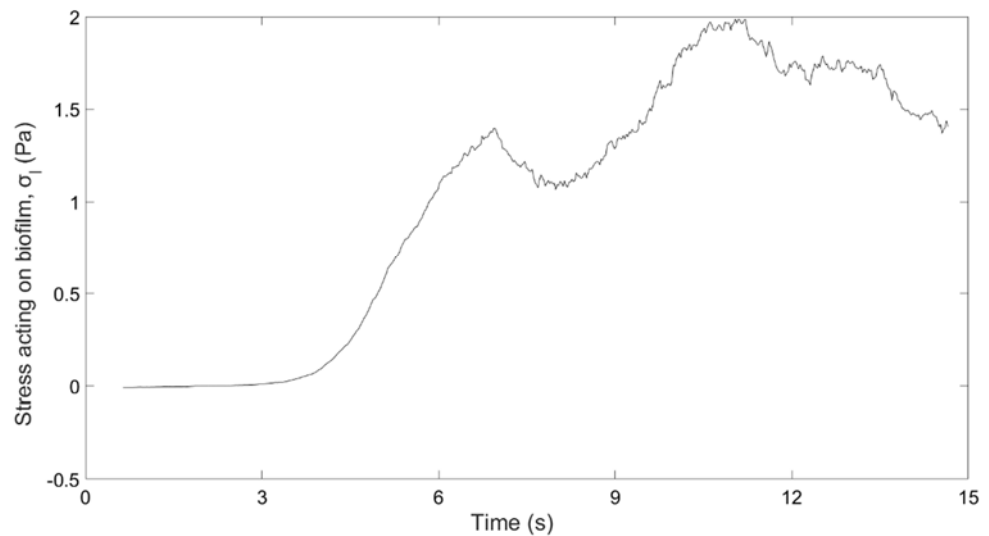


Figure 5:23 Stress versus time for a flow rate of 25000 $\mu\text{l/h}$. The increased stress due to the increase in flow velocity can be observed.

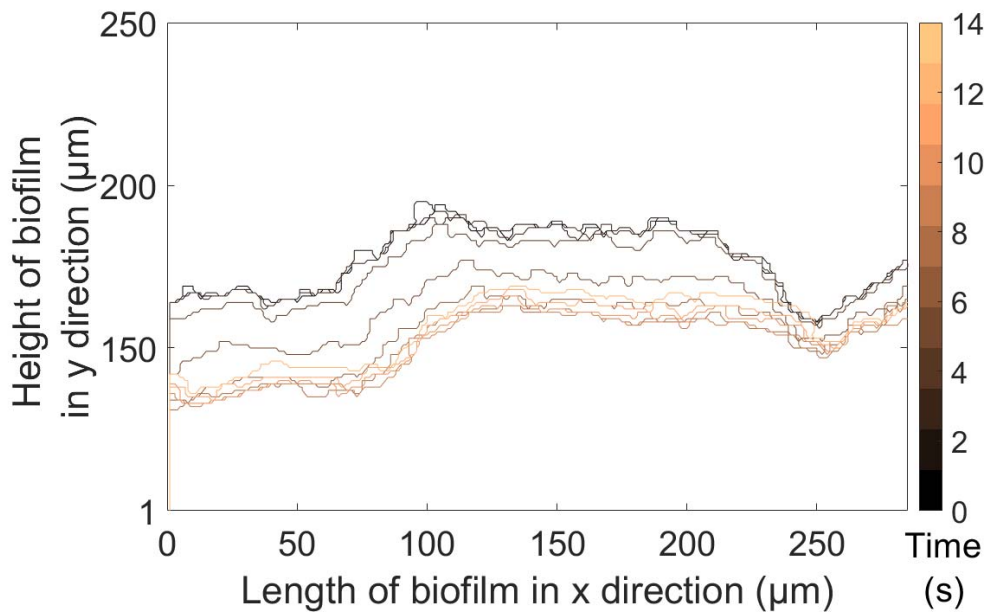


Figure 5:24 Biofilm deformation under maximum stress. The energy lost by the biofilm can be observed from the difference in the initial and final shape of the biofilm.

From the above figure, the maximum deformation by the biofilm due to the stress is calculated to be 30 μm . It is also observed that the biofilm has undergone deformation due to the high fluid stress acting on the biofilm. The time scale for recovery from the deformation much larger compared to the deformation time. To calculate this loss of energy and observe the viscoelastic behavior of the biofilm, the strain versus stress plots are derived as shown in Figure 5:25, Figure 5:26, and Figure 5:27.

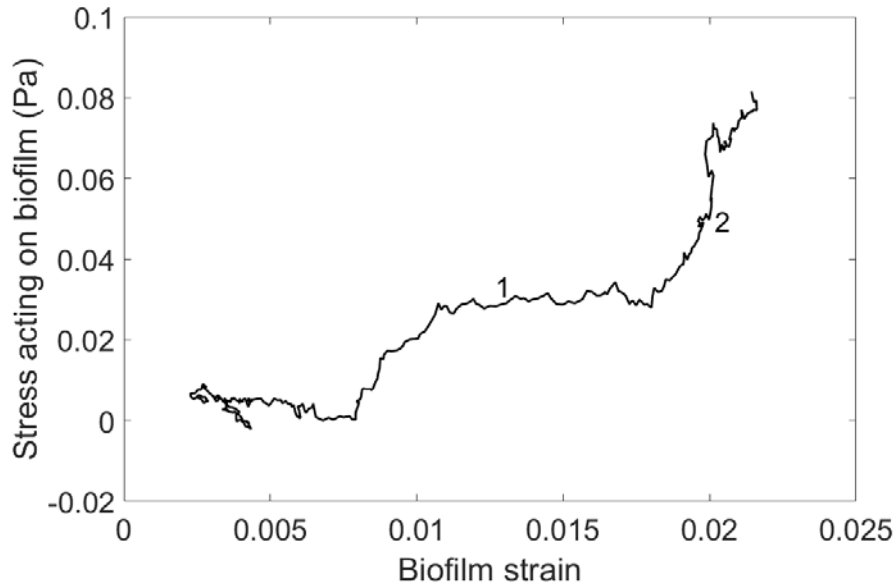


Figure 5:25 Stress in the liquid versus strain experienced by biofilm for a flow rate of 1000 $\mu\text{l/h}$. The Young's modulus is calculated in Table 5-1 from the points 1 and 2 shown in the figure.

Calculation locations	1	2
Stress in the liquid σ_1 (Pa)	0.0226 ± 0.002	0.0437 ± 0.0007
Strain	0.01	0.01
Young's modulus (Pa)	2.20 ± 0.15	2.23 ± 0.07

Table 5-1 Table showing stress, strain and Young's modulus for the biofilm at a maximum flow of 1000 $\mu\text{l/h}$ at different time points mentioned in Figure 5:25.

From the above Table 5-1 and Figure 5:25 it can be observed, the data from the lowest flow rate has a considerable amount of error in the calculations. One of the factors observed during experiments is the roughness of the biofilm surface at low flow rates are high and this adds to the errors in the calculation of stress and strain. The stress-strain curve for higher flow rates has fewer errors compared to the low flow rates (Figure 5:27). This effect on the decrease in surface roughness with increasing flow rates is observed by (Picioreanu *et al.*, 2018).

The stress in the liquid acting on the biofilm and the strain appear to be linear from the above plot. The stress versus strain for the flow rate of 5000 $\mu\text{l/h}$ is shown in Figure 5:26.

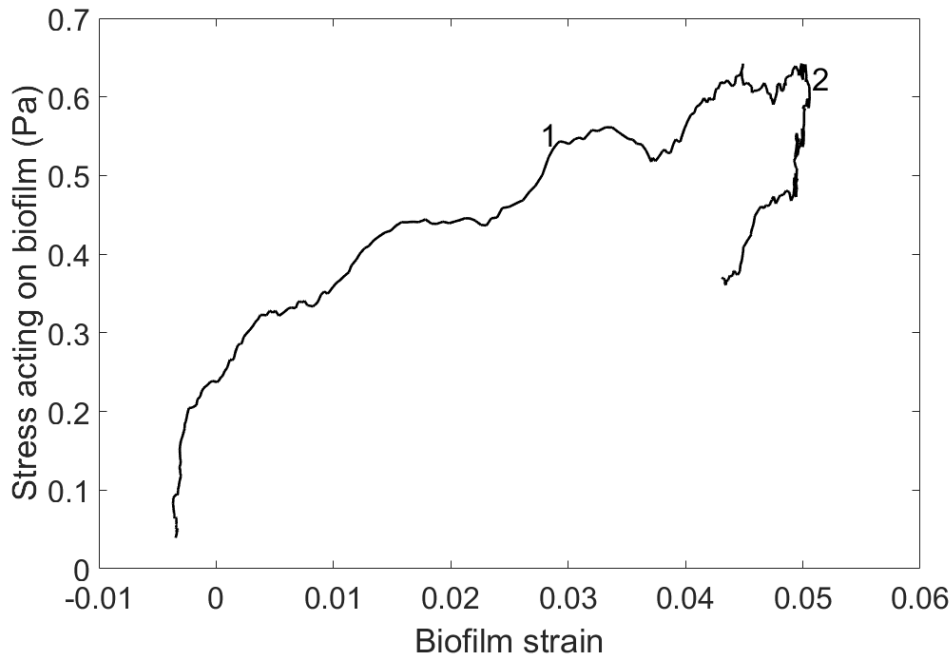


Figure 5:26 Stress in the liquid versus strain experienced by biofilm for a flow rate of 5000 $\mu\text{l/h}$. The viscoelastic behavior of the biofilm can be observed. The stress-strain values and Young's modulus of the biofilm at the points 1 and 2 shown in the figure are given in Table 5-2.

Calculation locations	1	2
Stress in the liquid σ_1 (Pa)	0.53 ± 0.09	0.64 ± 0.003
Strain	0.029	0.049
Young's modulus (Pa)	18.36 ± 0.31	12.92 ± 0.04

Table 5-2 Table showing stress, strain and Young's modulus for the biofilm at a maximum flow of 5000 $\mu\text{l/h}$ at different time points mentioned in Figure 5:26

From the above Figure 5:26 shows the stress-strain curve for the biofilm under the fluid stress from a flow rate of 5000 $\mu\text{l/h}$. The viscoelastic behavior of the biofilm can be observed from the plot, from the hysteresis loop. The complete unloading cycle is not observed due to recording restrictions. A part of the unloading part is shown in the figure. The biofilm

can be observed to have lost energy by the stress loading on the biofilm. This can be observed from Table 3-4. The stress-strain curve for the flow velocity of 25000 $\mu\text{l/h}$ is shown below. Under the highest flow rate of 25000 $\mu\text{l/h}$, the biofilm appears to yield as observed from Figure 5:27.

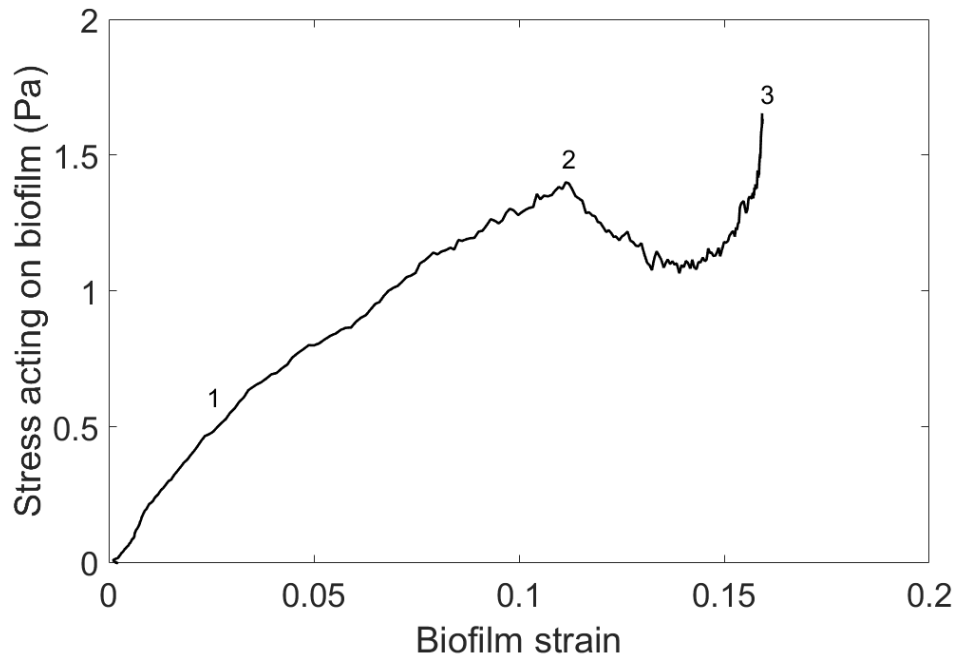


Figure 5:27 Stress-strain curve for the maximum flow rate of 25000 $\mu\text{l/h}$. The figure shows the stress-strain from the start of velocity to the peak velocity. The yielding of the biofilm can be observed in the figure. The Young's modulus is calculated in Table 5-3 from the points 1, 2 and 3 shown in the figure.

Table 5-3 shows Young's modulus calculated at different time points from the above stress-strain curves. The points of calculation are shown in Figure 5:27 above.

Calculation locations	1	2	3
Stress in the liquid σ_1 (Pa)	0.51 ± 0.01	1.39 ± 0.002	1.64 ± 0.01
Strain	0.027	0.11	0.11
Young's modulus (Pa)	18.71 ± 0.19	12.56 ± 0.14	10.29 ± 0.08

Table 5-3 Table showing the stress, strain and Young's modulus values at different time points as shown in Figure 5:27. The biofilm strength decreases due to the loading until strain hardening occurs.

For a flow rate of 25000 $\mu\text{l/h}$, yielding of the biofilm was observed as seen in the stress-strain curve in the above Figure 5:27. At stress value of 1.4 Pa, the biofilm appears to be yielding, the yield strength at this point is 12.56 Pa. After this point, the biofilm yields and the biofilm starts strain hardening. This property can be attributed to the porous regions of the biofilm being squeezed and after this restructuring, the biofilm might start to harden. The regions of biofilm where this deformation happens are shown in Figure 5:28 below. This phenomenon of the fluid being squeezed out from the voids and channels in the biofilm structure have been observed by (Stoodley *et al.*, 2000). The biofilm continues to harden after this until the unloading starts. The modulus corresponding to the maximum stress and strain under a high flow of 25000 $\mu\text{l/h}$ is observed to be 10.29 Pa.

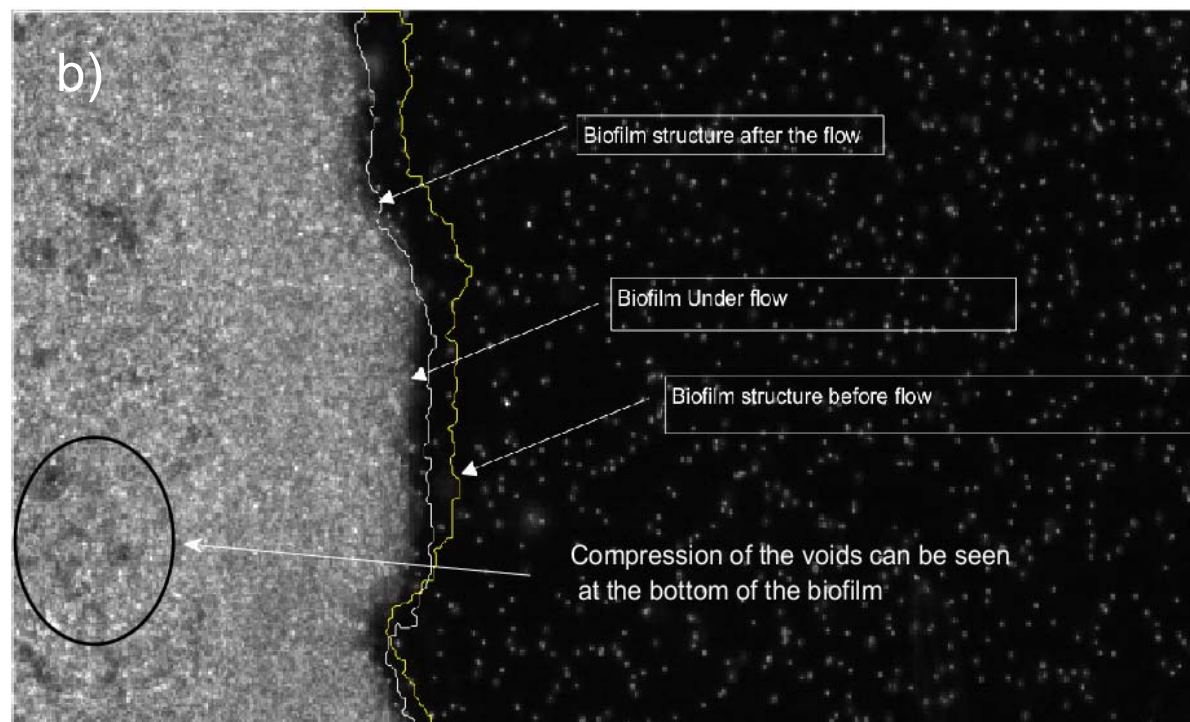
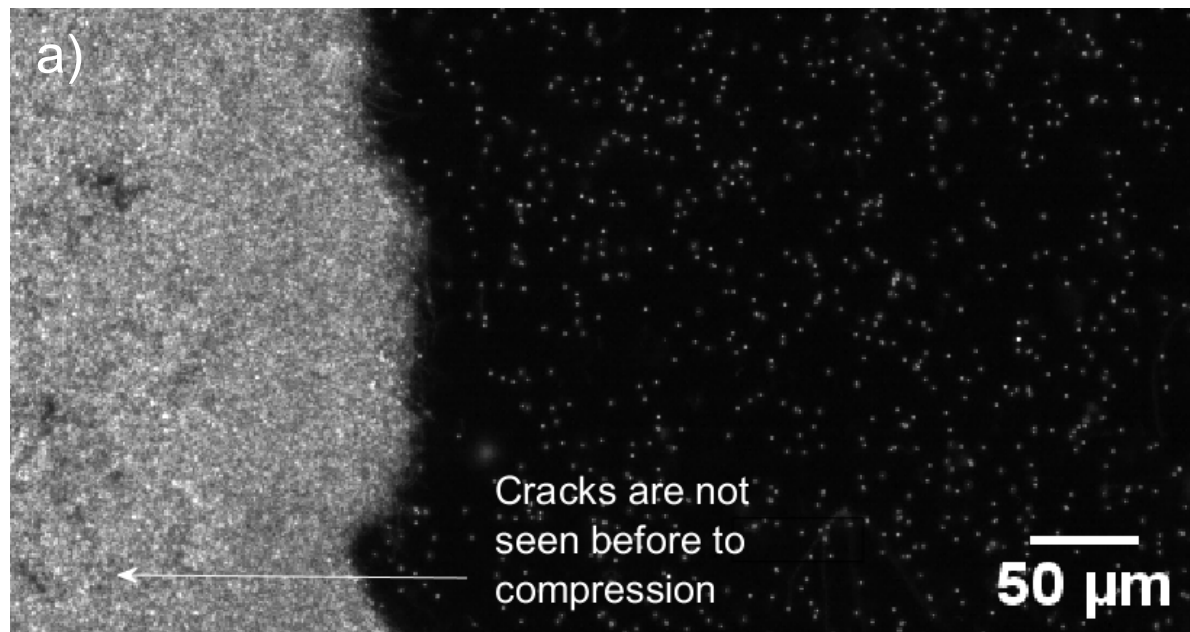


Figure 5:28 Deformation of biofilm under a flow velocity of 0.14 m/s (25000 $\mu\text{l/h}$) near the biofilm surface. The lines show the biofilm boundary before deformation and biofilm boundary after the loading and unloading cycle.

The above image shows the deformation of the biofilm after applying the flow of 25000 $\mu\text{l/h}$. The biofilm can be observed to have undergone permanent deformation. Similar deformation was observed by (Stoodley *et al.*, 2000). Deformation of *P. aeruginosa* biofilms under stress have shown a reduction of 25% in the thickness of biofilm upon stress of 0-10.11 Pa. In the current study, the biofilm has lost 9% of its thickness upon applying a

stress of 0-2 Pa. It has been demonstrated, the reduction in thickness is due to porosity and the reduction in thickness compacts the bacterial cells, thereby reducing the porosity of biofilm (Stoodley *et al.*, 2000). In a study by (Stoodley *et al.*, 1994) it has been shown, the nutrient transport can happen through the channels present in the biofilms. The real-time response of biofilms for the fluid stresses have been captured by the use of high-speed imaging techniques.

5.5 Conclusions

Micro PIV has been employed to observe the viscoelastic deformation of the biofilms. From the experiments, the stresses acting on the biofilm surface were quantified and the deformation of the biofilms was observed. This method of testing biofilms in situ provides the true mechanical characteristics of the biofilm since the structure of the EPS is not altered before the experiments. The viscoelastic properties of the biofilm can be observed by the hysteresis loop in Figure 5:26. This suggests the viscoelastic nature of biofilms measured in this work. Therefore, the viscoelastic properties of biofilms using microfluidics will be determined in the future. The detachment of bacterial clumps detaching from the biofilm was observed but was not pursued in the current study. The exposed rough features of the biofilm at the biofilm liquid interface was detached earlier under minimal stresses.

6 Conclusions and future work

6.1 Conclusions

The two main stages of biofilm films were studied in this current work. Multiple experiments and computational modelling have been used to study the effect of fluid flow in the attachment of planktonic bacteria (*S. gordonii*) to the steel surfaces and biofilm deformation (*B. subtilis*).

Bacterial attachment on steel surfaces was characterized using different surface roughness, topographies by employing different flow velocities. A computational model using mechanical factors influencing the bacterial attachment was developed and validated with the experiments.

Further to study the effect of flow in the deformation of the biofilms in situ, Micro PIV technique was employed and the changes in the stress and strain of the biofilm underflow analyzed.

Based on the findings of the research, the following conclusions can be drawn,

- The surface roughness of the surface material plays a vital role in the attachment of bacterial cells. The surface coverage of the attached bacteria increased with the increase in roughness under static conditions.
- The effect of conditioning layer (saliva coating) in masking the roughness properties showed no significant difference.
- In static conditions, the bacterial attachment under different topographies had no effect on the attachment, the increase in attachment under the topographies is due to the surface roughness and surface hydrophobicity. This is mainly due to the fact the dimensions of the topographies are larger by an order of 2 to that of the bacterial cells.
- The topographical features of the surfaces only come into play under flow conditions. The transport of bacterial cells from fluid medium to the surface is greatly altered by the presence of topographies.
- The surface coverage of the attached bacteria inside the 40 μm depth channels is reduced with the increase in the flow velocity.

- The surface coverage inside the 10 μm depth channels, on the other hand, is not greatly reduced compared to plain surfaces. The main reason for this change is due to the difference in the aspect ratios of the channels (10 and 40 μm depth and 120 μm width).
- A computational model has been developed to validate the bacterial attachment using physical properties like surface roughness (surface element integration), surface chemistry (XDLVO theory), topographies and fluid flow.
- The computational model was qualitatively comparable to the experimental results obtained in the study. The effect of physical forces in the bacterial attachment is explained using the model.
- The changes in bacterial attachment due to the combined effect of fluid flow and topographies was observed by the computational model.
- The effect of flow on a mature biofilm is also studied by the use of microfluidics. An experimental model for the in situ observation of the viscoelastic properties and deformation of the biofilm has been developed.
- The developed method was used to successfully calculate the stress and strain of the biofilm due to the fluid flow.

Overall, the study demonstrated the physical properties influencing the attachment of bacteria on steel surfaces and an experimental model has been developed and tested to examine the viscoelastic properties of the biofilm.

6.2 Future work

This study has contributed to understanding the effect of fluid flow on the attachment of bacteria and deformation of biofilms. Some of the suggestions for future work that can contribute and test the current findings are

Improvement of the computational models for bacterial attachment:

In the current study, the computational model is employed using the physical properties of the surface and bacterial cells. The model can

further be developed to take into consideration the biological adhesion – ligand interactions and the role of surface appendages.

Testing the experimental model for biofilm deformation:

The currently developed method to observe biofilm deformation has been carried out using *B. subtilis*. It will be beneficial to study different biofilms in situ to further understand the viscoelasticity of the biofilms.

Biofilm detachment using microfluidics:

The biofilm detachment and dispersal is an important phenomenon and the similar method used for biofilm deformation can be employed to study the detachment of biofilms.

Appendix

The computational code developed to study the bacterial attachment is available on GitHub under the following link

<https://github.com/subashbommu/Biofilm-deposition-model.git>

The computational model is for surface element integration and calculation of XDLVO interactions are modelled using C++. The Navier-Stokes equation is solved using MATLAB.

The mass of bacteria deposited is calculated from the deposition rate obtained from the diffusion-convection equation. The steps used for calculating the deposited mass is given below.

- The average deposition rate for different surfaces is calculated. Plain surface, inside and outside the channelled surface and the walls of the channel.
- From the experiments, the surface area of each sample is calculated. From the dimensions, the average mass deposited over the surface area is calculated from the deposition rate.
- From this the average mass of bacteria, the number of bacterial cells and the equivalent surface coverage by it are calculated and plotted.

The MATLAB codes used to process the biofilm experiments can be obtained from the GitHub link below

https://github.com/subashbommu/Stress_strain_from-velocity-and-pressure.git

The Queen 2 MATLAB code (Dabiri *et al.*, 2014) used in this work can be obtained from the link below.

<http://dabirilab.com/software/>

References

- Abban, S., Jakobsen, M. and Jespersen, L. (2012) 'Attachment behaviour of *Escherichia coli* K12 and *Salmonella typhimurium* P6 on food contact surfaces for food transportation', *Food Microbiology*, 31(2), pp. 139-147.
- Abbott, A. and Hayes, M.L. (1984) 'The conditioning role of saliva in streptococcal attachment to hydroxyapatite surfaces', *Journal of General Microbiology*, 130(4), pp. 809-816.
- Absolom, D.R., Lamberti, F.V., Policova, Z., Zingg, W., van Oss, C.J. and Neumann, A.W. (1983) 'Surface thermodynamics of bacterial adhesion', *Applied and Environmental Microbiology*, 46(1), pp. 90-97.
- Al Ashhab, A., Sweity, A., Bayramoglu, B., Herzberg, M. and Gillor, O. (2017) 'Biofouling of reverse osmosis membranes: effects of cleaning on biofilm microbial communities, membrane performance, and adherence of extracellular polymeric substances', *Biofouling*, 33(5), pp. 397-409.
- Alfa, M.J. and Howie, R. (2009) 'Modeling microbial survival in buildup biofilm for complex medical devices', *BMC Infectious Diseases*, 9(1), p. 56.
- Alpkvist, E., Picioareanu, C., van Loosdrecht, M.C. and Heyden, A. (2006) 'Three-dimensional biofilm model with individual cells and continuum EPS matrix', *Biotechnology and Bioengineering*, 94(5), pp. 961-979.
- Ammar, Y., Swailes, D., Bridgens, B. and Chen, J. (2015) 'Influence of surface roughness on the initial formation of biofilm', *Surface and Coatings Technology*, 284(1), pp. 410-416.
- Ayad, M.F., Rosenstiel, S.F. and Salama, M. (1997) 'Influence of tooth surface roughness and type of cement on retention of complete cast crowns', *The Journal of Prosthetic Dentistry*, 77(2), pp. 116-121.
- Aydin, M. and Fenner, R.T. (2001) 'Boundary element analysis of driven cavity flow for low and moderate Reynolds numbers', *International Journal for Numerical Methods in Fluids*, 37(1), pp. 45-64.
- Aykent, F., Yondem, I., Ozyesil, A.G., Gunal, S.K., Avunduk, M.C. and Ozkan, S. (2010) 'Effect of different finishing techniques for restorative materials on surface roughness and bacterial adhesion', *The Journal of Prosthetic Dentistry*, 103(4), pp. 221-227.
- Back, C.R., Sztukowska, M.N., Till, M., Lamont, R.J., Jenkinson, H.F., Nobbs, A.H. and Race, P.R. (2017) 'The *Streptococcus gordonii* adhesin CshA protein binds host fibronectin via a catch-clamp mechanism', *Journal of Biological Chemistry*, 292(5), pp. 1538-1549.
- Bahar, O., De La Fuente, L. and Burdman, S. (2010) 'Assessing adhesion, biofilm formation and motility of *Acidovorax citrulli* using microfluidic flow chambers', *FEMS Microbiology Letters*, 312(1), pp. 33-39.
- Baier, R.E. (1975) 'Applied chemistry at protein interfaces', in *Applied Chemistry at Protein Interfaces*. American Chemical Society, pp. 1-25.

- Baier, R.E. (1982) 'Conditioning surfaces to suit the biomedical environment: recent progress', *Journal of Biomechanical Engineering*, 104(4), pp. 257-271.
- Bakterij, A. (2014) 'An overview of the influence of stainless-steel surface properties on bacterial adhesion', *Materiali in tehnologije*, 48(5), pp. 609-617.
- Balazs, D.J., Triandafillu, K., Chevolut, Y., Aronsson, B.O., Harms, H., Descouts, P. and Mathieu, H.J. (2003) 'Surface modification of PVC endotracheal tubes by oxygen glow discharge to reduce bacterial adhesion', *Surface and Interface Analysis*, 35(3), pp. 301-309.
- Baumann, B., Duker, J.S., Potsaid, B. and Fujimoto, J.G. (2011) 'Ultrahigh speed optical coherence tomography: New developments for ophthalmic imaging', *International Review of Ophthalmic Optics*.
- Berke, A.P., Turner, L., Berg, H.C. and Lauga, E. (2008) 'Hydrodynamic attraction of swimming microorganisms by surfaces', *Physical Review Letters*, 101(3), p. 38102.
- Berne, C., Ducret, A., Hardy, G.G. and Brun, Y.V. (2015) 'Adhesins involved in attachment to abiotic surfaces by Gram-negative bacteria', *Microbiology Spectrum*, 3(4), pp. 163-199.
- Berne, C., Ellison, C.K., Ducret, A. and Brun, Y.V. (2018) 'Bacterial adhesion at the single-cell level', *Nature Reviews Microbiology*, 16(10), pp. 616-627.
- Bhadra, C.M., Truong, V.K., Pham, V.T.H., Al Kobaisi, M., Seniutinas, G., Wang, J.Y., Juodkazis, S., Crawford, R.J. and Ivanova, E.P. (2015) 'Antibacterial titanium nano-patterned arrays inspired by dragonfly wings', *Scientific Reports*, 5, pp. 16817-16817.
- Billings, N., Birjiniuk, A., Samad, T.S., Doyle, P.S. and Ribbeck, K. (2015) 'Material properties of biofilms-a review of methods for understanding permeability and mechanics', *Reports on Progress in Physics*, 78(3), p. 36601.
- Blauert, F., Horn, H. and Wagner, M. (2015) 'Time-resolved biofilm deformation measurements using optical coherence tomography', *Biotechnology and Bioengineering*, 112(9), pp. 1893-1905.
- Boks, N.P., Norde, W., van der Mei, H.C. and Busscher, H.J. (2008) 'Forces involved in bacterial adhesion to hydrophilic and hydrophobic surfaces', *Microbiology*, 154(Pt 10), pp. 3122-3133.
- Bowen, B.D., Levine, S. and Epstein, N. (1976) 'Fine particle deposition in laminar flow through parallel-plate and cylindrical channels', *Journal of Colloid and Interface Science*, 54(3), pp. 375-390.

- Boyd, R.D., Verran, J., Jones, M.V. and Bhakoo, M. (2002) 'Use of the Atomic Force Microscope To determine the effect of substratum surface topography on bacterial adhesion', *Langmuir*, 18(6), pp. 2343-2346.
- Bray, D. (2001) 'Cell movements: From molecules to motility', New York: Garland Science.
- Bruus, H. (2008) *Theoretical microfluidics*. Oxford: Oxford University Press.
- Bryers, J.D. (2008) 'Medical biofilms', *Biotechnology and Bioengineering*, 100(1), pp. 1-18.
- Busscher, H.J. and van der Mei, H.C. (2006) 'Microbial adhesion in flow displacement systems', *Clinical Microbiology Reviews*, 19(1), pp. 127-141.
- Cairns, L.S., Marlow, V.L., Bissett, E., Ostrowski, A. and Stanley-Wall, N.R. (2013) 'A mechanical signal transmitted by the flagellum controls signalling in *Bacillus subtilis*', *Molecular Microbiology*, 90(1), pp. 6-21.
- Cao, Y., Su, B., Chinnaraj, S., Jana, S., Bowen, L., Charlton, S., Duan, P., Jakubovics, N.S. and Chen, J. (2018) 'Nanostructured titanium surfaces exhibit recalcitrance towards *Staphylococcus epidermidis* biofilm formation', *Scientific Reports*, 8(1), p. 1071.
- Capdeville, B. and Rols, J.L. (1992) 'Introduction to biofilms in water and wastewater treatment', in Melo, L.F., Bott, T.R., Fletcher, M. and Capdeville, B. (eds.) *Biofilms - Science and Technology*. Dordrecht: Springer Netherlands, pp. 13-20.
- Characklis, W.G. and Marshall, K. (1990) *Biofilms*. New York: Wiley.
- Chaturongkasumrit, Y., Takahashi, H., Keeratipibul, S., Kuda, T. and Kimura, B. (2011) 'The effect of polyesterurethane belt surface roughness on *Listeria monocytogenes* biofilm formation and its cleaning efficiency', *Food Control*, 22(12), pp. 1893-1899.
- Cheng, Y.T., Rodak, D.E., Wong, C.A. and Hayden, C.A. (2006) 'Effects of micro- and nano-structures on the self-cleaning behaviour of lotus leaves', *Nanotechnology*, 17(5), pp. 1359-1362.
- Christopher, M.W. and Bonnie, L.B. (2005) 'QUORUM SENSING: Cell-to-cell communication in bacteria', *Annual Review of Cell and Developmental Biology*, 21(1), pp. 319-346.
- Costerton, J.W., Lewandowski, Z., Caldwell, D.E., Korber, D.R. and Lappin-Scott, H.M. (1995) 'Microbial biofilms', *Annual Reviews in Microbiology*, 49(1), pp. 711-745.
- Crawford, R.J., Webb, H.K., Truong, V.K., Hasan, J. and Ivanova, E.P. (2012) 'Surface topographical factors influencing bacterial attachment', *Advances in Colloid and Interface Science*, 179-182, pp. 142-149.

- Cvitkovitch, D.G., Li, Y.-H. and Ellen, R.P. (2003) 'Quorum sensing and biofilm formation in *Streptococcal* infections', *Journal of Clinical Investigation*, 112(11), pp. 1626-1632.
- Dabiri, D. (2006) 'Cross-correlation digital particle image velocimetry—a review', *Turbul. ABCM Curitiba*, 155, p. 199.
- Dabiri, J.O., Bose, S., Gemmell, B.J., Colin, S.P. and Costello, J.H. (2014) 'An algorithm to estimate unsteady and quasi-steady pressure fields from velocity field measurements', *Journal of Experimental Biology*, pp. jeb-092767.
- Dantas, L.C.d.M., Silva-Neto, J., xe, o Paulo, d., Dantas, T.S., Naves, L.Z., das Neves, F., xe, vio, D., da Mota, A., xe and rito, S. (2016) 'Bacterial adhesion and surface roughness for different clinical techniques for acrylic polymethyl methacrylate', *International Journal of Dentistry*, 2016, p. 6.
- Ding, A.M., Palmer, R.J., Jr., Cisar, J.O. and Kolenbrander, P.E. (2010) 'Shear-enhanced oral microbial adhesion', *Applied and Environmental Microbiology*, 76(4), pp. 1294-1297.
- Dodd, M.S., Papineau, D., Grenne, T., Slack, J.F., Rittner, M., Pirajno, F., O'Neil, J. and Little, C.T.S. (2017) 'Evidence for early life in Earth's oldest hydrothermal vent precipitates', *Nature*, 543, p. 60.
- Donlan, R.M. (2002) 'Biofilms: microbial life on surfaces', *Emerging Infectious Diseases*, 8(9), pp. 881-890.
- Donlan, R.M. and Costerton, J.W. (2002) 'Biofilms: survival mechanisms of clinically relevant microorganisms', *Clinical Microbiology Reviews*, 15(2), pp. 167-193.
- Drescher, K., Dunkel, J., Cisneros, L.H., Ganguly, S. and Goldstein, R.E. (2011) 'Fluid dynamics and noise in bacterial cell-cell and cell-surface scattering', *Proceedings of the National Academy of Sciences of the United States of America*, 108(27), pp. 10940-10945.
- Drescher, K., Shen, Y., Bassler, B.L. and Stone, H.A. (2013) 'Biofilm streamers cause catastrophic disruption of flow with consequences for environmental and medical systems', *Proceedings of the National Academy of Sciences of the United States of America*, 110(11), pp. 4345-4350.
- El Moustaid, F., Eladdadi, A. and Uys, L. (2013) 'Modeling bacterial attachment to surfaces as an early stage of biofilm development', *Mathematical Biosciences & Engineering*, 10(3), pp. 821-842.
- Ensikat, H.J., Ditsche-Kuru, P., Neinhuis, C. and Barthlott, W. (2011) 'Superhydrophobicity in perfection: the outstanding properties of the lotus leaf', *Beilstein Journal of Nanotechnology*, 2, p. 152.

- Epstein, A.K., Hochbaum, A.I., Kim, P. and Aizenberg, J. (2011) 'Control of bacterial biofilm growth on surfaces by nanostructural mechanics and geometry', *Nanotechnology*, 22(49), p. 4484.
- Etxeberria, M., López Jiménez, L., Merlos, A., Henar, E. and Viñas, M. (2013) 'Bacterial adhesion efficiency on implant abutments: a comparative study', *International Microbiology*, 16(4), pp. 235-242.
- Flemming, H.-C., Neu, T.R. and Wozniak, D.J. (2007) 'The EPS matrix: the "house of biofilm cells"', *Journal of Bacteriology*, 189(22), pp. 7945-7947.
- Flemming, H.C. (2011) 'Microbial biofouling: unsolved problems, insufficient approaches, and possible solutions', in *Biofilm Highlights*. Springer, pp. 81-109.
- Flemming, H.C. and Wingender, J. (2010) 'The biofilm matrix', *Nature Reviews Microbiology*, 8(9), pp. 623-633.
- Francois, P., Vaudaux, P., Nurdin, N., Mathieu, H.J., Descouts, P. and Lew, D.P. (1996) 'Physical and biological effects of a surface coating procedure on polyurethane catheters', *Biomaterials*, 17(7), pp. 667-678.
- Friedlander, R.S., Vlamakis, H., Kim, P., Khan, M., Kolter, R. and Aizenberg, J. (2013) 'Bacterial flagella explore microscale hummocks and hollows to increase adhesion', *Proceedings of the National Academy of Sciences of the United States of America*, 110(14), pp. 5624-5629.
- Garnett, A.J. and Matthews, S. (2012) 'Interactions in bacterial biofilm development: a structural perspective', *Current Protein and Peptide Science*, 13(8), pp. 739-755.
- Garrett, T.R., Bhakoo, M. and Zhang, Z. (2008) 'Bacterial adhesion and biofilms on surfaces', *Progress in Natural Science*, 18(9), pp. 1049-1056.
- George, O.T., Heidi, B.K. and Roberto, K. (2000) 'Biofilm formation as microbial development', *Annual Review of Microbiology*, 54(1), pp. 49-79.
- Graham, M. and Cady, N. (2014) 'Nano and microscale topographies for the prevention of bacterial surface fouling', *Coatings*, 4(1), pp. 37-59.
- Guan, Y.H., Lath, D.L., Graaf, T., Lilley, T.H. and Brook, AH, B. (2003) 'Moderation of oral bacterial adhesion on saliva-coated hydroxyapatite by polyaspartate', *Journal of Applied Microbiology*, 94(3), pp. 456-461.
- Halan, B., Buehler, K. and Schmid, A. (2012) 'Biofilms as living catalysts in continuous chemical syntheses', *Trends in Biotechnology*, 30(9), pp. 453-465.
- Harrison, S.M. and Cleary, P.W. (2014) 'Towards modelling of fluid flow and food breakage by the teeth in the oral cavity using smoothed particle hydrodynamics (SPH)', *European Food Research and Technology*, 238(2), pp. 185-215.

- Hasan, J., Webb, H.K., Truong, V.K., Pogodin, S., Baulin, V.A., Watson, G.S., Watson, J.A., Crawford, R.J. and Ivanova, E.P. (2013) 'Selective bactericidal activity of nanopatterned superhydrophobic cicada *Psaltoda claripennis* wing surfaces', *Applied Microbiology and Biotechnology*, 97(20), pp. 9257-9262.
- Hauert, R. (2003) 'A review of modified DLC coatings for biological applications', *Diamond and Related Materials*, 12(3-7), pp. 583-589.
- Head, D., A. Devine, D. and Marsh, P.D. (2017) 'In silico modelling to differentiate the contribution of sugar frequency versus total amount in driving biofilm dysbiosis in dental caries', *Scientific Reports*, 7(1), p. 17413.
- Hizal, F., Rungraeng, N., Lee, J., Jun, S., Busscher, H.J., van der Mei, H.C. and Choi, C.H. (2017) 'Nanoengineered superhydrophobic surfaces of aluminum with extremely low bacterial adhesivity', *ACS Applied Materials and Interfaces*, 9(13), pp. 12118-12129.
- Hochbaum, A.I. and Aizenberg, J. (2010) 'Bacteria pattern spontaneously on periodic nanostructure arrays', *Nano Letters*, 10(9), pp. 3717-3721.
- Hoek, E.M. and Agarwal, G.K. (2006) 'Extended DLVO interactions between spherical particles and rough surfaces', *Journal of Colloid and Interface Science*, 298(1), pp. 50-58.
- Hoek, E.M.V., Bhattacharjee, S. and Elimelech, M. (2003) 'Effect of membrane surface roughness on colloid-membrane DLVO interactions', *Langmuir*, 19(11), pp. 4836-4847.
- Horvath, R., Dregelyi-Kiss, Á. and Matyasi, G. (2015) 'The examination of surface roughness parameters in the fine turning of hypereutectic aluminium alloys', *Scientific Bulletin-University Politehnica of Bucharest Series D*, 77(2), pp. 205-216.
- Hotze, E.M., Phenrat, T. and Lowry, G.V. (2010) 'Nanoparticle aggregation: challenges to understanding transport and reactivity in the environment', *Journal of Environmental Quality*, 39(6), pp. 1909-1924.
- Hou, S., Gu, H., Smith, C. and Ren, D. (2011) 'Microtopographic patterns affect *Escherichia coli* biofilm formation on poly(dimethylsiloxane) surfaces', *Langmuir*, 27(6), pp. 2686-2691.
- Ista, L.K. and López, G.P. (2013) 'Thermodynamic analysis of marine bacterial attachment to oligo(ethylene glycol)-terminated self-assembled monolayers', *Biointerphases*, 8(1), p. 24.
- James, N.R. and Jayakrishnan, A. (2003) 'Surface thiocyanation of plasticized poly (vinyl chloride) and its effect on bacterial adhesion', *Biomaterials*, 24(13), pp. 2205-2212.
- James, S.A., Hilal, N. and Wright, C.J. (2017) 'Atomic force microscopy studies of bioprocess engineering surfaces—imaging, interactions and

mechanical properties mediating bacterial adhesion', *Biotechnology Journal*, 12(7), p. 1860.

Janjaroen, D., Ling, F.Q., Monroy, G., Derlon, N., Morgenroth, E., Boppart, S.A., Liu, W.T. and Nguyen, T.H. (2013) 'Roles of ionic strength and biofilm roughness on adhesion kinetics of *Escherichia coli* onto groundwater biofilm grown on PVC surfaces', *Water Research*, 47(7), pp. 2531-2542.

Jayathilake, P.G., Gupta, P., Li, B., Madsen, C., Oyebamiji, O., González-Cabaleiro, R., Rushton, S., Bridgens, B., Swailes, D. and Allen, B. (2017) 'A mechanistic individual-based model of microbial communities', *PloS one*, 12(8), p. e0181965

Jin, F., Conrad, J.C., Gibiansky, M.L. and Wong, G.C.L. (2011) 'Bacteria use type-IV pili to slingshot on surfaces', *Proceedings of the National Academy of Sciences of the United States of America*, 108(31), pp. 12617-12622.

Kandemir, N., Vollmer, W., Jakubovics, N.S. and Chen, J. (2018) 'Mechanical interactions between bacteria and hydrogels', *Scientific Reports*, 8(1), p. 10893.

Kargar, M., Wang, J., Nain, A.S. and Behkam, B. (2012) 'Controlling bacterial adhesion to surfaces using topographical cues: a study of the interaction of *Pseudomonas aeruginosa* with nanofiber-textured surfaces', *Soft Matter*, 8(40), p. 10254.

Katsikogianni, M.G. and Missirlis, Y.F. (2010) 'Interactions of bacteria with specific biomaterial surface chemistries under flow conditions', *Acta Biomater*, 6(3), pp. 1107-1118.

Kavitha, S. and Raghavan, V. (2018) 'Isolation and characterization of marine biofilm forming bacteria from a ship's hull', *Frontiers in Biology*, 13(3), pp. 208-214.

Kaya, T. and Koser, H. (2012) 'Direct upstream motility in *Escherichia coli*', *Biophysical Journal*, 102(7), pp. 1514-1523.

Kearns, D.B. (2010) 'A field guide to bacterial swarming motility', *Nature reviews. Microbiology*, 8(9), pp. 634-644.

Kelly, P. (2013) 'Solid mechanics part I: An introduction to solid mechanics', *Solid mechanics lecture notes*, pp. 283-337.

Kesel, A. and Liedert, R. (2007) 'Learning from nature: non-toxic biofouling control by shark skin effect', *Comparative Biochemistry and Physiology*, 4(146), p. 130.

Kim, J., Park, H.D. and Chung, S. (2012) 'Microfluidic approaches to bacterial biofilm formation', *Molecules*, 17(8), pp. 9818-9834.

- Kim, M.K., Drescher, K., Pak, O.S., Bassler, B.L. and Stone, H.A. (2014) 'Filaments in curved streamlines: Rapid formation of *Staphylococcus aureus* biofilm streamers', *New Journal of Physics*, 16(6).
- Kinnari, T.J., Esteban, J., Martin-de-Hijas, N.Z., Sanchez-Munoz, O., Sanchez-Salcedo, S., Colilla, M., Vallet-Regi, M. and Gomez-Barrena, E. (2009) 'Influence of surface porosity and pH on bacterial adherence to hydroxyapatite and biphasic calcium phosphate bioceramics', *Journal of Medical Microbiology*, 58(1), pp. 132-137.
- Klemm, P. and Schembri, M.A. (2000) 'Bacterial adhesins: function and structure', *International Journal of Medical Microbiology*, 290(1), pp. 27-35.
- Kolenbrander, P.E., Andersen, R.N., Blehert, D.S., Eglund, P.G., Foster, J.S. and Palmer, R.J. (2002) 'Communication among Oral Bacteria', *Microbiology and Molecular Biology Reviews*, 66(3), pp. 486-505.
- Kundukad, B., Seviour, T., Liang, Y., Rice, S.A., Kjelleberg, S. and Doyle, P.S. (2016) 'Mechanical properties of the superficial biofilm layer determine the architecture of biofilms', *Soft matter*, 12(26), pp. 5718-5726.
- Larsen, T. and Fiehn, N.-E. (2017) 'Dental biofilm infections – an update', *APMIS*, 125(4), pp. 376-384.
- Laufer, B.Z., Pilo, R. and Cardash, H.S. (1996) 'Surface roughness of tooth shoulder preparations created by rotary instrumentation, hand planing, and ultrasonic oscillation', *The Journal of Prosthetic Dentistry*, 75(1), pp. 4-8.
- Lauga, E. (2016) 'Bacterial hydrodynamics', *Annual Review of Fluid Mechanics*, 48(1), pp. 105-130.
- Lauga, E., DiLuzio, W.R., Whitesides, G.M. and Stone, H.A. (2006) 'Swimming in circles: motion of bacteria near solid boundaries', *Biophysical Journal*, 90(2), pp. 400-412.
- Lecuyer, S., Rusconi, R., Shen, Y., Forsyth, A., Vlamakis, H., Kolter, R. and Stone, H.A. (2011) 'Shear stress increases the residence time of adhesion of *Pseudomonas aeruginosa*', *Biophysical Journal*, 100(2), pp. 341-350.
- Lele, P.P., Hosu, B.G. and Berg, H.C. (2013) 'Dynamics of mechanosensing in the bacterial flagellar motor', *Proceedings of the National Academy of Sciences of the United States of America*, 110(29), pp. 11839-11844.
- Li, G., Tam, L.K. and Tang, J.X. (2008) 'Amplified effect of Brownian motion in bacterial near-surface swimming', *Proceedings of the National Academy of Sciences of the United States of America* 105(47), pp. 18355-18359.
- Lieleg, O., Caldara, M., Baumgärtel, R. and Ribbeck, K. (2011) 'Mechanical robustness of *Pseudomonas aeruginosa* biofilms', *Soft matter*, 7(7), pp. 3307-3314.

- Liu, Y. and Tay, J.H. (2002) 'The essential role of hydrodynamic shear force in the formation of biofilm and granular sludge', *Water Research*, 36(7), pp. 1653-1665.
- Lorite, G.S., Rodrigues, C.M., de Souza, A.A., Kranz, C., Mizaikoff, B. and Cotta, M.A. (2011) 'The role of conditioning film formation and surface chemical changes on *Xylella fastidiosa* adhesion and biofilm evolution', *Journal of Colloid and Interface Science*, 359(1), pp. 289-295.
- Ma, J., Sun, Y., Gleichauf, K., Lou, J. and Li, Q. (2011) 'Nanostructure on taro leaves resists fouling by colloids and bacteria under submerged conditions', *Langmuir*, 27(16), pp. 10035-10040.
- Mahapatra, A., Padhi, N., Mahapatra, D., Bhatt, M., Sahoo, D., Jena, S., Dash, D. and Chayani, N. (2015) 'Study of biofilm in bacteria from water pipelines', *Journal of Clinical and Diagnostic Research*, 9(3), pp. DC09-DC11.
- Mahmoud, B., Zhe, X., Leah, G., Yingjie, D., Hongbing, L., Philippe, Z. and Majid, M.-J. (2014) 'Nanoindentation of *Pseudomonas aeruginosa* bacterial biofilm using atomic force microscopy', *Materials Research Express*, 1(4), p. 045411.
- Mainardi, F. and Spada, G. (2011) 'Creep, relaxation and viscosity properties for basic fractional models in rheology', *The European Physical Journal Special Topics*, 193(1), pp. 133-160.
- Mainwaring, D.E., Nguyen, S.H., Webb, H., Jakubov, T., Tobin, M., Lamb, R.N., Wu, A.H., Marchant, R., Crawford, R.J. and Ivanova, E.P. (2016) 'The nature of inherent bactericidal activity: insights from the nanotopology of three species of dragonfly', *Nanoscale*, 8(12), pp. 6527-6534.
- McClaine, J.W. and Ford, R.M. (2002) 'Characterizing the adhesion of motile and nonmotile *Escherichia coli* to a glass surface using a parallel-plate flow chamber', *Biotechnology and Bioengineering*, 78(2), pp. 179-189.
- Mei, L., Busscher, H.J., van der Mei, H.C. and Ren, Y. (2011) 'Influence of surface roughness on *Streptococcal* adhesion forces to composite resins', *Dental Materials*, 27(8), pp. 770-8.
- Merz, A.J. and Forest, K.T. (2002) 'Bacterial surface motility: slime trails, grappling hooks and nozzles', *Current Biology*, 12(8), pp. R297-R303.
- Missirlis, Y.F. and Katsikogianni, M. (2007) 'Theoretical and experimental approaches of bacteria-biomaterial interactions', *Materialwissenschaft und Werkstofftechnik*, 38(12), pp. 983-994.
- Mitik-Dineva, N., Wang, J., Mocanaru, R.C., Stoddart, P.R., Crawford, R.J. and Ivanova, E.P. (2008) 'Impact of nano-topography on bacterial attachment', *Biotechnology Journal: Healthcare Nutrition Technology*, 3(4), pp. 536-544.

- Molaei, M. and Sheng, J. (2016) 'Succeed escape: Flow shear promotes tumbling of *Escherichia coli* near a solid surface', *Scientific Reports*, 6, p. 35290.
- Mullan, F., Austin, R.S., Parkinson, C.R., Hasan, A. and Bartlett, D.W. (2017) 'Measurement of surface roughness changes of unpolished and polished enamel following erosion', *PloS one*, 12(8), pp. e0182406-e0182406.
- Nyvad, B. and Kilian, M. (1987) 'Microbiology of the early colonization of human enamel and root surfaces in vivo', *Scandinavian Journal of Dental Research* 95(5), pp. 369-80.
- O'Loughlin, C.T., Miller, L.C., Siryaporn, A., Drescher, K., Semmelhack, M.F. and Bassler, B.L. (2013) 'A quorum-sensing inhibitor blocks *Pseudomonas aeruginosa* virulence and biofilm formation', *Proceedings of the National Academy of Sciences of the United States of America*, 110(44), pp. 17981-6.
- Ottemann, K.M. and Miller, J.F. (1997) 'Roles for motility in bacterial-host interactions', *Molecular Microbiology*, 24(6), pp. 1109-17.
- Pachori, A., Kambalimath, H., Maran, S., Niranjana, B., Bhambhani, G. and Malhotra, G. (2018) 'Evaluation of changes in salivary pH after intake of different eatables and beverages in children at different time intervals', *International Journal of Clinical Pediatric Dentistry*, 11(3), pp. 177-182.
- Palermo, A. and Marzani, A. (2015) 'Limits of the Kelvin Voigt Model for the analysis of wave propagation in monoatomic mass-spring chains', *Journal of Vibration and Acoustics*, 138(1), pp. 011022-011022-9.
- Palmer, J., Flint, S. and Brooks, J. (2007) 'Bacterial cell attachment, the beginning of a biofilm', *Journal of Industrial Microbiology and Biotechnology*, 34(9), pp. 577-588.
- Paramonova, E., de Jong, E.D., Krom, B.P., van der Mei, H.C., Busscher, H.J. and Sharma, P.K. (2007) 'Low-Load compression testing: a novel way of measuring biofilm thickness', *Applied and Environmental Microbiology*, 73(21), pp. 7023-7028.
- Paramonova, E., Kalmykova, O.J., van der Mei, H.C., Busscher, H.J. and Sharma, P.K. (2009) 'Impact of hydrodynamics on oral biofilm strength', *Journal of Dental Research*, 88(10), pp. 922-6.
- Persat, A., Nadell, C.D., Kim, M.K., Ingremeau, F., Siryaporn, A., Drescher, K., Wingreen, N.S., Bassler, B.L., Gitai, Z. and Stone, H.A. (2015) 'The mechanical world of bacteria', *Cell*, 161(5), pp. 988-997.
- Petrova, O.E. and Sauer, K. (2012) 'Sticky situations-Key components that control bacterial surface attachment', *Journal of Bacteriology*, pp. 3-12.
- Picioareanu, C., Blauert, F., Horn, H. and Wagner, M. (2018) 'Determination of mechanical properties of biofilms by modelling the deformation

- measured using optical coherence tomography', *Water Research*, 145, pp. 588-598.
- Poncin-Epaillard, F., Herry, J.M., Marmey, P., Legeay, G., Debarnot, D. and Bellon-Fontaine, M.N. (2013) 'Elaboration of highly hydrophobic polymeric surface--a potential strategy to reduce the adhesion of pathogenic bacteria?', *Materials Science and Engineering: C*, 33(3), pp. 1152-61.
- Pratt, L.A. and Kolter, R. (1998) 'Genetic analysis of *Escherichia coli* biofilm formation: roles of flagella, motility, chemotaxis and type I pili', *Molecular Microbiology*, 30(2), pp. 285-293.
- Raffel, M., Willert, C.E., Scarano, F., Kähler, C.J., Wereley, S.T. and Kompenhans, J. (2018) *Particle image velocimetry: a practical guide*. Springer.
- Renner, L.D. and Weibel, D.B. (2011) 'Physicochemical regulation of biofilm formation', *MRS bulletin*, 36(5), pp. 347-355.
- Riedewald, F. (2006) 'Bacterial adhesion to surfaces: the influence of surface roughness', *PDA Journal of Pharmaceutical Science and Technology*, 60(3), pp. 164-71.
- Rusconi, R., Garren, M. and Stocker, R. (2014) 'Microfluidics expanding the frontiers of microbial ecology', *Annual Review of Biophysics*, 43, pp. 65-91.
- Saini, R., Saini, S. and Sharma, S. (2011) 'Biofilm: A dental microbial infection', *Journal of Natural Science, Biology, and Medicine*, 2(1), pp. 71-75.
- Sharma, S., Jaimes-Lizcano, Y.A., McLay, R.B., Cirino, P.C. and Conrad, J.C. (2016) 'Subnanometric roughness affects the deposition and mobile adhesion of *Escherichia coli* on silanized glass surfaces', *Langmuir*, 32(21), pp. 5422-33.
- Shaw, T., Winston, M., Rupp, C.J., Klapper, I. and Stoodley, P. (2004) 'Commonality of elastic relaxation times in biofilms', *Physical Review Letters*, 93(9), p. 098102.
- Silverman, M. and Simon, M. (1974) 'Flagellar rotation and the mechanism of bacterial motility', *Nature*, 249, p. 73.
- Stewart, P.S. (2002) 'Mechanisms of antibiotic resistance in bacterial biofilms', *International Journal of Medical Microbiology*, 292(2), pp. 107-13.
- Stoodley, P., Cargo, R., Rupp, C.J., Wilson, S. and Klapper, I. (2002) 'Biofilm material properties as related to shear-induced deformation and detachment phenomena', *Journal of Industrial Microbiology and Biotechnology*, 29(6), pp. 361-367.
- Stoodley, P., Debeer, D. and Lewandowski, Z. (1994) 'Liquid flow in biofilm systems', *Applied and Environmental Microbiology*, 60(8), pp. 2711-2716.

- Stoodley, P., Hall-Stoodley, L. and Lappin-Scott, H.M. (2001) 'Detachment, surface migration, and other dynamic behavior in bacterial biofilms revealed by digital time-lapse imaging', in *Methods in Enzymology*. Elsevier, pp. 306-319.
- Stoodley, P., Lewandowski, Z., Boyle, J.D. and Lappin-Scott, H.M. (2000) 'Structural deformation of bacterial biofilms caused by short-term fluctuations in fluid shear: An in situ investigation of biofilm rheology', *Biotechnology and Bioengineering*, 65(1), pp. 83-92.
- Tala, L., Fineberg, A., Kukura, P. and Persat, A. (2018) 'Label-free visualization of type IV pili dynamics by interferometric scattering microscopy', *bioRxiv*, p. 298562.
- Taylor, R.L., Verran, J., Lees, G.C. and Ward, A.P. (1998) 'The influence of substratum topography on bacterial adhesion to polymethyl methacrylate', *Journal of Materials Science: Materials in Medicine*, 9(1), pp. 17-22.
- Tolker-Nielsen, T., Brinch, U.C., Ragas, P.C., Andersen, J.B., Jacobsen, C.S. and Molin, S. (2000) 'Development and dynamics of *Pseudomonas* sp biofilms', *Journal of Bacteriology*, 182(22), pp. 6482-6489.
- Towler, B.W., Rupp, C.J., Cunningham, A.B. and Stoodley, P. (2003) 'Viscoelastic properties of a mixed culture biofilm from rheometer creep analysis', *Biofouling*, 19(5), pp. 279-285.
- Tsang, P.H., Li, G., Brun, Y.V., Freund, L.B. and Tang, J.X. (2006) 'Adhesion of single bacterial cells in the micronewton range', *Proceedings of the National Academy of Sciences of the United States of America*, 103(15), pp. 5764-5768.
- Tuson, H.H. and Weibel, D.B. (2013) 'Bacteria-surface interactions', *Soft Matter*, 9(18), pp. 4368-4380.
- Van Oss, C.J. (1989) 'Energetics of cell-cell and cell-biopolymer interactions', *Cell Biophysics*, 14(1), pp. 1-16.
- VanEpps, J.S. and Younger, J.G. (2016) 'Implantable device-related infection', *Shock (Augusta, Ga.)*, 46(6), pp. 597-608.
- Videla, H.A. and Herrera, L.K. (2005) 'Microbiologically influenced corrosion: looking to the future', *International microbiology*, 8(3), p. 169.
- Vincent, C., Boerlin, P., Daignault, D., Dozois, C.M., Dutil, L., Galanakis, C., Reid-Smith, R.J., Tellier, P.P., Tellis, P.A., Ziebell, K. and Manges, A.R. (2010) 'Food reservoir for *Escherichia coli* causing urinary tract infections', *Emerging Infectious Diseases*, 16(1), pp. 88-95.
- Wade, W.G. (2013) 'The oral microbiome in health and disease', *Pharmacological Research*, 69(1), pp. 137-143.

- Wang, H., Sodagari, M., Ju, L.K. and Zhang Newby, B.m. (2013) 'Effects of shear on initial bacterial attachment in slow flowing systems', *Colloids and Surfaces B: Biointerfaces*, 109, pp. 32-39.
- Wanner, O. and Reichert, P. (1996) 'Mathematical modeling of mixed-culture biofilms', *Biotechnology and Bioengineering*, 49(2), pp. 172-184.
- Watnick, P. and Kolter, R. (2000) 'Biofilm, city of microbes', *Journal of Bacteriology*, 182(10), pp. 2675-2679.
- Wilson, C.J., Clegg, R.E., Leavesley, D.I. and Pearcy, M.J. (2005) 'Mediation of biomaterial-cell interactions by adsorbed proteins: a review', *Tissue Engineering*, 11(1-2), pp. 1-18.
- Woodyard, L.L., Bowersock, T.L., Turek, J.J., McCabe, G.P. and Deford, J. (1996) 'A comparison of the effects of several silver-treated intravenous catheters on the survival of staphylococci in suspension and their adhesion to the catheter surface', *Journal of Controlled Release*, 40(1), pp. 23-30.
- Worschech, C.C., Rodrigues, J.A., Martins, L.R.M. and Ambrosano, G.M.B. (2003) 'In vitro evaluation of human dental enamel surface roughness bleached with 35% carbamide peroxide and submitted to abrasive dentifrice brushing', *Pesquisa Odontológica Brasileira*, 17(4), pp. 342-348.
- Xu, Z., Liu, Q. and Ling, J. (1995) 'An evaluation of the van Oss-Chaudhury-Good equation and Neumann's equation of state approach with mercury substrate', *Langmuir*, 11(3), pp. 1044-1046.
- Young, K.D. (2006) 'The selective value of bacterial shape', *Microbiology and Molecular Biology Reviews*, 70(3), pp. 660-703.
- Yu, P., Wang, C., Zhou, J., Jiang, L., Xue, J. and Li, W. (2016) 'Influence of surface properties on adhesion forces and attachment of *Streptococcus mutans* to zirconia in vitro', *BioMed Research International*, 2016, p. 10.
- Zhang, X., Zhang, Q., Yan, T., Jiang, Z., Zhang, X. and Zuo, Y.Y. (2015) 'Quantitatively predicting bacterial adhesion using surface free energy determined with a spectrophotometric method', *Environmental Science & Technology*, 49(10), pp. 6164-6171.
- Zhao, Y., Ni, Y. and Zeng, W. (2014) 'A consistent approach for characterising asphalt concrete based on generalised Maxwell or Kelvin model', *Road Materials and Pavement Design*, 15(3), pp. 674-690.